

1 **Environmental influences on human innovation and behavioural diversity in southern**
2 **Africa 92-80 000 years ago**

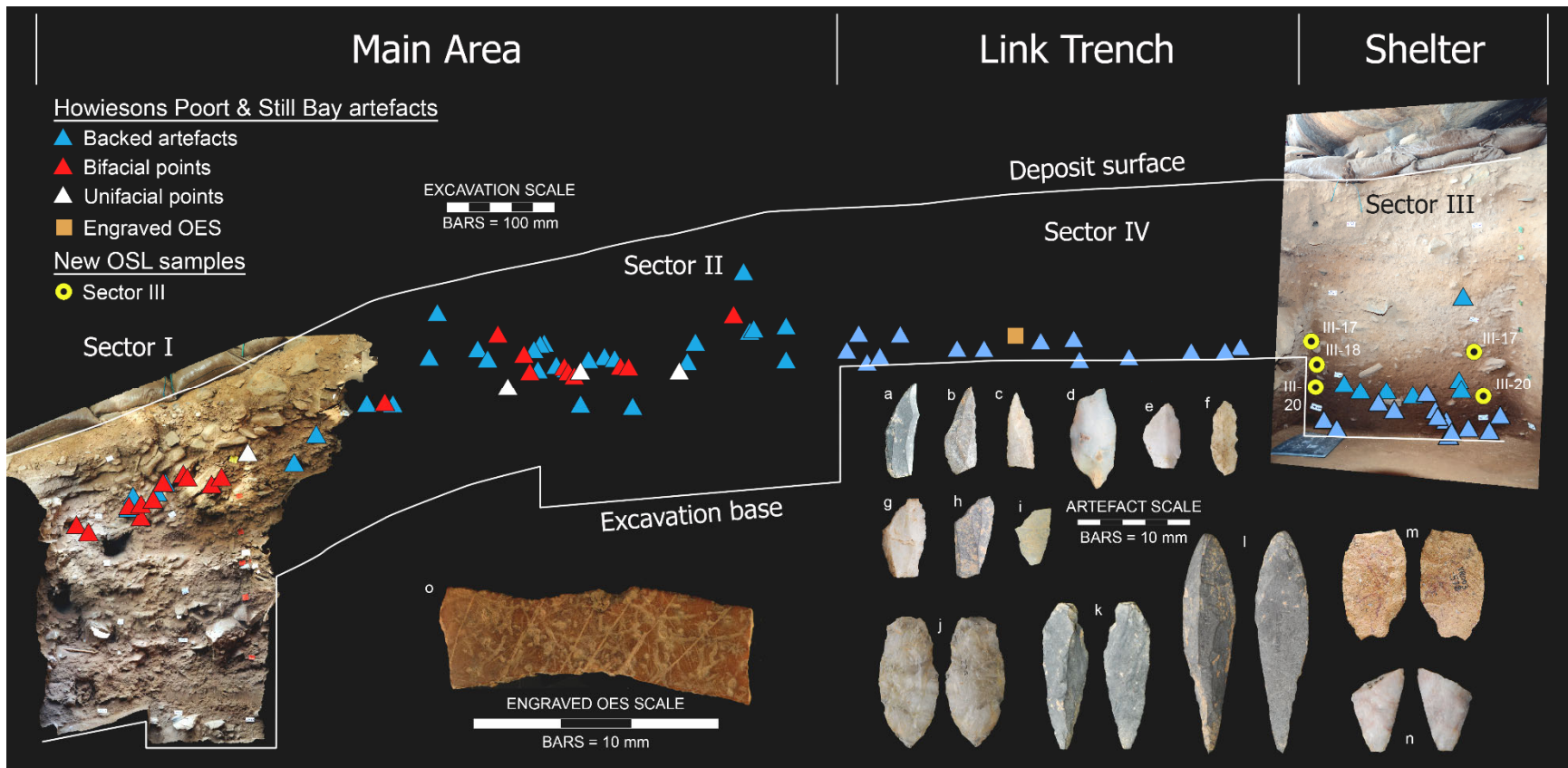
3 Supplementary Information

4 **VR003 excavation history**

5 VR003 has been excavated over five seasons between 2009 and 2016. The initial two seasons
6 had the primary objective of assessing the potential of the deposit, and only selected finds were
7 plotted. The final three seasons 2014-2016 involved plotting of all cultural items using different
8 size cut-offs for different classes of material (≥ 20 mm for lithics, ≥ 25 mm for bone). Some
9 classes of material, notably OES, were only plotted if modified. All plotted artefacts were
10 assigned unique provenience ID's and individually bagged. Sedimentary aggregates were
11 plotted with a single indicative point location, and volume was quantified as proportional bucket
12 volume (FULL, $\frac{3}{4}$, $\frac{1}{2}$, $\frac{1}{4}$). All aggregates were sieved on site through nested 3 mm and 1.5 mm
13 mesh, and the residues from each bagged separately. All plotting was undertaken using a local
14 grid, managed by control points emplaced around the site.

15
16 We currently recognise nine archaeological horizons and eight geological horizons in the Main
17 Area sequence (1); for the sake of simplicity in this paper we refer to the lower two
18 archaeological horizons (I-08 and I-09) in aggregate as the Lower Deposits. All horizons in the
19 Main Area are associated with the MSA. Inside the small extant shelter (known as Sector III) we
20 identify 23 geological horizons (III-01 through III-23), with Late Holocene LSA comprising the
21 upper 14 strata (0.6-0.9 m depth). In the Main Area, I-04 was assigned to the Howiesons Poort
22 and Still Bay (1), though initially dated by OSL in the Main Area to 45.7 ± 2.8 ka. Inside the
23 shelter in Sector III, Howiesons Poort artefacts occur in strata III-18 through III-23, with initial
24 OSL ages of 42.3 ± 2.7 ka and 41.7 ± 2.9 (1) (Still Bay has yet to be encountered in this part of
25 the site). In both areas these ages are unusually young for the Howiesons Poort. We provide a
26 redating here (SI Geochronology below) using OSL on quartz grains from III-18 to III-20 that
27 places the Howiesons Poort between 71.6 ± 6.2 and 60.8 ± 5.2 , consistent with ages elsewhere,
28 with ages for the immediately overlying post-Howiesons Poort stratum III-17 of 55.7 ± 4.4 and
29 66.1 ± 5.3 ka (Figure S1).

30
31 The *fossiles directeur* for the Howiesons Poort and Still Bay (backed artefacts and bifacial points
32 respectively) occur as a discrete band across the entire site and include a single piece of
33 engraved OES in the Link Trench (Figure S1). In the Main Area there is no recurrence of such
34 artefacts in the underlying deposits, which we assign to the pre-Still Bay MSA.



35

36 **Figure S1.** East section view of VR03 deposits showing distribution of Howiesons Poort (backed artefacts, blue triangles) and Still Bay (bifacial
 37 points, red triangles) type markers across the excavation area, and the sampling locations for the five new Sector III quartz OSL ages reported on
 38 here (yellow circles). Unifacial points (white triangles) may occur in either the post-Howiesons Poort or Still Bay; in this case they appear limited to
 39 the Still Bay. a-c, truncated pointed backed pieces; d-f, segments; g-i, truncated oblique pieces; j-n, bifacial and partly-bifacial points and
 40 fragments; o, engraved OES.

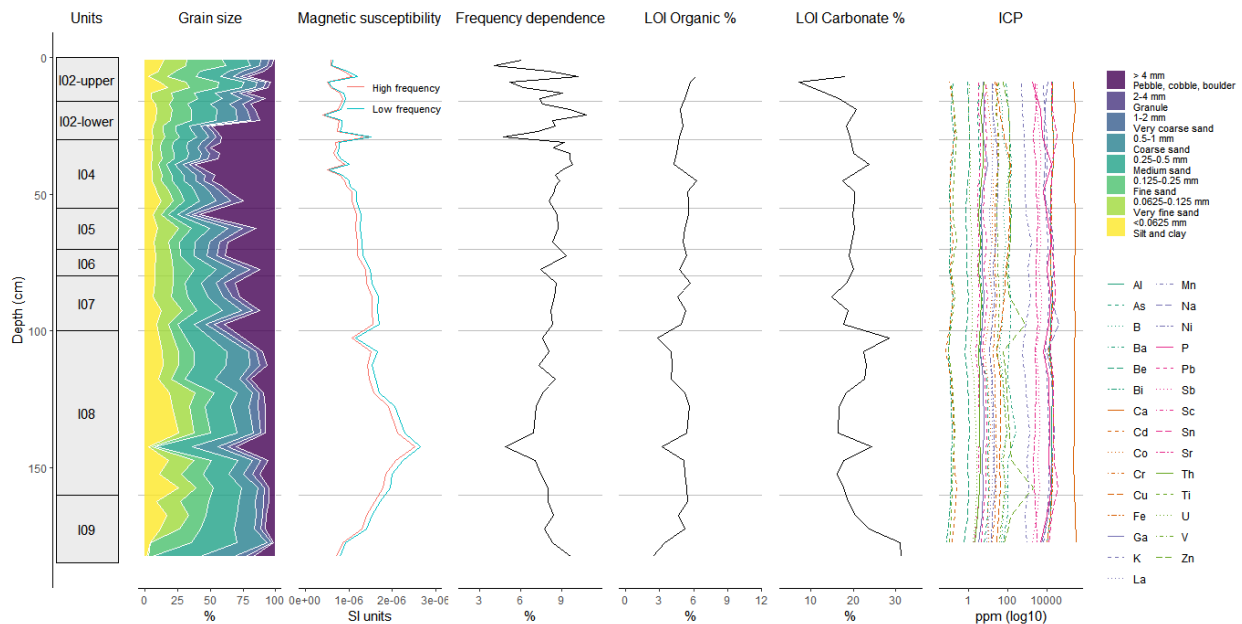
41

42

43 **Geoarchaeology**

44 **Sedimentology.** Grain size analysis, loss on ignition, and magnetic susceptibility shows
45 structured variation through the Main Area deposits (Figure S2). The upper 0.3 m (I-02 & I-03)
46 are significantly finer grained than the rest of the Main Area deposit and show large variations in
47 magnetic susceptibility frequency dependence suggesting that these sediments contain a
48 significant amount of superparamagnetic ferrimagnetic grains interpreted to be formed via
49 anthropogenic burning. Though magnetic susceptibility increases in the lower deposits, the
50 consistency of the frequency dependence indicates a natural signal likely driven by changes in
51 the mineralogy of the deposit. The lower 1.6 m of the Main Area shows a decreasing grain size
52 trend through strata I-04 to I-09, with a significant increase in carbonate percentage in the
53 bottom 100 mm of the section.

54



55

56 **Figure S2.** Grain size, LOI, and magnetic susceptibility data for the Main Area, Sector I.

57

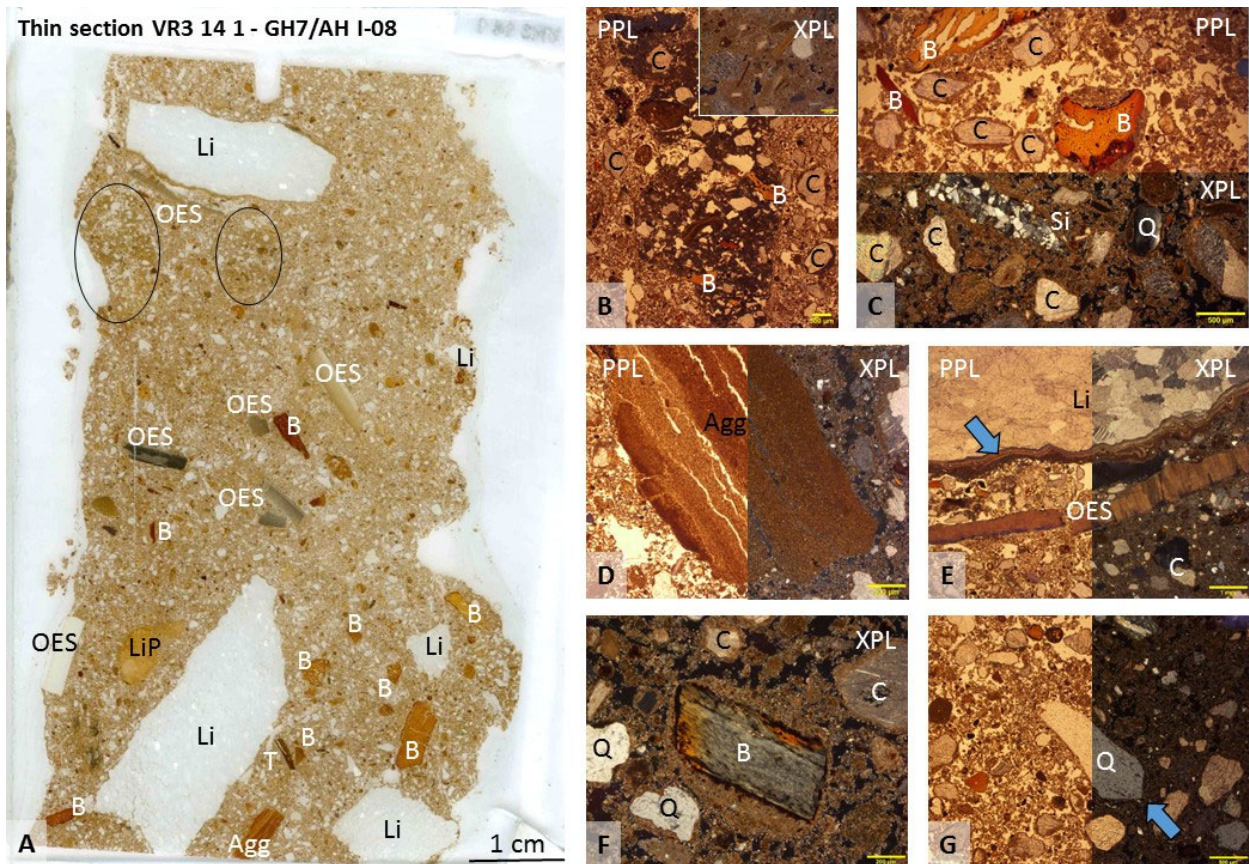
58 **Micromorphology.** Micromorphological analyses were directed at investigating the sedimentary
59 components and formation processes including post-depositional alterations. To this aim we
60 collected three block samples from layers I-08, I-09, and their respective contact. One thin
61 section of each was produced by P. Kritikakis (University of Tübingen, Germany), T. Beckmann
62 (Schwülper-Lagesbüttel, Germany) and T. Culligan (University College Dublin, Ireland). The
63 three thin sections show overall similar characteristic with each other but also with the upper

64 deposits as previously described (1). The related distribution of fine and coarse materials is
65 dominantly porphyric, but sand sized grains generally exhibit a coating with fine material (Figure
66 S3 C). Additionally, cemented areas were observed (Figures S3 A&B, Figure S3 A&C) which
67 show a dense calcitic crystallitic micritic groundmass with floating coarse grains. Otherwise, void
68 space is open and dominated by simple and complex packing voids. Star shaped vughs,
69 channels and chambers are also present. The microstructure is thus massive to spongy, but can
70 also appear as granular due to coated grains. One thin section from I-08 appears to be partially
71 disturbed and shows several deviations from this general microstructure. This includes a clear
72 and wavy contact with the intact part (Figure S4 A & F), silty crusts with vesicles (Figure S4 F),
73 increased density/cementation, a darker shade (compare Figures S4 C, F, & G), and local areas
74 with a massive, well sorted pellet structure (Figure S4 E). However, the disturbed part does not
75 differ in its components from the intact part. In all three analysed thin sections, the material
76 composition can be divided into a fine silty, calcareous matrix with rare silty quartz grains, and
77 coarse grained (> 0.02 mm) geogenic and anthropogenic components. Geogenic components
78 include sand sized calcite crystals (e.g. Figure S3 A-C, & E), fine limestone gravel (e.g. Figure
79 S3 A&E), sand to fine gravel sized quartz (angular or rounded, Figure S3 F&G), rare sand to
80 fine gravel sized, rounded soil aggregates (Figure S3 A, D), fine gravel quartzite and gypsum
81 (Figure S4 D). Gypsum is present as accumulations of lenticular crystals as well as in rounded
82 rocks. The dominant anthropogenic component is bone fragments, which are sand to gravel
83 sized, subrounded to subangular (Figure S3 A-C, Figure S4 A&E, Figure S5 A, 6). Several bone
84 fragments show heating alterations, ranging from charring to superficial and complete
85 calcination (Figure S3 F, Figure S4 B, E, & G, Figure S5 G). The presence of microscopic
86 charcoal and dark amorphous staining, especially in the lowermost layer I-09, also indicates fire
87 use activities at the site, possibly related to the observed heat treatment of silcrete at the site.
88 Silcrete and quartz microdebitage, showing a particular 'flaked' shape compared to the
89 geogenic rounded minerals/rocks, are also present (Figure S3 C&G). OES is another common
90 anthropogenic component, and fragments show a subangular to rounded shape (Figure S3
91 A&E, Figure S4 C, Figure S5 A, C, & D). A few OES fragments show a dark colour, potentially
92 as the result of charring of their organic content, and others show internal fractures (Figure S4
93 C, Figure S5 D). Finally, one iron-rich rock fragment was observed, potentially presenting a
94 piece of ochre (Figure S5 B).

95 These micromorphological observations on the sediments allow us to reconstruct the
96 anthropogenic and natural formation processes of I-08 and I-09, the Lower Deposits of the deep
97 sounding. The calcareous matrix, calcite crystals and limestone originate from the weathering of

98 the bedrock and colluvial deposition on the slope. The fine coating on sand sized components,
99 the occurrence of rounding and of soil aggregates from the plateau above the site suggest
100 transport processes (2). However, the high frequency of microscopic bones and their broad size
101 distribution, the rarity of components from the plateau, and that the fine coating is composed of
102 typical slope material all indicate limited transport on the slope in front of the shelter and support
103 the integrity of the archaeological record at the site. Post-depositional processes affecting the
104 archaeological record are limited to impact fractures, possibly from trampling, local cementation,
105 and gypsum formation. The latter two result from circulating water and later evaporation. There
106 is little difference between I-08 and I-09, which show the same general composition and
107 structures, as well as depositional and post-depositional processes. One difference, however, is
108 a darker colour of I-09 compared to I-08, resulting from an increase in microcharcoal in this
109 layer. This increase in microcharcoal may indicate an intensification of fire use activities at the
110 site at this time, but may also just reflect a local phenomenon in this layer. Generally, fire use
111 activities appear to be of different fire intensity or duration as reflected in the variable heating
112 signal recorded in the bones. As we have not yet discovered any *in situ* combustion features,
113 fire use interpretation remains limited. Regarding the disturbed part in one thin section from I-08,
114 this most likely presents an ancient biogenic structure, possibly an underground nest structure.
115 The observed structure does not, however, resemble the published microstructure of termite
116 mounds (3-6) or of underground bee nests (7), which are both known in the area.

117

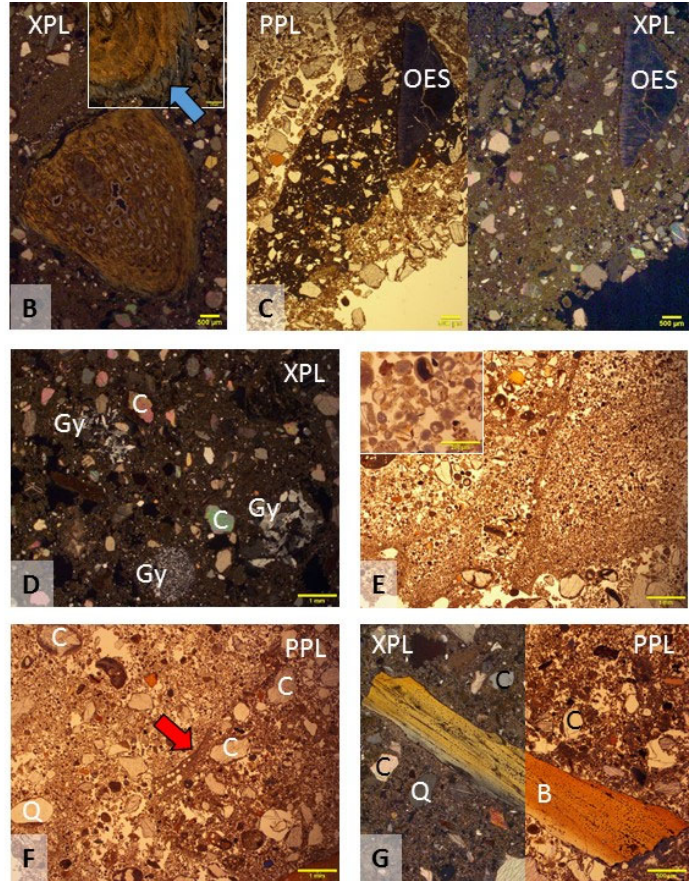
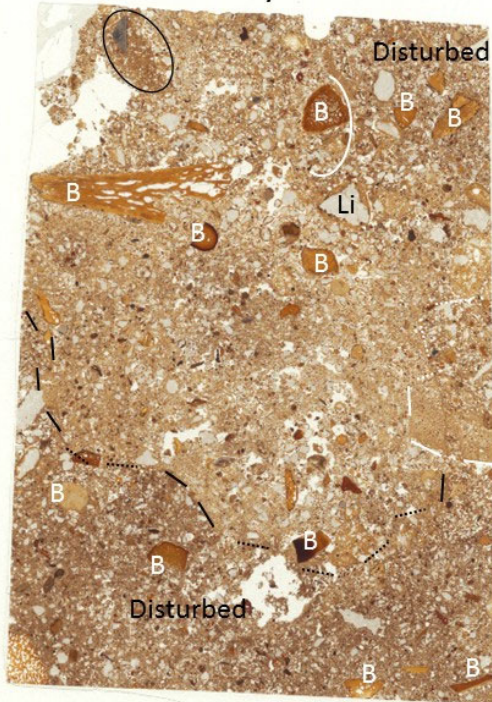


118

119 **Figure S3.** Micromorphology sample VR003 14 1 (I-08). (A) Scan of thin section VR 14 1 showing a
 120 homogenous appearance and random orientation of coarse grains. Coarse grains are mainly limestone
 121 and calcite crystals originating from limestone weathering (white grains) as well as quartz (also white
 122 grains, rarer than calcite), bones (almost all brown grains, larger ones labelled), ostrich eggshell and
 123 rarely teeth, speleothem pendants and aggregates. Two cemented areas are present (black circles), but
 124 only become visible at higher magnification (see B). (B) Cemented area showing a dark colour and clear
 125 boundaries to the surrounding matrix. The inlet at the upper right shows the dense microstructure in the
 126 cemented area, which otherwise does not differ from the surrounding matrix indicating *in situ* formation.
 127 Scale 500 µm, scale inlet 200 µm. (C) Sand to fine gravel sized grains, including bones, often exhibit a
 128 coating composed of fine material, a typical feature of slope deposits. The coating and the general matrix
 129 are composed of the same calcareous silt suggesting transport on the slope and not from the plateau
 130 above. Large grains such as limestone gravel, or elongated objects such as silcrete and ostrich eggshell,
 131 generally do not show coatings. Scale 500 µm. (D) A subrounded surface slack aggregate, enriched in
 132 organics and clay. This aggregate originates from the plateau above the site. Scale 500 µm. (E) *In situ*
 133 snapped ostrich eggshell below limestone. Note the coarse-crystalline nature of the limestone and a
 134 laminated pendant (arrow) formed on its surface. Scale 1 mm. (F) Calcined bone (grey colour). Scale
 135 200µm. (G) Quartz microdebitage with elongated shape and acute edges (arrow), indicating that this
 136 quartz presents a knapping by-product. Scale 500µm. Abbreviations used here and in subsequent
 137 figures: Agg = Aggregate, B = Bone, C = Calcite, Ch = Charcoal, Gy = Gypsum, Ir = iron rich rock, Li =
 138 Limestone, OES = Ostrich eggshell, OIL = Oblique Incident Light, PPL and XPL= plane and Cross
 139 Polarized Light, Q = Quartz, Si= silcrete, T = Tooth, OIL plane and Cross Polarized Light, Q = Quartz,
 140 Si= silcrete, T = Tooth, OIL.

141

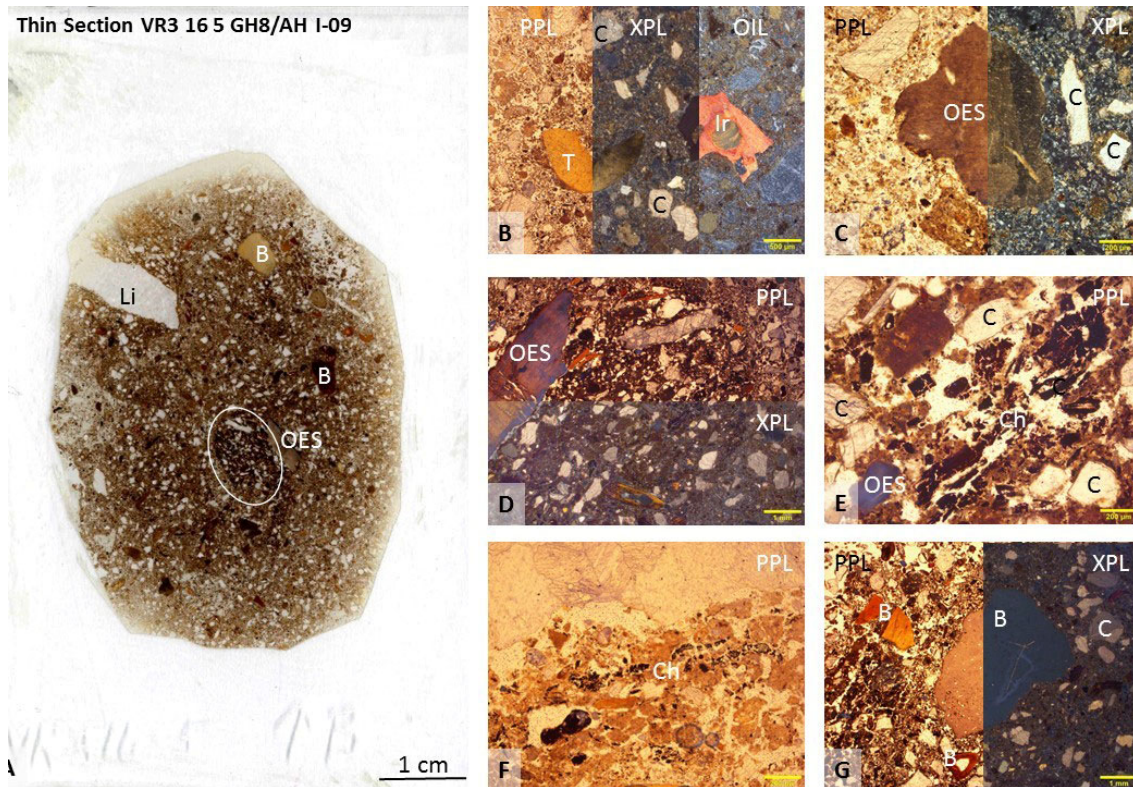
Thin Section VR3 15 8 GH8/AH I-09



142

A

143 **Figure S4.** Micromorphology sample VR003 15 8 (I-09). (A) Scan of thin section VR3 15 8 showing local
 144 disturbances (dark coloured areas at bottom and upper right corner of slide). The contact is clear (marked
 145 by lines) and the intact part shows similar characteristics to thin section VR 14 1. Also here the deposit
 146 shows a calcareous matrix with limestone gravel, calcite crystals, fine gravel to sand sized bones (almost
 147 all brown grains) and a cemented areas (black circle) occurs. (B) Superficially calcined bone (blue arrow
 148 in inlet indicating grey, calcined phase), suggesting short exposure to a high temperature fire. Scale 500
 149 µm, inlet 200 µm. (C) Cemented area with dark colour and clear boundaries to surrounding matrix, but
 150 showing same composition with calcareous silt (see XPL) and calcite crystals, bones and ostrich
 151 eggshell. Note also the internal fractures in the ostrich eggshell. Scale 500 µm. (D) Gypsum is present in
 152 variable forms with accumulations of lenticular crystals to rounded aggregates/rocks. Scale 1 mm. (E)
 153 Disturbed area with pellet structures, sorted for very fine sand, and fine coating of the wall, indicating a
 154 biogenic origin. Scale 1 mm. (F) Clear contact of the disturbed part with the intact part. Note a silty crust
 155 with vesicles here. Scale 1 mm. (G) Superficially calcined bone (grey colour) in the disturbed part of the
 156 thin section. Scale 500 µm.



157

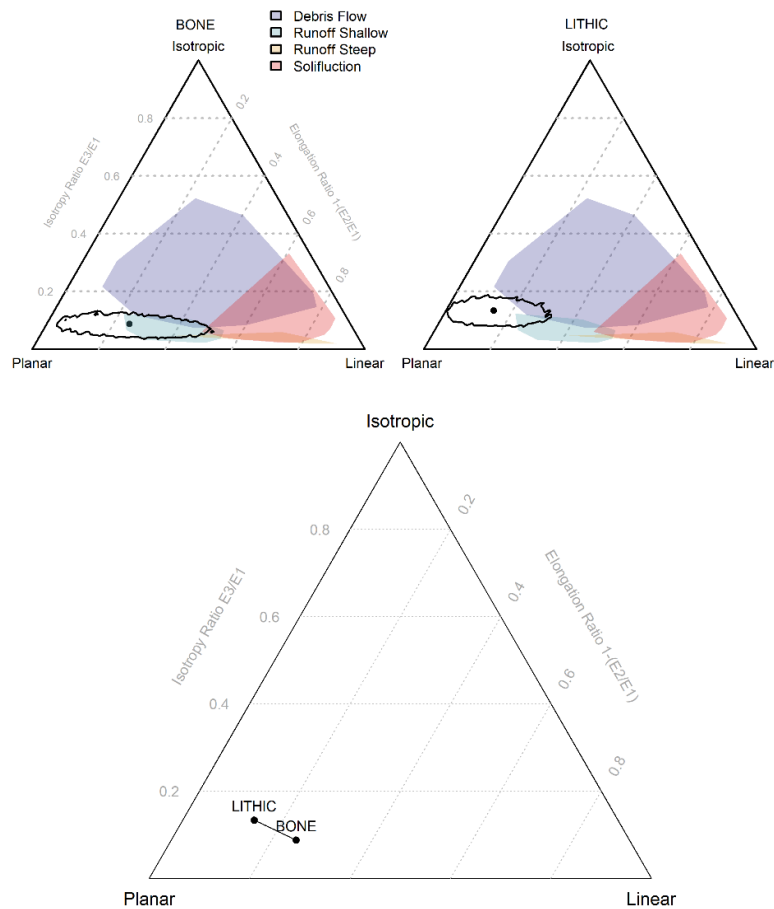
158 **Figure S5.** Micromorphology sample VR003 16 5 (I-09). (A) Scan thin section VR16 5 showing darker
 159 colour compared to the upper thin sections, resulting from microscopic charcoal and amorphous black
 160 staining in the matrix here (see E and F). Otherwise, the deposits show similar characteristics, with
 161 limestone and calcite crystals, many microscopic bones, a cemented area (white circle) and a
 162 homogenous, porphyric appearance. (B) Tooth (T) and an iron rich rock fragment, possibly ochre.
 163 Scale 500 μm . (C) Rounded ostrich eggshell suggesting transport. Scale 200 μm . (D) Cemented area
 164 next to an ostrich eggshell with internal fractures/dissolution traces. The fine material appears darker
 165 here due to increased density and black amorphous staining. Note also the bones in the cemented
 166 area. Scale 1 mm. (E) Details of cemented area with microscopic charcoal. Scale 200 μm . (F)
 167 Microscopic charcoal in the general matrix. Scale 200 μm . (G) Bone fragments, some heated (central
 168 grey) and others without heating alterations (brown). Scale 1 mm.

169

170 **Fabric analysis.** During excavation, elongated lithics and bones axis were plotted with two
 171 spatial points to record their orientation and slope. The three-dimensional plunge and
 172 bearing of each artefact was plotted in a Benn diagram along with comparative data for
 173 geological processes modelled by (8). Confidence intervals ($p = .95$) in the Benn diagrams
 174 were calculated using a permutation test developed by (9), which involves resampling the
 175 assemblage 10000 times and plotting contour lines that accounts for 95% of the resampled
 176 indices. Rayleigh and Kolmogorov-Smirnov tests were used to determine if the orientation
 177 (bearing) and slope (plunge) of artefacts differed significantly from a uniform distribution, and
 178 were run using the CircStats package in R. Mean slope values for the two-point objects
 179 (10.8°) do not deviate substantially from the low to moderate slope of the Lower Deposit
 180 sediments, and the artefacts show no preferential pattern in orientation.

181

182



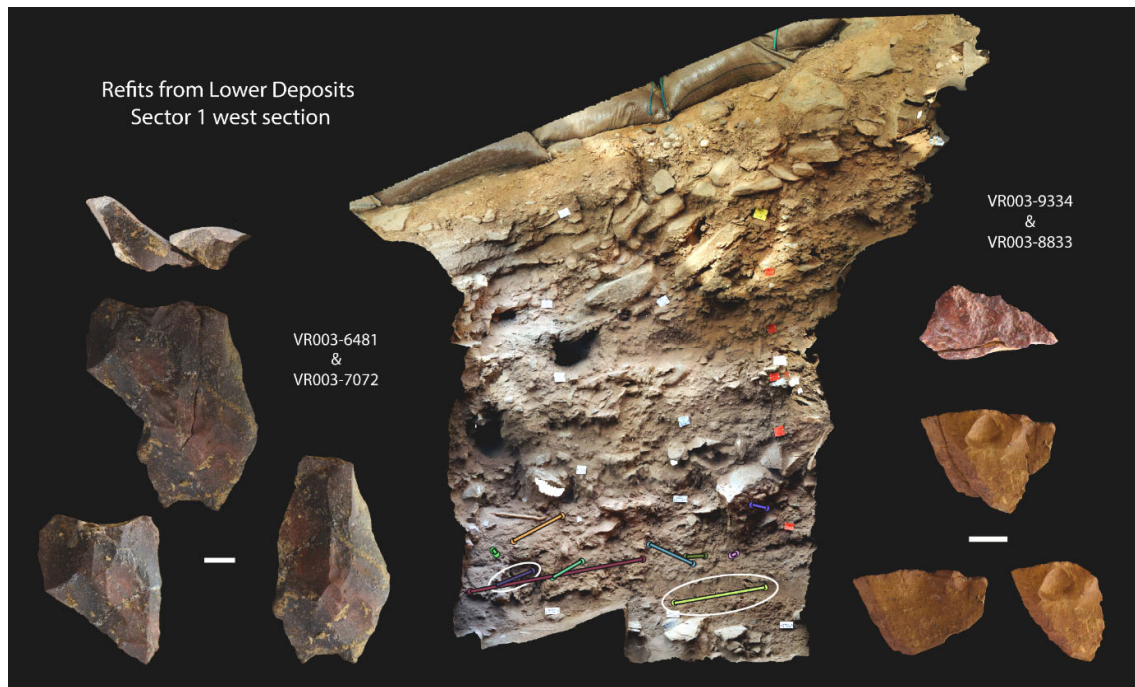
183

184 **Figure S6.** Benn diagrams for two-point lithics and bones from I-08 and I-09 against expectations for
 185 various depositional processes.

186

187

188 **Refits.** Refit analysis of lithic artefacts was used principally as a means of assessing the
189 integrity and slope of the archaeological deposits. Only silcrete and chert artefacts were
190 included, as these materials are visually diverse and distinctive, particularly when compared
191 to the other major materials in the assemblage (quartz, quartzite, and hornfels). A total of 12
192 refit sets was found in I-08 and I-09, comprising nine instances of sequential flake removals,
193 two sets of conjoining flake fragments, and one instance where two pieces of heat shatter
194 could be refit. Refits over short distances occur at various orientations (Figure S7). Refits
195 over long distances typically follow the slope of the surface and lower strata.



196
197 **Figure S7.** Distribution and orientation of lithic refit sets in I-08 and I-09, with indicative examples of
198 refitting flakes.

199 **Geochronology**

200 **Luminescence dating**

201 **Sample collection and preparation.** Samples were collected during the excavation of VR003
202 by hammering metal tubes into cleaned section faces. These tubes were sealed with adhesive
203 tape and wrapped in opaque plastic bags for transportation. Five samples were taken from
204 Sector III (inside the shelter), with the aim of replicating previously published ages for the
205 Howiesons Poort levels at VR003 (10). These published ages were younger than might be
206 expected based on the affinities of associated material, though the chronology for these
207 technocomplexes is contested (11, 12). A further four samples were taken from strata I-08 to
208 I-09 in Sector I (Main Area), the lowermost VR003 levels excavated so far, to establish the
209 age of this portion of the site.

210

211 In the laboratory, samples were processed under subdued red light. Sunlight exposed material
212 was removed from each end of the sample tube and retained for dose rate measurement.
213 Quartz and K-feldspar were extracted from the portion of each sample which had not been
214 exposed to sunlight since burial. Samples were initially wet-sieved to isolate the 212-180 μm
215 size fraction. This removes large bedrock clasts from the sample before acid treatment,
216 meaning that the possibility of incorporating grains liberated by dissolution of the bedrock was
217 minimized. Carbonates and organic matter were subsequently removed from the 212-180 μm
218 fraction using 1M HCl and H_2O_2 respectively. The resulting material was re-sieved at 180 μm .
219 Density separations at 2.72, 2.62, 2.58 and 2.53 g/cm^3 (13) were used to isolate quartz (2.62-
220 2.72 g/cm^3) and K-feldspar (2.53-2.58 g/cm^3). The quartz fraction was etched in HF (23M HF
221 for 60 min followed by a 10M HCl rinse) and sieved at 150 μm to remove partially dissolved
222 feldspars. Samples were stored in opaque containers prior to measurement.

223

224 **Environmental dose rate calculation.** For HF acid etched sand-sized quartz grains, the
225 environmental dose rate consists of external beta, gamma and cosmic ray components. The
226 dose rate to unetched sand-sized K-feldspar also contains an external alpha component and
227 an internal beta component.

228

229 External alpha, beta and gamma dose rates were determined using alpha counting, beta
230 counting and field gamma-spectrometry respectively. Alpha and beta counting was performed
231 on dried, homogenised sub-samples of the light-exposed material removed from the sample
232 tube prior to extraction of the dating sample. Uranium and thorium concentrations were
233 calculated for each sample using thick-source alpha counts obtained using Daybreak Model
234 583 alpha counters. External alpha dose rates were calculated from these data using standard
235 conversion factors (14) and assuming secular equilibrium in the U and Th decay series. Beta

236 dose rates were measured with a Risø GM-25-5 low-level beta counting system (15) using
 237 MgO and Volkagem (16) loess standards. Gamma dose rates were measured with an EG&G
 238 Ortec digiDart-LF gamma-spectrometer using the “threshold” method. External dose rates
 239 were corrected for moisture content (10±5%), attenuation of alpha (17) and beta (18) radiation
 240 due to grain size and alpha efficiency, using an a-value of 0.11±0.03 (19). The internal dose
 241 rate to K-feldspar grains was calculated assuming a K concentration of 12±1% and a K/Rb
 242 concentration ratio of 270:1 (20). The assumed K concentration encompasses (at 2σ) nearly
 243 the full range of K concentrations (9-14%) measured for single-grains of K-feldspar emitting
 244 detectable luminescence signals (21-25) and is consistent with the widely adopted value of
 245 12.5±1.0% (26). Cosmic ray dose rates for the Main Area (Sector I) samples (the K-feldspar
 246 samples) were calculated using site location (31.5°S, 18.5°E, 50 m elevation) and present day
 247 sediment burial depths, assuming a sediment overburden density of 1.8±0.1 g/cm³. However,
 248 calculation of the cosmic dose rates to the Sector III samples (the quartz samples) was
 249 complicated by their location behind the present-day dripline. For the purposes of calculation
 250 the cave was approximated to have an opening 120° wide and a roof consisting of a 3.5 m
 251 thickness of rock with a density of 2.5 g/cm³. The dose rate at the surface of the sediment 1
 252 m behind the dripline (the approximate sampling location) was then calculated using the cos²Φ
 253 zenith angular distribution of cosmic rays (27). For each sample, this surface cosmic dose rate
 254 was modified according to the present-day burial depth using an overburden density of 1.8±0.1
 255 g/cm³. Total dose rates were calculated using the DRAC dose rate calculator (28). Dose rates
 256 are presented in Table S1. Here and throughout the luminescence Supplementary
 257 Information, uncertainties are given at 1σ except where otherwise stated.

258
 259
 260

Table S1. Sample depths and dose rates for VR003 samples. Depths are given below present-day sediment surface.

Stratum	Sample (mineral) ^a	Sample depth (m)	External dose rate (Gy/ka) ^b				Total dose rate, D _r (Gy/ka)
			Alpha	Beta	Gamma	Cosmic	
Sector III ‘Inside the Shelter’							
17	8238 (Q)	0.67±0.1 ^c	-	0.70±0.08	0.68±0.07	0.11±0.01	1.49±0.11
17	2885 (Q)	0.67±0.1 ^c	-	0.87±0.10	0.66±0.07	0.11±0.01	1.64±0.12
18	2883 (Q)	0.72±0.1 ^c	-	1.01±0.12	0.68±0.07	0.11±0.01	1.80±0.14
20	2881 (Q)	0.80±0.1 ^c	-	0.98±0.12	0.70±0.07	0.11±0.01	1.78±0.14
20	8235 (Q)	0.80±0.1 ^c	-	1.03±0.12	0.94±0.09	0.11±0.01	2.08±0.15
Sector I ‘Main Area’							
7/8	2432 (KF)	1.2±0.2	0.06±0.01	0.70±0.05	0.57±0.04	0.18±0.02	2.30±0.11 ^d
8	8710 (KF)	1.4±0.2	0.06±0.01	1.09±0.08	0.64±0.05	0.17±0.02	2.74±0.13 ^d
9	8678 (KF)	1.7±0.2	0.06±0.01	1.15±0.10	0.60±0.04	0.17±0.02	2.76±0.14 ^d
10	11918 (KF)	1.9±0.2	0.05±0.01	0.67±0.05	0.50±0.04	0.16±0.02	2.17±0.11 ^d

261 ^aQ = quartz, KF = K-feldspar. ^bExternal dose rates after correction for sample moisture content (10±5%)
 262 and, where appropriate, corrected for attenuation due to grain size and alpha efficiency. ^cDepth below
 263 sediment surface, excluding the 3.5 m cave roof thickness ^dTotal dose rates are the sum of external
 264 dose rates plus an internal dose rate contribution of 0.79±0.08 Gy/ka.
 265

266 **Luminescence measurement equipment.** Luminescence measurements were made on
267 quartz extracted from Sector III samples, while K-feldspar was used for Sector I material. This
268 approach was adopted since the Sector I samples were presumed to be considerably older
269 than those from Sector III. K-feldspars are able to absorb far larger radiation doses than quartz
270 before “saturation” occurs, enabling them to yield older ages before the upper limit of the
271 technique is reached.

272

273 Individual grains of quartz or K-feldspar were mounted in aluminium discs drilled with 100
274 holes, each 300 μm deep and 300 μm in diameter. All luminescence measurements presented
275 in this study were carried out using a Risø TL/OSL-DA-15 automated dating system (29), fitted
276 with a dual laser single-grain attachment (30, 31). Individual grains were stimulated using
277 either a focused 10 mW Nd:YVO₄ solid-state diode-pumped green (532 nm) laser for quartz
278 OSL or a 140 mW TTL modulated infra-red (IR, 830 nm) laser with a Schott RG 780 longpass
279 filter mounted in the beamline for K-feldspar pIRIR. Simultaneous illumination of all grains on
280 a disc was carried out using either blue (470 nm) or IR (870 nm) light emitting diodes (LEDs).
281 Luminescence was detected using an Electron Tubes Ltd 9235QB15 photomultiplier tube
282 shielded by Hoya U-340 filters when measuring quartz and Schott BG3 and BG39 filters when
283 measuring K-feldspar. Irradiation was carried out using a 1.48 GBq ⁹⁰Sr/⁹⁰Y beta source. This
284 source is calibrated relative to the National Physical Laboratory, Teddington ⁶⁰Co γ -source
285 (Hotspot 800) (32). Due to the spatial inhomogeneity of beta emitters across the active face
286 of our ⁹⁰Sr/⁹⁰Y beta source, it was necessary to calibrate the dose rate to each individual grain
287 position on a single-grain disc (33). All single-grain discs were placed into the Risø instrument
288 at the same angle relative to the ⁹⁰Sr/⁹⁰Y beta source. For the instrument used in this study,
289 the sample discs rotated $0.04 \pm 0.03^\circ$ per measurement cycle within the single-aliquot
290 regenerative-dose method (see below). Consequently, it is possible to accurately correct for
291 the effects of inhomogeneity in our ⁹⁰Sr/⁹⁰Y beta source by applying a grain position correction
292 to each equivalent dose. Position-corrected equivalent doses were used in all age
293 calculations.

294

295 **The single-aliquot regenerative-dose method applied to quartz and K-feldspar.**
296 Equivalent doses (D_e) were determined using the single-aliquot regenerative-dose (SAR)
297 method (34). This method allows an independent estimate of D_e to be generated for each
298 aliquot or mineral grain measured, though in practice single-grain measurements suffer a high
299 rejection rate. The SAR technique involves making a series of paired measurements of
300 luminescence intensity. The first measurement in each pair gives the natural (L_n) or
301 regenerated (L_x) luminescence intensity, while the second measurement (T_x) gives the
302 luminescence intensity in response to a fixed test dose. T_x is used to monitor changes in

303 sensitivity (luminescence per unit dose) during the measurement sequence. By dividing the
 304 natural or regenerated luminescence intensities by their respective test dose intensity (i.e.
 305 L_n/T_n or L_x/T_x), a sensitivity-corrected luminescence response is determined. All single-grain
 306 quartz measurements presented in this study were made using the SAR procedure and
 307 experimental conditions detailed in Table S2.

308
 309
 310

Table S2. The SAR measurement sequence used to produce single-grain equivalent dose estimates from quartz from VR003.

Step	a) Single-grain quartz OSL
1	Give regenerative dose, D_i^a
2	Preheat 1 (260 °C for 10 s) ^b
3	Green laser stimulation (125 °C, 2 s), L_x^c
4	Give test dose, D_t (~10 Gy)
5	Preheat 2 (220 °C for 10 s)
6	Green laser stimulation (125 °C, 2 s), T_x
7	Return to step 1

311 ^a In the first cycle, where the natural luminescence intensity is observed, $D_i = 0$ Gy. ^b The suitability of
 312 preheat 1 and 2 temperatures for measuring quartz from VR003 was assessed by performing single-
 313 grain dose recovery tests (35) on 600-800 grains per sample. All samples yielded dose recovery
 314 ratios (measured D_e /given dose) consistent with unity at 2σ , implying that the measurement conditions
 315 used were appropriate. ^c The luminescence signal (L_x or T_x) was that recorded during the first 0.3 s of
 316 stimulation, with a background signal from the last 0.3 s of stimulation subtracted.

317
 318
 319

Table S3. The SAR measurement sequence used to produce a) single-grain equivalent dose estimates and b) fading rates from K-feldspars from VR003.

Step	a) Single-grain K-feldspar pIRIR	b) K-feldspar pIRIR fading rates
1	Give regenerative dose, D_i^a	Give regenerative dose (~50 Gy) ^c
2	Preheat 1 (255 °C for 60 s)	Preheat 1 (255 °C for 60 s)
3	IR diode stimulation (60 °C for 200 s)	Pause ^d
4	IR laser stimulation (225 °C, 2 s), L_x^b	IR diode stimulation (60 °C for 200 s)
5	IR diode stimulation (225 °C for 500 s)	IR diode stimulation (225 °C for 200 s), $L_x^{e,f}$
6	Give test dose, D_t (~50 Gy)	Give test dose, (~50 Gy)
7	Preheat 2 (255 °C for 60 s)	Preheat 2 (255 °C for 60 s)
8	IR diode stimulation (60 °C for 200 s)	IR diode stimulation (60 °C for 200 s)
9	IR laser stimulation (225 °C, 2 s), T_x^b	IR diode stimulation (225 °C for 200 s), T_x^e
10	IR diode stimulation (225 °C for 500 s)	IR diode stimulation (290 °C for 150 s)
11	Return to step 1	Return to step 1

320 ^a In the first cycle, where the natural luminescence intensity is observed, $D_i = 0$ Gy. ^b The luminescence
 321 signal (L_x or T_x) was that recorded during the first 0.3 s of stimulation, with a background signal from
 322 the last 0.3 s of stimulation subtracted. ^c Prior to the first measurement cycle, aliquots were illuminated
 323 for 150 s at 290 °C to remove any residual signal remaining after completion of the single-grain
 324 measurement sequence. ^d For each aliquot, ten measurements were made, of which three were prompt
 325 (no pause), three were made after a 1 hour pause, and two were made after 10 and 100 hour pauses.
 326 ^e The luminescence signal (L_x or T_x) was that recorded during the first 50 s of stimulation, with a
 327 background signal from the last 50 s of stimulation subtracted. ^f The optical wash incorporated into the
 328 single-grain measurement sequence was omitted here since IR diodes illuminate the disc more evenly
 329 than the single-grain laser, minimising the potential to carry signal over into the test dose measurements
 330 (36).

331
 332
 333
 334
 335

K-feldspars were measured using a post-infrared, infrared stimulated luminescence (pIRIR)
 measurement sequence (Table S3a). In this sequence, the sample is illuminated using IR
 diodes for 200 s prior to measurement of the signal (L_x or T_x) from individual grains using an
 IR laser. This procedure removes luminescence signals which are prone to “fading”, which

336 could otherwise lead to underestimation of D_e (37, 38). In addition, samples underwent an
 337 elevated temperature (225 °C for 500 s) IR diode stimulation after measurement of L_x or T_x , to
 338 prevent carry-over of charge from one measurement to the next (36). Although VR003
 339 samples yielded limited K-feldspar, dose recovery tests (39) were performed on three
 340 multigrain aliquots of each of samples VR003-8678 and VR003-8710, and 600 individual
 341 grains of sample VR003-2432. These tests yielded dose recovery ratios (measured D_e /given
 342 dose) of 1.01 ± 0.03 , 0.98 ± 0.03 and 0.99 ± 0.01 respectively, implying that the measurement
 343 conditions used were appropriate.

344

345 It has been observed widely that a large proportion of quartz and K-feldspar grains either do
 346 not yield a measureable luminescence signal, or display luminescence characteristics which
 347 indicate that they are unsuitable for age determination. Consequently, most dating studies
 348 adopt rejection criteria which exclude these grains. In the present study we adopted rejection
 349 criteria based on those used to analyse the very large single-grain dataset from Denisova
 350 Cave, southern Siberia (24). In this analysis, grains were rejected where one or more of the
 351 following conditions were met:

- 352 a) The initial T_n signal is less than 3σ above the corresponding background count, or the
 353 relative error on T_n is $>20\%$.
- 354 b) The recycling ratio (34) differs from unity by greater than 2σ .
- 355 c) The IR-depletion ratio (40) is more than 2σ below unity (this criterion excludes feldspar
 356 grains, and was only used for analysing quartz datasets).
- 357 d) Recuperation is high. This criterion was met where L_x/T_x for the 0 Gy regeneration point
 358 is greater than 5 % of L_x/T_x for the maximum regenerative dose.
- 359 e) The L_x/T_x ratios are too scattered to be reliably fitted with a curve. This criterion is met
 360 where the figure-of-merit (FOM) value (41, 42) exceeds 10%. The FOM is defined as:

361
$$FOM(\%) = \frac{\sum_{i=1}^n |y_i^o - y_i^f|}{\sum_{i=1}^n y_i^f}$$

362 where y_i^o and y_i^f denote the i^{th} observed and fitted values respectively.

- 363 f) The L_n/T_n ratio is statistically consistent with, or higher than, the saturation level of the
 364 corresponding dose response curve (DRC), so that a finite D_e value and error cannot
 365 be obtained.
- 366 g) The D_e value is obtained by extrapolation of the fitted DRC, rather than interpolation
 367 among the regenerative dose signals.
- 368 h) The grain has a negative D_e value consistent with zero. This criterion was used to
 369 identify modern contaminants introduced during sampling, and was only applied to the
 370 quartz datasets.

371 Application of the rejection criteria was achieved using the function `calSARED()` provided in
 372 the R package *numOSL* (43, 44), with DRCs fitted using a general-order kinetic fit (45). For
 373 each accepted grain, the standard error associated with the D_e determination was estimated

374 using a 1000 iteration Monte Carlo simulation. Rejection criteria were applied to grains in the
 375 order listed above, and only one cause for rejection was noted per grain (Tables S4 and S5).

376
 377
 378

Table S4. The number of quartz grains which were measured, rejected after application of rejection criteria, and accepted for inclusion in the calculation of the burial dose.

Sample (VR003-...)	8238	2885	2883	2881	8235
Stratum	III-17	III-17	III-18	III-20	III-20
Total number of grains measured ^a					
	2800	2800	2800	2500	2800
Grains rejected for the following reasons					
a) T_n signal $<3*$ background or relative error $>20\%$	2362	2285	2071	1927	2201
b) Poor recycling ratio	66	108	129	165	83
c) IR-depletion ratio	36	23	31	18	39
d) 0 Gy dose $>5\%$ of L_x/T_x for the maximum dose	4	9	6	3	7
e) FOM $>10\%$	19	28	16	29	12
f) $L_n/T_n > DRC$	68	62	138	145	159
g) D_e obtained by extrapolation	24	41	122	33	90
h) Negative D_e value consistent with zero	13	14	20	8	29
Sum of rejected grains					
	2592	2570	2533	2328	2620
Acceptable individual D_e values					
	208	230	267	172	180

379 ^a Gives the number of grain positions measured i.e. 100 per single-grain disc. Discs were not inspected
 380 after use to assess the proportion of unoccupied grain positions, but a value ~3% has been reported by
 381 the same operator (SJA) when measuring similar material.

382
 383
 384

Table S5. The number of K-feldspar grains which were measured, rejected after application of rejection criteria, and accepted for inclusion in the calculation of the burial dose.

Sample (VR003-...)	2432	8710	8678	11918
Stratum	I-07/8	I-08	I-09	I-09
Total number of grains measured ^a				
	1200	1200	1600	1200
Grains rejected for the following reasons				
a) T_n signal $<3*$ background or relative error $>20\%$	843	912	1285	868
b) Poor recycling ratio	31	31	40	43
c) IR-depletion ratio	Omitted for K-feldspar			
d) 0 Gy dose $>5\%$ of L_x/T_x for the maximum dose	6	5	4	9
e) FOM $>10\%$	71	74	127	61
f) $L_n/T_n > DRC$	0	1	2	0
g) D_e obtained by extrapolation	2	10	4	2
h) Negative D_e value consistent with zero	Omitted for K-feldspar			
Sum of rejected grains				
	953	1033	1462	983
Acceptable individual D_e values				
	247	167	138	217

385 ^a Gives the number of grain positions measured i.e. 100 per single-grain disc. Discs were not inspected
 386 after use to assess the proportion of unoccupied grain positions, but a value ~3% has been reported by
 387 the same operator (SJA) when measuring similar material.

388
 389
 390
 391
 392
 393

To determine the age of a sample which has been measured using single-grain luminescence techniques, it is first necessary to analyse the distribution of individual D_e values in order to generate a single burial dose (D_b). Initially, the Central Age Model (CAM) (46) was used to calculate D_b for both quartz and feldspar samples using the function `calc_CentralDose()` in the R package *Luminescence* (47). The CAM generates D_b on the assumption that the dispersion

394 of measured D_e values is explained by the overdispersion parameter (OD, the relative
395 standard deviation of the true paleodoses) and measurement uncertainties. This model is
396 appropriate for samples where the luminescence signal of all constituent grains was fully
397 bleached prior to deposition, and where no post-depositional mixing has occurred.

398

399 For the quartz (Sector III) Howiesons Poort and post-Howiesons Poort samples from inside
400 the shelter, overdispersion values ranged between $30\pm 2\%$ and $55\pm 2\%$, with a mean value of
401 45%. These values are higher than the $<20\text{-}30\%$ overdispersion typically reported for well-
402 bleached unmixed quartz samples e.g. (48), implying that some degree of post-depositional
403 mixing might have occurred. This inference is supported by the observation of minor
404 bioturbation by roots and insects during micromorphological analysis of Sector III sediments
405 (1). Consequently, D_b for these samples was determined using the Finite Mixture Model (FMM)
406 (49). The FMM is appropriate for samples containing more than one population of grains, for
407 example where bioturbation has occurred. The use of overdispersion alone to determine
408 whether the FMM should be applied to a sample has been criticised (50) on the grounds that
409 high overdispersion values can be caused by spatially variable β dose rates (beta
410 microdosimetry) resulting from the presence of potassium feldspars. We discount beta
411 microdosimetry as the main cause of the high overdispersion observed for VR003 quartz
412 samples since this phenomenon is most pronounced where total dose rates are low (<1 Gy/ka)
413 and the sediment is coarse grained, whereas the dated horizons have dose rates ranging from
414 1.5-2.1 Gy/ka (Table S1) and contain abundant silt-sized material (1). It has also been
415 suggested that the FMM can identify dose components that do not result from post-
416 depositional mixing, leading to the calculation of incorrect ages (51). This possibility has been
417 discounted here both because it is contested (52) and because micromorphological analysis
418 of Sector III sediments (1), implies that post-depositional mixing has occurred.

419

420 The FMM was run using two to six D_e components and an overdispersion value of 25%, the
421 latter being sufficiently large to allow for the effects of beta microdosimetry (48). The minimum
422 number of statistically supported D_e components was determined for each dataset by
423 optimising the Bayesian Information Criterion (BIC) and the maximum log likelihood (l_{ik}) using
424 the function `calc_FiniteMixture()` in the R package *Luminescence* (47). For the purposes of
425 age calculation, D_b was the equivalent dose for the component containing the largest
426 proportion of accepted grains. Equivalent dose distributions and FMM components for the
427 quartz samples are shown in Figure S8 and Table S6.

428

429 For each quartz dataset, analysis using the FMM indicates that the majority of grains (74-94%)
430 belong to the single population with the highest equivalent dose. One or more lower-dose

431 components are required, implying that post-depositional processes, presumably minor root
432 or insect bioturbation, have intruded a small proportion of younger grains. This inference is
433 consistent with the published micromorphological analysis of Sector III samples (10).

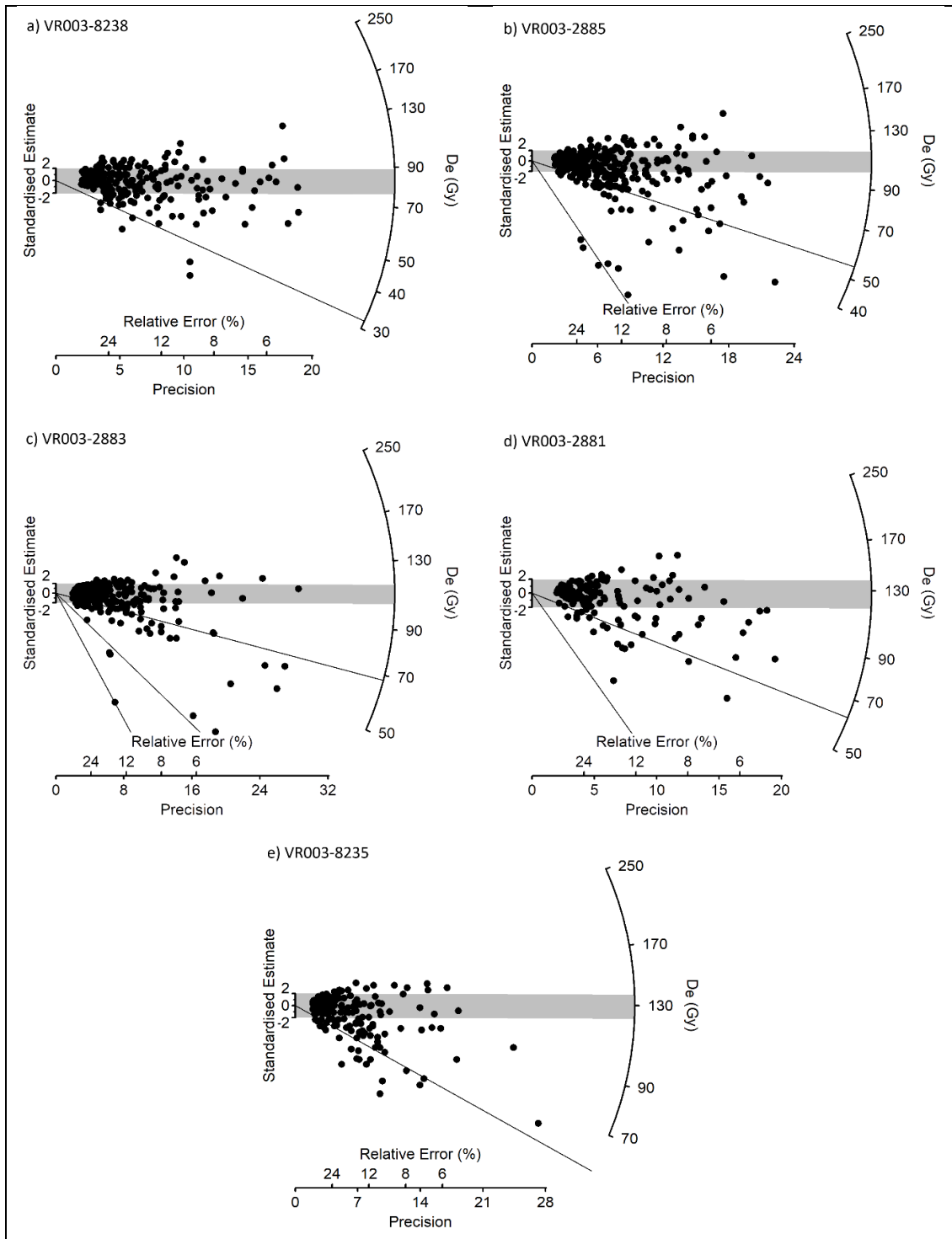
434

435 Since a number of grains were excluded from calculation of the burial dose due to natural
436 signal saturation (rejection criterion f , Table S4) it is necessary to demonstrate that the
437 omission of these data does not bias D_b (51). To test this possibility the quartz datasets were
438 reanalysed, this time using an additional rejection criterion. Briefly, luminescence data for each
439 grain were fitted using a single saturating exponential passing through the origin i.e. $L_x/T_x =$
440 $a[1-\exp(-D/D_0)]$, where L_x/T_x is the sensitivity corrected luminescence intensity, a is the
441 saturation value and D_0 is a measure of the curvature of the dose response curve. Equivalent
442 doses (CAM and FMM) were then calculated after rejecting grains with D_0 below a threshold
443 value. This process was repeated with the D_0 threshold ranging from 0 Gy (no grains rejected
444 due to the D_0 criterion) to 150 Gy in 10 Gy increments. Two recent studies using this approach
445 (51, 53) have shown that dose recovery ratios increased as the D_0 threshold increased,
446 reaching a plateau consistent with unity, after which no further significant changes were
447 observed. Similarly, when performing this analysis on independently dated samples, D_b for the
448 plateau was consistent with the expected burial dose based on their known age (Thomsen et
449 al., 2016).

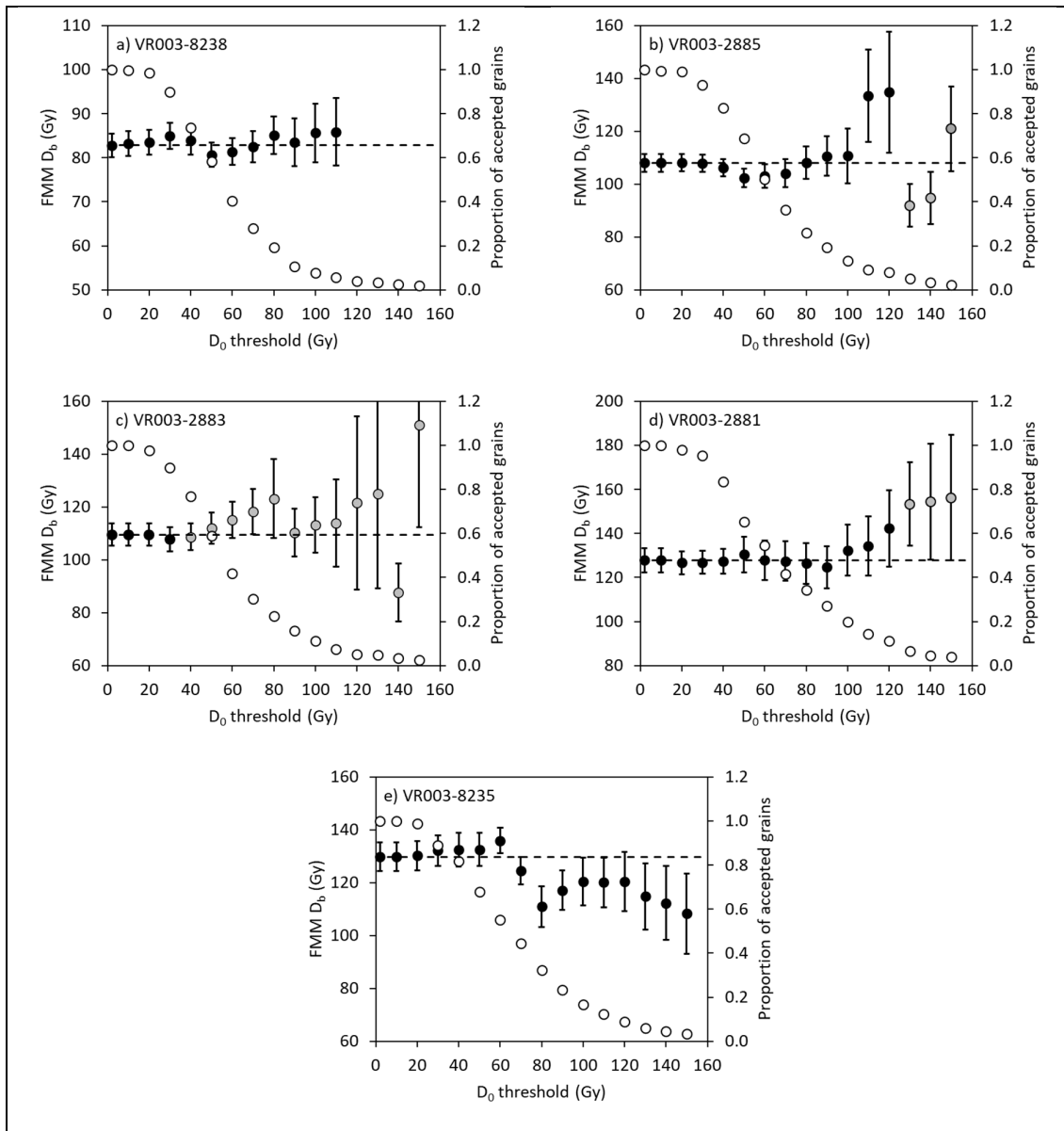
450

451 Plots of D_b (CAM and FMM) versus D_0 threshold are presented for each quartz sample in
452 Figure S9. For all samples, irrespective of the D_0 threshold applied, D_b is consistent with that
453 calculated without application of the D_0 rejection criterion at 2σ . Furthermore, only one sample
454 (VR003-2881) shows a systematic rise in D_b with increasing D_0 threshold, the pattern
455 suggested to indicate burial dose underestimation due to the onset of saturation in single-grain
456 datasets (Thomsen et al., 2016; Guo et al., 2017). In fact, the FMM calculated burial dose is
457 remarkably consistent with increasing D_0 threshold despite an order of magnitude reduction in
458 the number of accepted grains (all samples) and a change in the minimum number of
459 statistically supported components (samples VR03-2885, -2883, -2881). A similar pattern is
460 noted with the CAM D_b values (not shown), though as outlined above, this is not expected to
461 yield the most accurate estimate of the true burial dose. Consequently, we find no evidence
462 that more accurate D_b values will be obtained by applying an additional grain rejection criterion
463 based upon a D_0 threshold. Hereafter, we calculate ages for the VR003 quartz samples using
464 D_b obtained from the FMM without application of a D_0 rejection criterion.

465



466 **Figure S8.** Single-grain quartz D_e distributions for a) VR003-8238, b) VR003-2885, c) VR003-2883, d)
 467 VR003-2881 and VR003-8235, associated with Howiesons Poort and overlying post-Howiesons Poort
 468 strata inside the shelter (see Figure S1 for locations). Each point represents an individual grain. The
 469 grey bars are centered on D_b , the FMM component containing the majority of accepted grains, and all
 470 points that lie within the bars are consistent (at 2σ) with this dose. One low-dose grain has been omitted
 471 from each of panels b (4.1 ± 0.2 Gy) and d (6.4 ± 0.4 Gy) to allow the main component to be displayed on
 472 an appropriately scaled radial axis.
 473

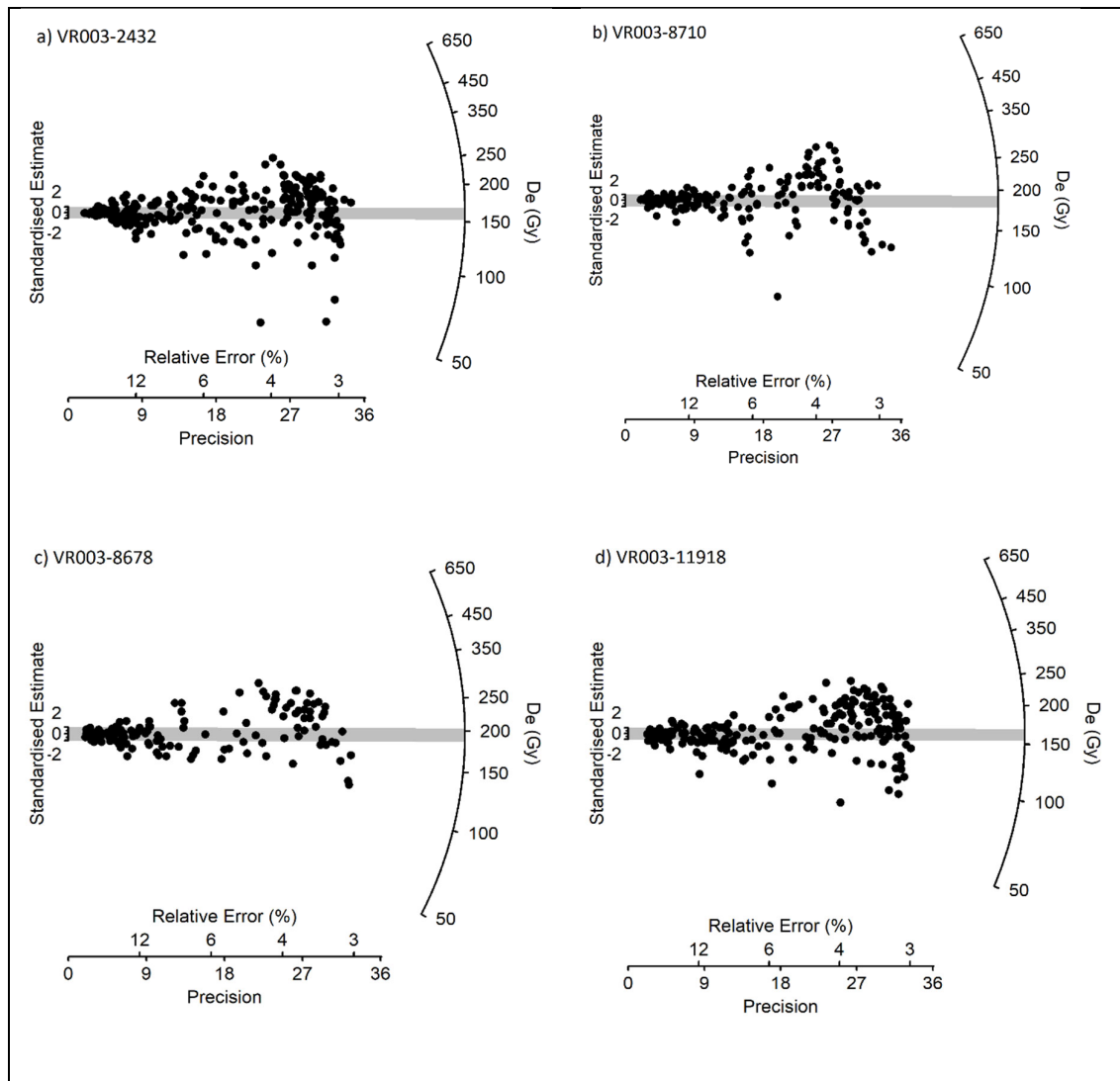


474 **Figure S9.** The main FMM component D_b (closed circles with 1σ uncertainties) and the corresponding
 475 proportion of accepted grains (open circles) plotted as a function of the D_0 threshold value. The
 476 proportion of accepted grains is calculated as the number of grains accepted using the threshold D_0
 477 divided by the number accepted where no threshold is applied. Uncertainties on D_b are 1σ and do not
 478 include the instrument's beta source calibration error (3%) since these are common to all quantities
 479 being compared. Closed circles filled in black represent FMM D_b values where the minimum number of
 480 statistically supported components equals that where no D_0 rejection criterion is applied, whereas those
 481 filled in grey represent D_b values calculated where fewer components are recognised. For sample
 482 VR003-8235 the FMM yields two identical components when the D_0 threshold exceeds 110 Gy, implying
 483 that only one component is present. No data are plotted for these points. The dashed lines indicate D_b
 484 where no D_0 rejection criterion is applied, and is the value used to calculate burial ages for the quartz
 485 (Sector III) samples.
 486

487 For the K-feldspar (Sector I) samples in the Main Area, overdispersion values ranged from
 488 $35\pm 2\%$ to $38\pm 2\%$. These values are consistent with well-bleached unmixed K-feldspar

489 samples, so the CAM was deemed appropriate for calculation of D_b . Equivalent dose
 490 distributions for the K-feldspar samples are shown in Figure S10.

491



492 **Figure S10.** Single-grain K-feldspar D_e distributions for a) VR003-2432, b) VR003-8710, c) VR003-
 493 8678 and d) VR003-11918 samples, taken from strata I-08 to I-09 in the Main Area. Each point
 494 represents an individual grain. The grey bars are centered on the CAM D_b and all points that lie within
 495 the bars are consistent (at 2σ) with this dose.

496

497 **Fading correction and ages.** Luminescence ages are calculated by dividing the burial dose,
 498 D_b by the total dose rate D_r . For quartz samples, the resulting age requires no subsequent
 499 correction. However, where feldspars exhibit measurable fading, it is necessary to correct this
 500 initial age. Fading rates were assessed using the measurement sequence outlined in Table
 501 S3b. These measurements were made on a subset ($n=32$) of the sample discs after
 502 completion of D_e measurements, but measurements and data analysis were conducted on
 503 bulk signals from each disc rather than those from individual grains. Fading rates (g -values
 504 normalised to t_c of 2 days) were calculated in Analyst v4.31.9 (54). Mean g -values for each

505 sample were consistent with the mean for all measured aliquots (1.9 ± 0.1 %/decade), and this
 506 value was used to correct each K-feldspar age. Fading corrections (55) were performed using
 507 the `calc_FadingCorr()` function in the R package *Luminescence*. CAM burial doses, dose rates
 508 and fading-corrected ages for the K-feldspar samples are presented in Table S7, while FMM
 509 components, equivalent doses, dose rates and ages for the quartz samples are presented in
 510 Table S6.

511
 512
 513

Table S6. Single-grain FMM components, burial doses, dose rates and ages for the Sector III quartz samples taken inside the shelter.

Stratum	Sample (VR003...)	Mineral ^a	Component ^b (number/%)	D _e (Gy) ^c	D _r (Gy/ka)	Age (ka) ^d
17	8238	Q	1/94 2/6	82.8±2.7 31.8±6.8	1.49±0.11	55.7±4.4 (8.8)
17	2885	Q	1/77 2/21 3/2	108±3 54.6±6.1 5.0±0.6	1.64±0.12	66.1±5.3 (10.6)
18	2883	Q	1/76 2/21 3/2 4/1	110±4 68.1±6.1 19.6±2.6 4.0±1.2	1.80±0.14	60.8±5.2 (10.4)
20	2881	Q	1/81 2/18 3/1	128±5 62.8±7.1 10.2±2.0	1.78±0.14	71.6±6.2 (12.4)
20	8235	Q	1/74 2/26	130±5 56.4±4.4	2.08±0.15	62.5±5.1 (10.2)

514 ^a Q = quartz, KF = K-feldspar. ^b Component number ranked from highest to lowest D_e. ^c The bold D_e for
 515 each sample is the burial dose (D_b) used to calculate the age. ^d Ages, with 1σ uncertainties and 2σ
 516 uncertainties in parentheses.

517
 518
 519

Table S7. Single-grain CAM burial doses, overdispersion, dose rate and ages for the Sector I K-feldspar samples in the Main Area.

Stratum	Sample (VR003-...)	Mineral ^a	OD (%) ^b	D _b (Gy) ^c	D _r (Gy/ka)	Age (ka) ^d
I-07/08	2432	KF	38±2	162±4	2.30±0.11	84.7±4.7 (9.4)
I-08	8710	KF	37±2	185±6	2.74±0.13	80.8±4.6 (9.2)
I-09	8678	KF	35±2	196±6	2.76±0.14	84.9±5.0 (10.3)
I-09	11918	KF	36±2	163±4	2.17±0.11	89.9±5.0 (10.1)

520 ^a Q = quartz, KF = K-feldspar. ^b OD = overdispersion. ^c D_b is the measured value and has not been
 521 corrected for the effects of fading. ^d Fading corrected ages, with 1σ uncertainties and 2σ uncertainties
 522 in parentheses.

523

524 **Discussion.** The K-feldspar ages from the Lower Deposits at VR003 are stratigraphically
 525 consistent, and indicate that sediments from I-08 to I-09 accumulated in late MIS 5. The quartz
 526 ages from Sector III inside the shelter are also stratigraphically consistent, ranging from
 527 55.7±4.4 ka (VR003-8238 in III- 17) to 71.6±6.2 ka (VR003-2881 in III- 20). However, these
 528 ages are older than published ages (10) for Sector III strata III-17 (42.3±2.7 ka) and III-20
 529 (41.7±2.9 ka). Insufficient information is available for the published dataset to allow a complete
 530 comparison, but some useful observations may be made.

531

532 Firstly, the directly comparable datasets for the III-17 and III-20 ages were produced using the
533 CAM (10) and FMM (this study). Since our analysis implies post-depositional incorporation of
534 younger grains into all Sector III samples, the CAM will yield lower D_b values and therefore
535 younger ages than the FMM in the absence of complicating factors. For the present dataset,
536 the CAM yields D_b values $16\pm 4\%$ lower than the FMM, and the discrepancy between the
537 published equivalent doses and those presented here for III-17 and III-20 is consistent with
538 this value. Steele et al. (1) justify the use of the CAM for their III-17 and III-20 samples on the
539 grounds that the observed overdispersion (28 and 36% for their samples) is best explained as
540 the result of inhomogeneous (beta) dose rates at the single-grain level (56). This inference is
541 defensible, and if correct it justifies the use of the CAM. However, use of the CAM on datasets
542 with relatively high ($\sim 20\text{-}25\%$) overdispersion is unconventional and we regard our approach
543 as more appropriate, particularly since micromorphological investigation of these sediments
544 implies some degree of bioturbation.

545

546 Secondly, the published environmental dose rates (2.05 ± 0.10 Gy/ka for III-17 and 2.73 ± 0.15
547 Gy/ka for Layer 20) are higher than those presented here, which would result in a younger
548 calculated age for a given D_b . Inter-sample variation in dose rates is possible, even over short
549 distances within a single archaeological layer. The published sediment water contents and
550 cosmic dose rates are consistent with those presented here. Calculation of the beta and
551 gamma contributions for the published samples suggests that both are partly responsible for
552 the discrepancy with the values in this study. It is possible that both sets of dose rates are
553 accurate, and no grounds exist for dismissing either as erroneous. Because the same
554 techniques were used to calculate dose rates for both the K-feldspar and quartz samples, and
555 the former are in good agreement with independent $^{230}\text{Th}/\text{U}$ burial dating of ostrich eggshell,
556 we regard the values presented in this study as reliable.

557

558 Based on the above reasoning, we believe that the quartz luminescence ages presented
559 above (Table S6) represent the most reliable age estimates for Sector III. Our revised
560 chronology for these units, which contain a Howiesons Poort assemblage, is consistent with
561 the published (57) start ($62.2\text{-}71.1$ ka, 95% CI) and end ($54.5\text{-}62.0$ ka, 95% CI) ages for this
562 technocomplex (their preferred "Estimate B"). Our chronology is also consistent with the longer
563 Howiesons Poort chronology obtained at Diepkloof Rock Shelter (12). Consequently, our
564 revised chronology for Sector III confirms that the Howiesons Poort assemblage at VR003 is
565 contemporaneous with similar material elsewhere in southern Africa.

566

567

568 **U-series Dating of Ostrich Eggshell**

569 **²³⁰Th/U burial dating.** Ostrich eggshells (OES) consist of ~2 mm-thick, low-Mg calcite
570 containing 1-3 wt.% organics and are suitable for ²³⁰Th/U dating, a technique capable of
571 producing accurate, precise ages (~0.1%, 2σ) with a useful limit of >500 ka. Similar to other
572 biominerals of higher animals, modern OES contain extremely low concentrations of primary
573 U (c. 1 ppb or less); accordingly, most U in ancient OES is secondary. Until recently U-series
574 dating of eggshells has been carried out without consideration of the effects of prolonged
575 secondary uptake of U. In contrast, “²³⁰Th/U burial dating” of OES, which we employ herein,
576 explicitly accounts for U uptake by OES from soil water after burial. In a previous study, we
577 documented U uptake patterns in archaeological OES, showed that the effects of prolonged
578 U uptake could be mitigated by applying a simple diffusion model to ages measured on OES
579 subsamples, and demonstrated that resulting model ages termed ²³⁰Th/U burial ages were
580 concordant with ¹⁴C ages measured on splits of latest Pleistocene to Holocene OES (58).
581 Further work has shown that ²³⁰Th/U burial dating can be successfully used to date
582 Pleistocene archaeological sites >100 ka, i.e., well beyond the ~50 ka ¹⁴C limit (59).

583

584 **Laser ablation.** U concentrations of archaeological OES, when profiled normal to their
585 surface via laser ablation, exhibit characteristic asymmetric patterns controlled by the
586 layered crystalline structure of OES (58). U profiles may therefore be used to identify OES
587 suitable for ²³⁰Th/U burial dating and to select optimal locations of subsamples for U-series
588 analysis. OES fragments from VR003 exhibit such U profiles (Figures S11-S13). Beginning
589 at the outer surface, U typically falls rapidly in the first hundred microns or so, defines a flat
590 or gently sloping plateau in the center of the eggshell, falls rapidly to a minimum value, and
591 then rises rapidly with scattered values near the inner surface of the OES. Such a pattern
592 indicates that U concentrations across most of the eggshell, from the outer surface to the U
593 minimum, are controlled by U uptake at the outer surface. These patterns are associated
594 with OES that yield ²³⁰Th/U burial ages concordant with ¹⁴C ages on splits of the same
595 eggshell (58).

596

597 ²³²Th/U profiles of VR003 OES were also carried out via laser ablation (see Figures S11-S13
598 as above). These data identify OES calcite with high common Th (²³²Th), an indicator of
599 associated initial ²³⁰Th, which can degrade the accuracy and precision of ²³⁰Th/U ages. ²³²Th/U
600 ratios generally decrease away from OES surfaces where eggshell calcite may be visibly
601 contaminated by detritus from host sediment (58). The OES from VR003 follow this pattern,
602 with ²³²Th/U ratios of c. 0.1 near their outer surfaces, while further inward rather pure OES
603 calcite with much lower ²³²Th/U ratios occurs.

604

605 Combining information from U and $^{232}\text{Th}/\text{U}$ profiles, the most suitable calcite for U-series dating
606 can be identified. It occurs in the central part of the OES where the crystalline structure
607 consists of radially-oriented, macroscopic columnar calcite crystal bundles of the palisade
608 layer. There, relatively high U and low $^{232}\text{Th}/\text{U}$ ratios coincide. For example, in sample VR003-
609 9085, mean [U] in the palisade layer ranges from ~ 62 to 16 ppb (median = 42.7 ppb); in
610 sample VR003-6612, mean [U] ranges from ~34 to 19 ppb in the palisade layer (median =
611 25.0 ppb); and in sample VR003-9300, [U] ranges between ~ 57 and 32 ppb in the palisade
612 layer (median = 56.2 ppb) (Figure S13; Table S5). In the palisade layer of all three VR003
613 samples, favorable $^{232}\text{Th}/\text{U}$ ratios of c. 0.01 or lower are observed, providing highly suitable
614 material for U-series dating.

615

616 **Table S8.** All isotope ratios are activity ratios. Uncertainties are 2 standard deviations. Uncorrected ages are calculated from measured ratios. Ages were
 617 corrected for U and Th from detritus using $(^{232}\text{Th}/^{238}\text{U}) = 1.21 \pm 0.60$, $(^{230}\text{Th}/^{238}\text{U}) = 1.0 \pm 0.1$, and $(^{234}\text{U}/^{238}\text{U}) = 1.0 \pm 0.1$. Decay constants are those of (60) for
 618 ^{238}U and (61) for ^{230}Th and ^{234}U . Initial $(^{234}\text{U}/^{238}\text{U})$ is back-calculated from the measured ratio and the corrected age.

Sample Name	Sample wt (mg)	U (ppb)	^{232}Th (ppb)	$(^{230}\text{Th}/^{232}\text{Th})$	$(^{232}\text{Th}/^{238}\text{U})$	$\pm (2\sigma, \%)$	$(^{230}\text{Th}/^{238}\text{U})$	$\pm (2\sigma, \%)$	$(^{234}\text{U}/^{238}\text{U})$	$\pm (2\sigma, \%)$	Initial $(^{234}\text{U}/^{238}\text{U})$	$\pm (2\sigma, \text{ab.})$	Uncorrected age		Corrected age		Burial age or minimum age	
													ka	$\pm (2\sigma), \text{ka}$	ka	$\pm (2\sigma), \text{ka}$	ka	$\pm (2\sigma), \text{ka}$
VR003-6612 inner	120.16	15.641	0.2925	136.9	0.0056	1.17	0.8305 0	1.76	1.6094	0.60	1.753	0.011	75.3	1.9	75.0	1.9	74.5	1.4
VR003-6612 outer	102.47	19.800	0.3661	138.0	0.0056	0.83	0.8269 0	1.33	1.6157	1.26	1.759	0.022	74.4	1.9	74.1	1.9		
VR003-9300 inner	102.65	49.731	0.8685	157.6	0.0055	0.56	0.8962 0	0.86	1.6271	0.49	1.7904	0.0090	82.3	1.2	82.0	1.2	88.3	3.2
VR003-9300 outer	95.83	49.836	0.4700	300.7	0.0029	0.87	0.9240 4	1.51	1.6245	0.50	1.7958	0.0099	86.0	2.0	85.9	2.0		
VR003-9085-inner	169.08	36.974	0.4197	264.6	0.0034	0.35	0.9775 4	0.50	1.6488	0.48	1.8389	0.0087	91.2	1.0	91.0	1.0	90.7	0.7
VR003-9085-outer	176.02	52.418	0.7833	199.6	0.0047	0.40	0.9708 9	0.64	1.6465	0.44	1.8342	0.0081	90.6	1.0	90.3	1.1		

619

620

621 **²³⁰Th/U ages of OES.** Three fragments of OES from layer I-09 were dated. U-series analytical
622 data and ages are given in Table S8, above. Measured U concentrations of OES calcite range
623 from ~15 to 50 ppb, ²³²Th/²³⁸U ratios are all <0.006, and corrections for initial ²³⁰Th from detritus
624 are small (median = 0.25 ka), indicating that the samples are geochemically suitable for
625 precise U-series dating. For OES fragment VR003-9300, we obtained an outer-shell age of
626 85.9 ±2.0 ka (errors are 2 σ) and an inner-shell age of 82.0 ±1.2 ka, consistent with prolonged
627 uptake of U originating from the outer surface of the eggshell. In such cases, we apply a simple
628 1-D diffusive uptake model to determine the time when the OES fragment was first exposed
629 to U in soil pore water. To do so, we plot the measured ages versus their distances from the
630 OES outer surface, normalized to the distance measured from the outer surface to the
631 minimum [U] observed in the laser ablation profile, which defines the limit of U derived by
632 uptake at the outer surface. Plotting ages of subsamples versus the square of their normalized
633 distance from the outer surface causes the expected relationship between age and distance
634 to become linear (58, 62). Accordingly, a linear extrapolation of the measured age-distance
635 relation to the outer OES surface, where U uptake was initiated, provides an estimate for the
636 age of initial U uptake, which we term the ²³⁰Th/U burial age of the sample. Figure S13 shows
637 these relationships for OES fragment VR003-9300, leading to a ²³⁰Th/U burial age of 88.3 ±3.2
638 ka, which we interpret as the best estimate for the depositional age of this OES.

639

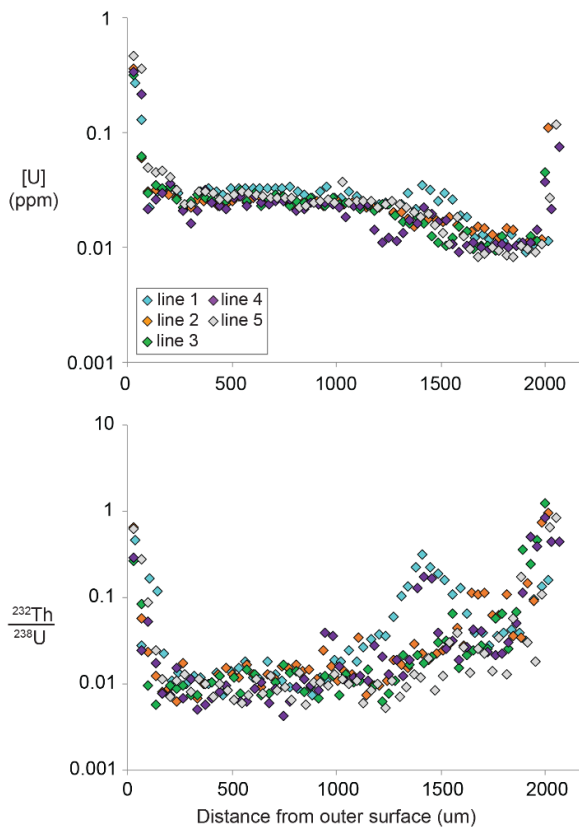
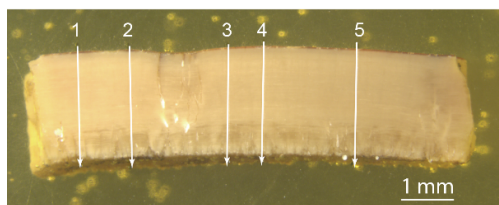
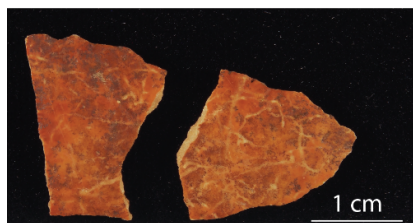
640 Subsamples from two other OES fragments, VR003-9085 and VR003-6612, yield measured
641 ages that are within analytical errors; i.e., 91.0 ±1.0 and 90.3 ±1.1 ka for VR003-9085 and
642 75.0 ±1.9 and 74.1 ±1.9 ka for VR003-6612, indicating relatively rapid U uptake (Figure S14).
643 In such cases, we interpret the weighted mean of the subsample ages as the best estimate of
644 the depositional age of the OES; i.e., 90.7 ±0.7 and 74.5 ±1.4 ka for VR003-9085 and VR003-
645 6612, respectively. The different U uptake histories inferred for the OES fragments studied
646 herein may result from distinct conditions in their host sediments including the availability and
647 U concentrations of soil pore waters in contact with each of the OES fragments.

648

649 As discussed in the text, we interpret the age of OES VR003-6612 as a minimum age and
650 infer an age for stratum I-09 of 90.2 ±3.2 ka (2σ error), equal to the weighted mean ages of
651 OES VR003-9300 and VR003-9085.

652

VR003-6612



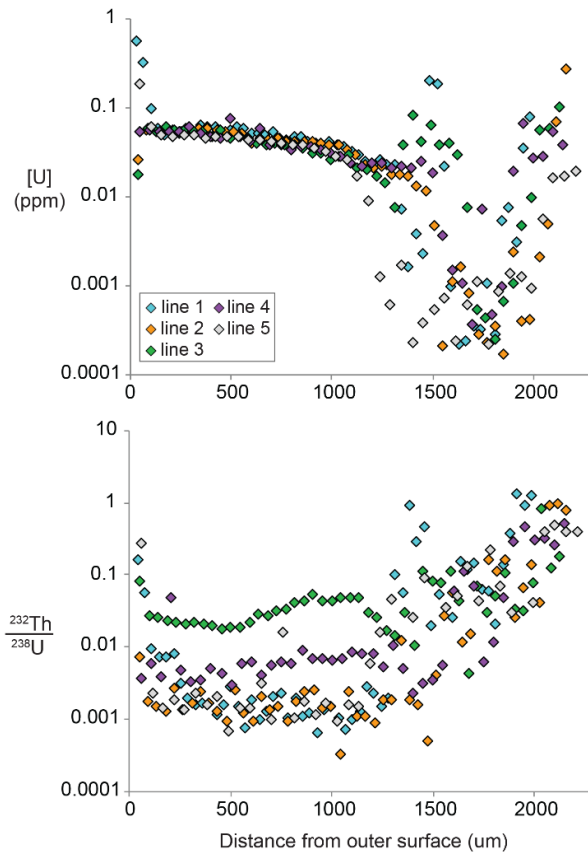
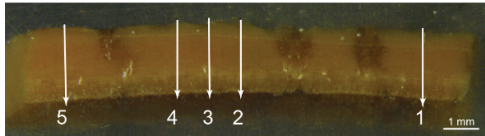
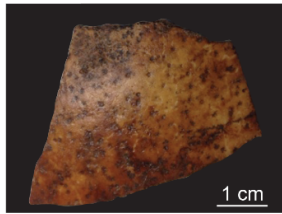
653

654 **Figure S11.** OES VR003-6612. Photo of analyzed OES fragment (upper left); photomicrograph of
655 laser ablation mount showing laser ablation tracks (lower left); and plots of laser ablation results
656 showing [U] and $^{232}\text{Th}/\text{U}$ versus distance from outer surface of OES.

657

658

VR003-9085

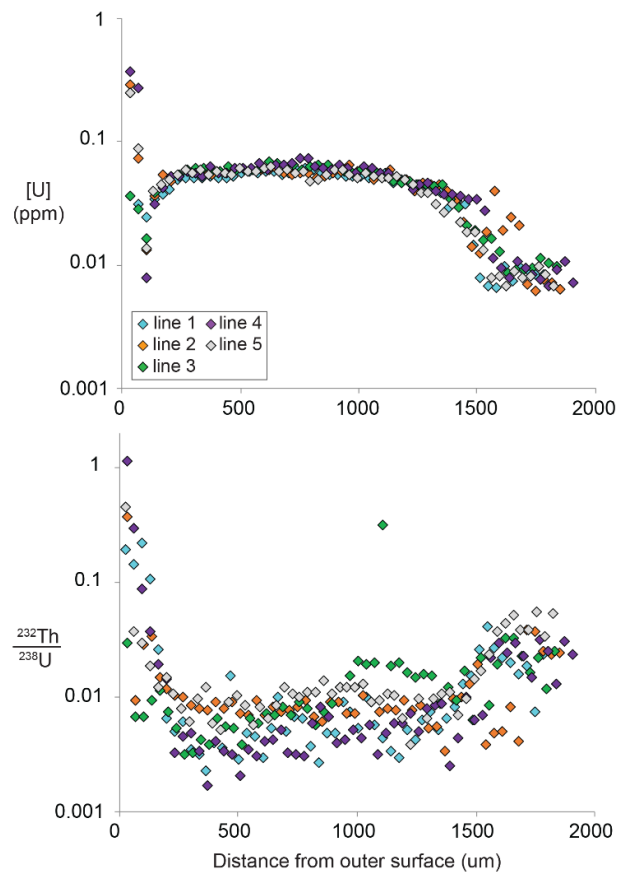
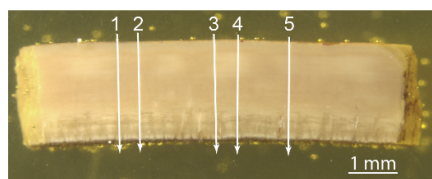
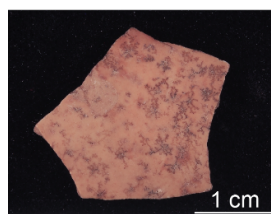


659

660 **Figure S12.** OES VR003-9085. Photo of analyzed OES fragment (upper left); photomicrograph of
661 laser ablation mount showing laser ablation tracks (lower left); and plots of laser ablation results
662 showing [U] and $^{232}\text{Th}/^{238}\text{U}$ versus distance from outer surface of OES.

663

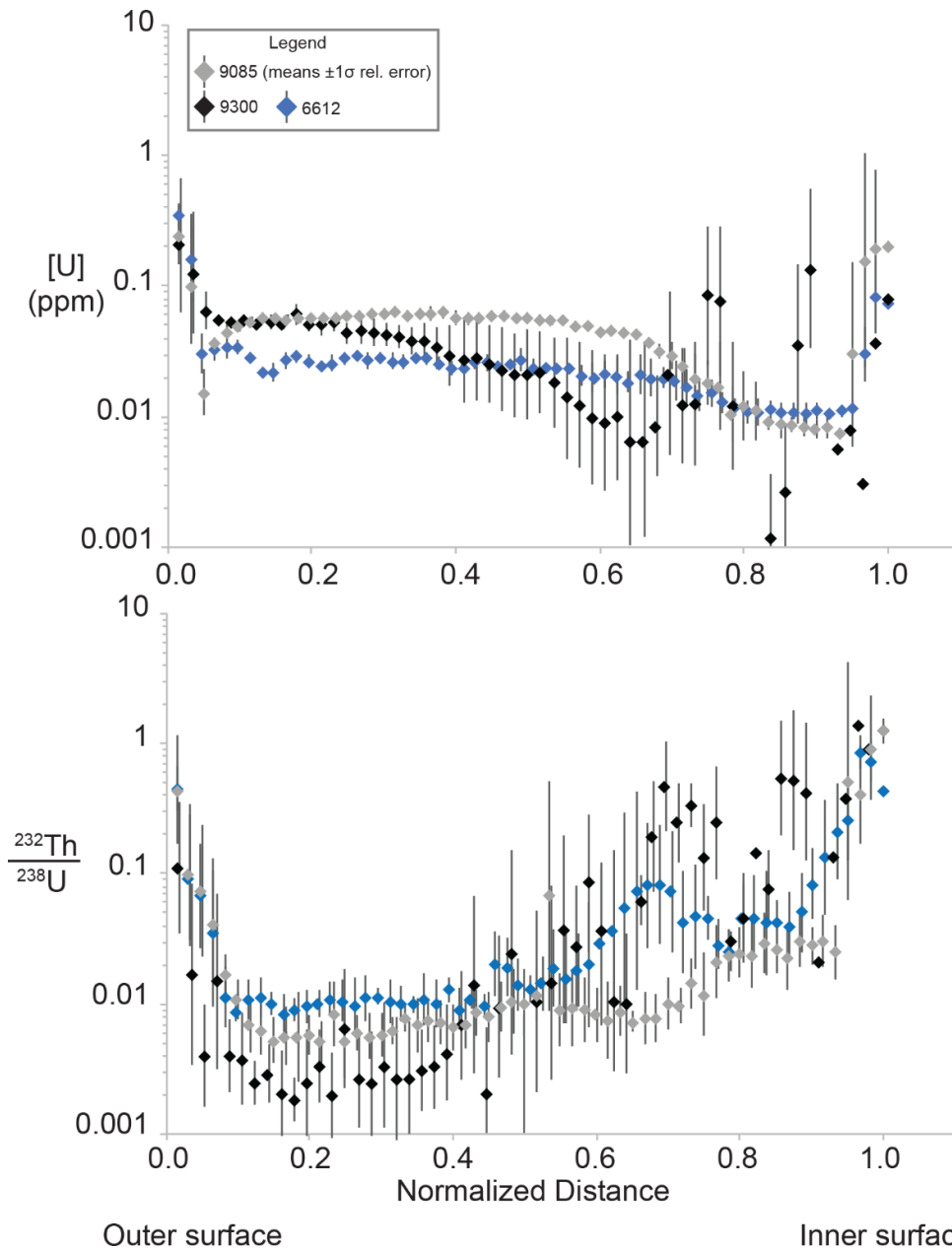
VR003-9300



664

665 **Figure S13.** OES VR003-9300. Photo of analyzed OES fragment (upper left); photomicrograph of
666 laser ablation mount showing laser ablation tracks (lower left); and plots of laser ablation results
667 showing [U] and $^{232}\text{Th}/^{238}\text{U}$ versus distance from outer surface of OES.

668



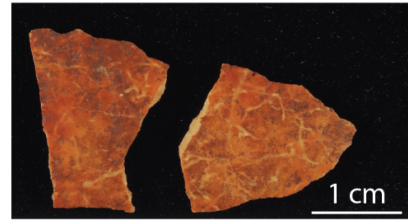
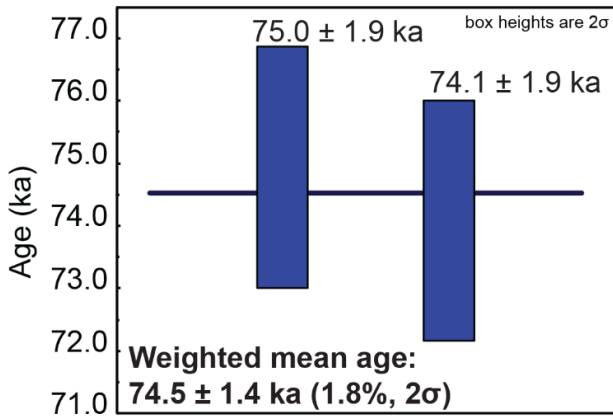
669

670 **Figure S14.** Plots comparing laser ablation results for the dated OES fragments. Points show the
 671 mean [U] or $^{232}\text{Th}/\text{U}$ at each position, computed by averaging values measured along five parallel
 672 laser ablation tracks across each OES. Mean [U] and $^{232}\text{Th}/\text{U}$ values are plotted versus distance from
 673 OES outer surfaces; vertical lines on points show 1σ errors.

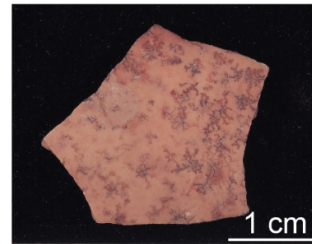
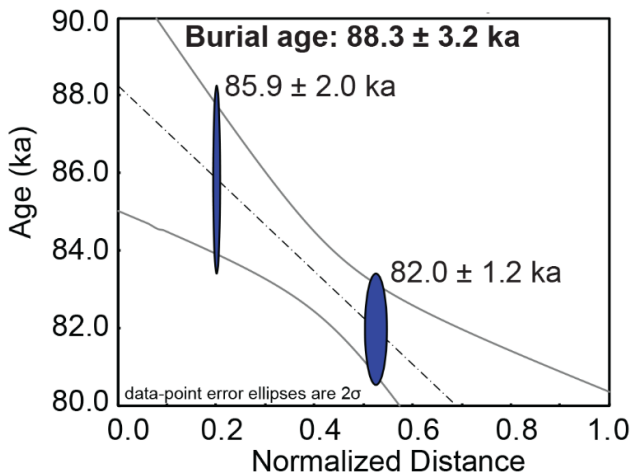
674

675

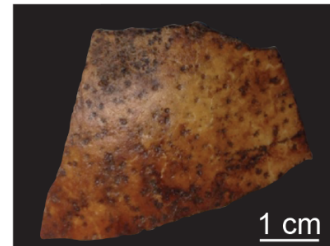
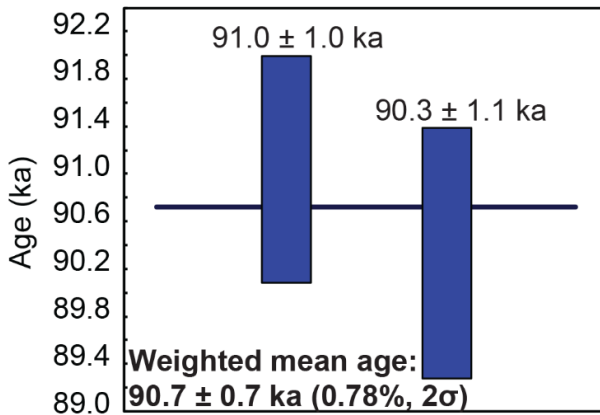
VR003-6612



VR003-9300



VR003-9085

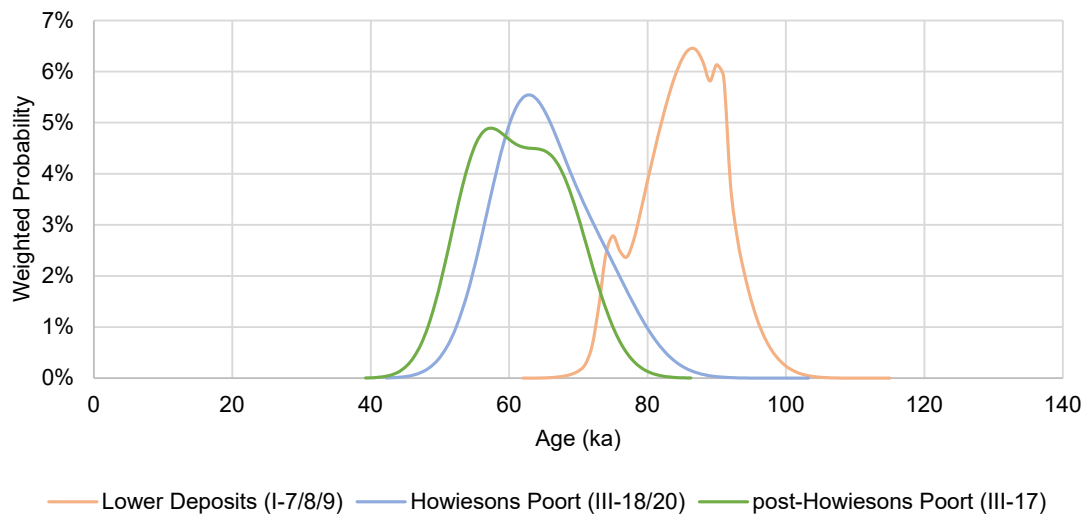


676

677 **Figure S15.** Photos of dated OES fragments (right) and plots of measured U-series ages (left). OES
678 fragment VR003-6612 yields concordant U-series ages for two samples that define a weighted mean
679 age; OES fragment VR003-9300 yields distinct U-series ages for two subsamples that define a
680 $^{230}\text{Th}/\text{U}$ burial age; and VR003-9085 yields concordant U-series ages for two samples that define a
681 weighted mean age.

682 **Establishing age estimates for depositional units**

683 To establish age estimates for the cultural/stratigraphic units identified at VR003, the OSL
684 and ostrich eggshell U/Th ages were combined in weighted probability density functions
685 (pdf_{age}) to define age estimates that reflect the ages and errors associated with each sample.
686 These, with weighted optima and one sigma errors, are shown in Figure S16 below. Age
687 ranges for the units based on optimum values and one sigma errors from these results are:
688 Lower Deposits = 86 ± 6 ; Howiesons Poort = $63 \pm 8 / -6$; post-Howiesons Poort = $57 \pm 12 / -4$.
689 Strata I-07, I-06 and I-05 were not directly dated but they are constrained stratigraphically by
690 adjacent dated layers, and are thus estimated to date to between ~79-71 ka.



691

692 **Figure S16.** Probability density functions defining estimated ages of cultural/stratigraphic units
693 identified at VR003 based on optically stimulated luminescence and ostrich eggshell U/Th ages
694 (Tables S6, S7 & S8).

695

696

697 **Archaeological data**

698 **Phytolith analysis**

699 Phytoliths at archaeological sites will accumulate as a result of natural processes and human
700 transport. The Main Area at VR003 is open to sunlight and naturally vegetated, though we
701 cannot preclude an anthropogenic signal in the phytolith assemblages. We thus focussed
702 our analysis on markers of rainfall seasonality (C₃:C₄ grasses), and the related prevalence of
703 fynbos taxa such as Restionaceae, though recognising particularly in the latter case that
704 humans may have selectively introduced such elements for purposes such as lighting fires
705 and/or construction of bedding.

706

707 **Phytolith classifications and definitions.** Phytolith counts were divided broadly into
708 graminoid and non-graminoid groups, with classification based on the revised nomenclature
709 (63) as well as previous studies (64, 65). Graminoid groups include morphotypes
710 characteristic of Poaceae (grasses), Cyperaceae (sedges), and Restionaceae (Cape reeds)
711 families. Restionaceae (or, restios) includes reniform, paddle-like, and various spheroidal
712 morphotypes. Restios are endemic to southern Africa and are characteristic of the fynbos
713 vegetation of the winter rainfall zone of the southwestern Cape (66, 67). Poaceae includes
714 short cells distinct to various grass subfamilies, such as the C₄ Chloridoid (short saddle) and
715 Panicoid grasses (wide bilobates, crosses), as well as various C₃ subfamilies. Papillates
716 were present, although these could be attributed either to Cyperaceae or to Proteaceae
717 shrubs (68). Other non-specific graminoid morphotypes were also present, such as blocky
718 and elongate, but they cannot be attributed to a particular group. Non-graminoid phytoliths
719 representative of woody and shrubby vegetation were also present in relatively high
720 concentrations (spheroidal, tracheary, among others). Spheroidal phytoliths from both
721 Restionaceae and non-graminoids were counted together due to their considerable
722 morphological similarity. The combination of these two groups is frequently used in contrast
723 with grass phytoliths as an indicator of fynbos vegetation (64, 65).

724

725 *Classification of short cell phytoliths.* The classification of Poaceae short cell phytoliths in this
726 study follows closely that of (69), which is modified from (64, 70). This classification is
727 aligned with the recent ICPN 2.0 nomenclature (63), as well as recent literature (65, 71).
728 Short cells in this study have been identified by morphology and classified by taxonomic
729 (Chloridoids, Panicoids) and bioclimatic (C₃ and C₄) groups (Figure S17).

730

731 **Phytolith data.** The total collected phytolith count and classification for all samples is
732 presented here as Table S9. Results are given as a standardized concentration per gram of

733 sediment. This is followed by a breakdown of the assemblage by ecologically significant
 734 taxonomic and bioclimatic groups, particularly Poaceae subfamilies as well as the
 735 Restionaceae and woody morphotypes in Table S10.

736

737 **Table S9.** Total phytolith concentration (#/gram), sample depths, archaeological unit attribution and
 738 morphotype classifications.

Morphotype	I-09 180-185 cm	I-08b 155-160 cm	I-08a 125-130 cm	I-07 100-105 cm	I-05/06 75-80 cm	I-04b 50-55 cm	I-04a 40-42 cm	I-03/04 30-32 cm	I-03 20-22 cm
Rondel	22.4	13.6	21.8	7.4	7.6	14.3	9.8	27.1	12.6
Crenate	16.8	16.6	9.8	1.6	3.5	0.6	0	2.1	0
Trapezoid	76	99.5	55.7	20.5	10.1	8.6	5.7	18.1	6.8
Polylobate	0	0	1.1	0	0	0	0	0	0
Plateau saddle	1.1	3	1.1	0	0.5	0	0.6	0.7	0.5
Round saddle	1.1	0	0	0	1	0.6	0	0	0
Flat bilobate	5.6	1.5	6.6	1.1	0	0.6	0	0	0
Trapezoidal bilobate	5.6	7.5	8.7	0	1.5	0	0.6	0	0
Cross	0	1.5	0	0	0	0	0	0	0
Short saddle	14.5	28.7	21.8	1.1	1.5	1.7	1.7	2.8	1
Wide bilobate	2.2	0	0	0	0	0.6	0	0	0
Narrow bilobate	1.1	0	0	0	0	0	0	0	0
Tower	11.2	6	9.8	1.1	0	0	0.6	1.4	1
Total short cells	157.6	177.9	136.4	32.8	25.7	27	19	52.2	21.9
Flabellate bulliforms	0	1.5	2.2	0	0	0	0	0	0
Blocky	29.1	70.9	19.7	31.1	19.7	6.3	8.6	27.1	15
Elongate entire	99.5	84.5	99.4	15.8	10.6	12.6	5.2	24.3	6.8
Elongate sinuate	2.2	12.1	12	1.6	1	0	0	0	0
Elongate dentate	2.2	4.5	4.4	0.5	0	0	0	0	0
Acute bulbosus	6.7	12.1	7.6	0	4	0	1.1	2.8	0
Other grasses	13.4	18.1	19.7	7.4	2	6.3	3.4	16.7	9.2
Papillates	4.5	15.1	7.6	3.2	3	2.9	5.2	9.7	4.8
Spheroidal	14.5	21.1	15.3	9.5	17.1	9.7	7.5	36.2	7.7
Reniform	4.5	4.5	6.6	0.5	1	0.6	0	1.4	0.5
Paddle-shape	2.2	3	3.3	1.6	1.5	1.1	0	0.7	0
Tracheary	1.1	3	0	0	4.5	0.6	2.9	22.2	5.3
Sheet	0	0	0	0	0	0	0	4.2	0.5
Other non- graminae	0	0	0	0	0	0	4	0	0
Total phytoliths	337.5	428.3	334.2	104	90.1	67.1	56.9	197.5	71.7

739

740 **Table S10.** Phytolith indicator ratios and proportions from ecologically significant taxonomic and
 741 bioclimatic groups.

	I-09 180-185 cm	I-08b 155-160 cm	I-08a 125-130 cm	I-07 100-105 cm	I-05/06 75-80 cm	I-04b 50-55 cm	I-04a 40-42 cm	I-03/04 30-32 cm	I-03 20-22 cm
Total phytoliths	337.5	428.3	334.2	104	90.1	67.1	56.9	197.5	71.7
Total short cells	157.6	177.9	136.4	32.8	25.7	27	19	52.2	21.9
Grass %	92.1%	89.1%	90.2%	85.8%	69.9%	77.8%	65.6%	62.3%	73.8%
C3 grass %	38.1%	33.1%	31.4%	29.4%	26.9%	36.8%	29.3%	24.3%	27.8%
C4 grass %	5.3%	7.1%	6.5%	1.1%	1.7%	3.4%	3.0%	1.4%	1.4%
Restio+woody %	6.3%	6.7%	7.5%	11.2%	21.8%	17.0%	13.2%	19.4%	11.4%
C4:C3 grasses	13.84	21.31	20.80	3.59	6.20	9.31	10.18	5.83	5.03
Restio+woody:Poa ceae	0.13	0.16	0.18	0.35	0.76	0.42	0.39	0.73	0.37

742

743

744
745
746
747
748
749
750
751
752
753
754
755
756
757
758
759
760
761
762
763
764
765
766
767

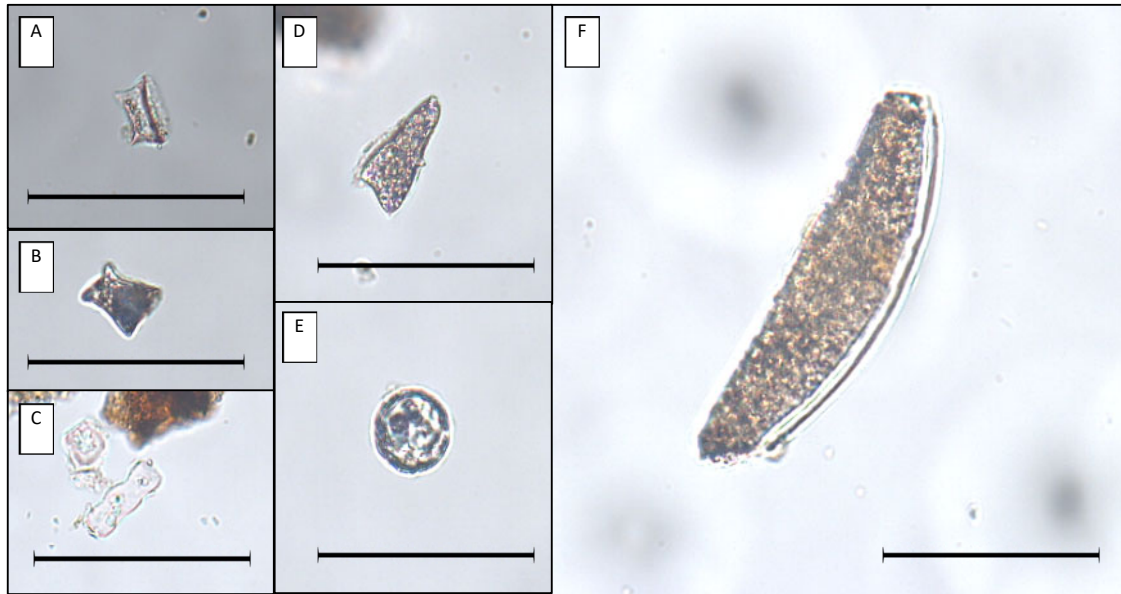
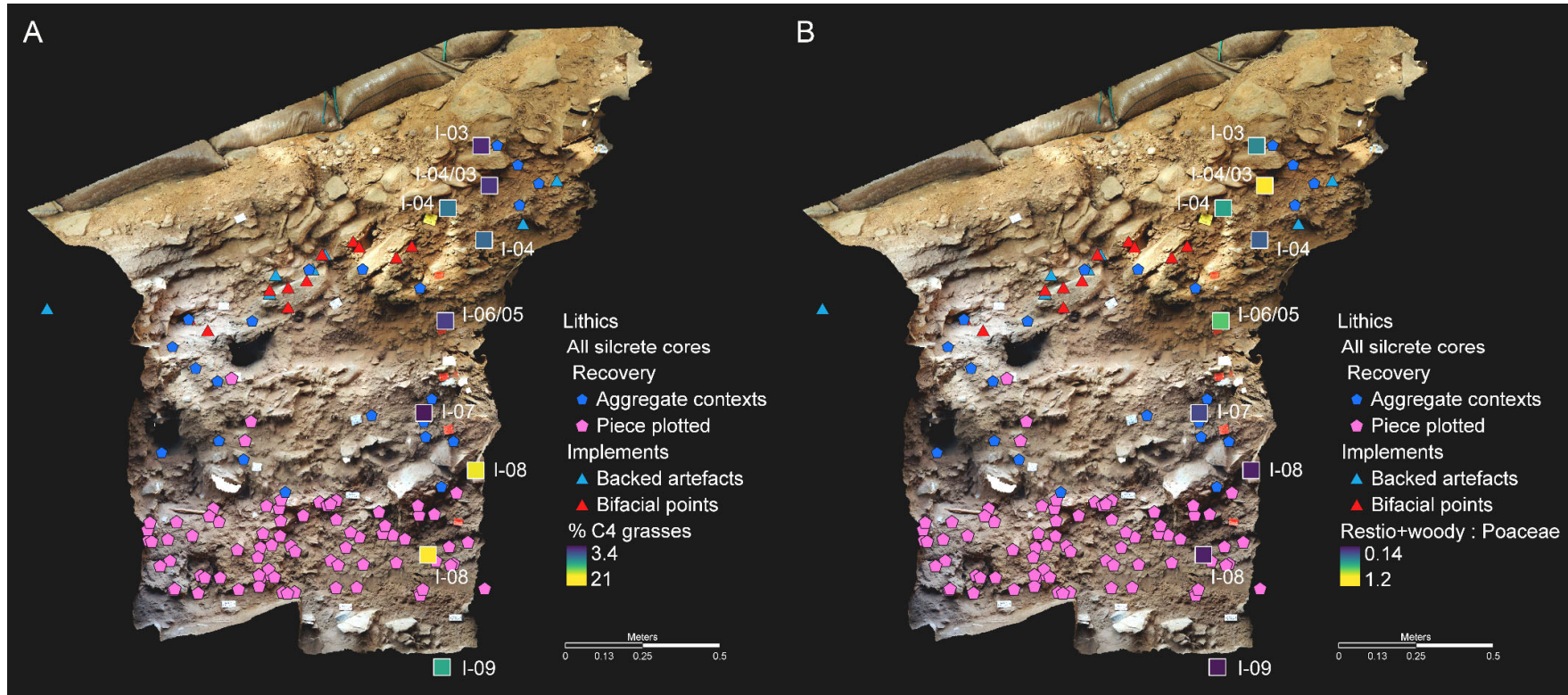


Figure S17. Selected phytolith morphotypes at 400x magnification. All bars 50 μm long. **(A & B)**, short saddles (Poaceae); **(C)**, crenate (Poaceae); **(D)**, paddle-like (Restionaceae); **(E)**, spheroid (Woody non-graminoid); **(F)**, boomerang (Restionaceae).

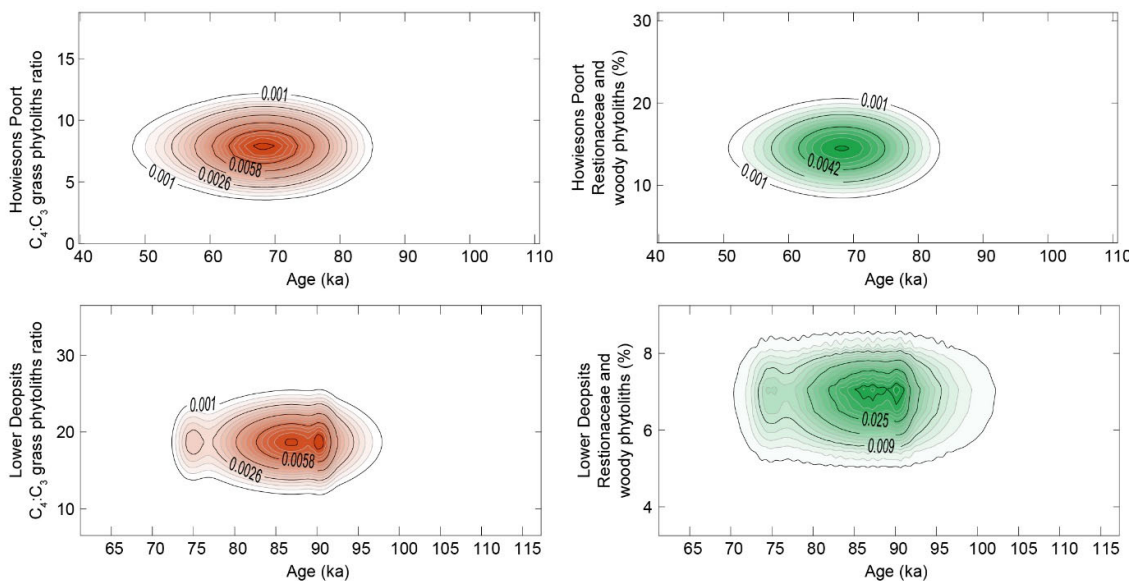


769
 770
 771
 772
 773

Figure S18. East section of VR003 showing sampling locations for phytoliths relative to key artefacts markers for the Lower Deposits, Still Bay and Howiesons Poort, and **(A)** % C₄ among grasses, and **(B)** the ratios of Restionaceae and woody taxa to grasses.

774 **Establishing an age-depth relationship for the phytolith data.** While the phytolith
 775 samples are assumed to respect a stratigraphic order consistent with progressive
 776 accumulation of sediments, the scatter of the OSL and ostrich eggshell U/Th ages does not
 777 enable modelling of a robust age-depth relationship for each sample. As such, to
 778 chronologically constrain the phytolith data, samples from the dated layers were compiled
 779 and mean values with standard deviations were calculated for each layer. This was done for
 780 the two primary metrics considered in this paper: C₄:C₃ grass ratio and the percentage of
 781 Restionaceae and woody phytoliths that have been associated by (60) and (61) with fynbos
 782 vegetation.

783 To define and depict aggregate phytolith sample values for the archaeological units
 784 considered, the sample values for each unit were combined to establish probability density
 785 functions for each unit (using the standard deviation of the sample values as the error)
 786 (pdf_{phyto}). Pdf_{age} (defined above) and pdf_{phyto} for each layer were multiplied to create the
 787 uncertainty spaces used in Main Text Figure 3 (Figure S19).



788 **Figure S19.** Uncertainty spaces defined by chronological and phytolith data for the Lower deposits
 789 and Howiesons Poort units of the VR003 sequence.

790

791 **Evaluation of significant bioclimatic and taxonomic groups and community**
 792 **composition in a regional context.** In this study we employ phytoliths to assess the impact
 793 of putative changes in rainfall seasonality and oceanic and atmospheric circulation dynamics
 794 that are thought to have occurred across the MIS 5/4 transition (72, 73). These changes
 795 include a general depression of regional temperatures, an equatorward displacement of the
 796 westerly storm track (bringing more winter rain to the southwestern Cape) (72-74) and an

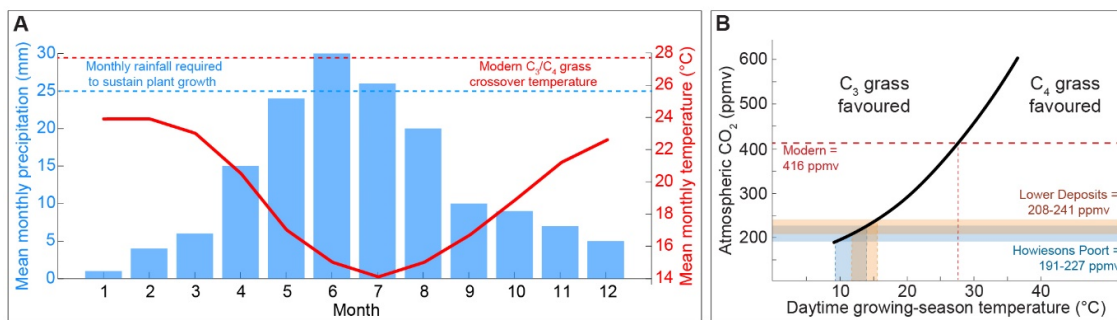
797 intensification of the Southeast Atlantic Anticyclone (73, 75, 76), which would have restricted
798 the incursion of summer moisture-bearing systems associated with tropical easterly flow (77-
799 79).

800

801 In southern Africa, phytoliths have proven to be valuable for inferring changes in rainfall
802 seasonality and vegetation composition (64, 65, 69). Two primary metrics are presented
803 here as ecologically significant indicators of change: the ratio of C₄ to C₃ grasses, and the
804 percentage of Restionaceae and woody phytoliths.

805

806 The differing physiologies of C₄ and C₃ afford distinct competitive advantages as a function
807 of prevailing climates and atmospheric CO₂ concentrations ($p\text{CO}_2$), with C₄ (C₃) grasses
808 being favoured under warmer (cooler) conditions (80-83). With decreasing $p\text{CO}_2$, C₄ grasses
809 gain a competitive advantage over C₃ grasses (81, 82). Under modern annual average
810 atmospheric CO₂ concentrations of 416 ppm (84), the crossover temperature is calculated to
811 be ~27.7°C for the warmest month with sufficient rainfall to sustain plant growth (following
812 81, 82; Figure S19). At the VR003 site, sufficient precipitation is received only in the austral
813 winter months, when temperatures are generally <16°C (Figure S20; (85)), explaining the
814 dominance of C₃ grasses in the region, both today (86) and in the VR003 sequence (Table
815 S9, S10). With no change in rainfall seasonality or amount, regional winter temperatures
816 would need to rise by at least 11.7°C for C₄ grasses to become favoured over C₃ grasses.
817 Under the lower $p\text{CO}_2$ of the 60-90 ka period (~190-240 ppm; (87, 88)), the crossover
818 temperature for C₄ advantage may have dropped to ~9°C or even lower (Figure S19, 81,
819 82). Considered in concert with southern African palaeotemperature reconstructions, which
820 can be used to estimate temperature depressions on the order of 2-4°C for MIS 4/5 (89, 90),
821 it may be predicted that changes in $p\text{CO}_2$ would drive a significant increase C₄ grass
822 phytoliths in the VR003 assemblage, particularly during MIS 4. Results indicate, however,
823 that this was not the case, with C₃ morphotypes dominating the grass phytolith assemblage,
824 particularly during MIS 4, when they reach levels as high as 94.1%. From these results we
825 infer that while $p\text{CO}_2$ may have some influence on the competitive advantage of C₄ over C₃
826 grasses (77, 78), it is primarily climate that drives the variability observed in the VR003
827 sequence.



829

830 **Figure S20. (A)** Modern mean annual precipitation and temperature at the VR003 (data from 80).
 831 Dotted lines indicate the threshold monthly precipitation requirement to sustain plant growth and the
 832 C₃/C₄ crossover temperature under modern atmospheric CO₂ concentrations (77, 78). **(B)** Modelled
 833 competitive advantage afforded C₃ and C₄ grasses as a function of atmospheric CO₂ concentration
 834 and growing season temperature (adapted from 78). Atmospheric CO₂ concentrations are from (84)
 835 for modern values and (82) and (83) for the VR003 units.

836

837 Interpreted thus in terms of climate variability, we consider that the relatively high C₄:C₃ ratio
 838 in samples from the Lower Deposits (92-79 ka) most likely reflect changes in rainfall
 839 seasonality, with an increase in summer rainfall, enabling at a minimum a greater presence
 840 of drought-adapted species of C₄ Chloridoideae (such as *Cladoraphis spinosa*). The
 841 transition from MIS 5 to MIS 4 is marked by a clear decrease in C₄ grass phytoliths, which
 842 we interpret to be an indication of reduced summer rainfall and a more seasonal rainfall
 843 regime. These findings are consistent both with prevailing conceptual models, which invoke
 844 equatorward expansions of the westerly storm track and southern African winter rainfall zone
 845 during periods of increased Antarctic sea-ice extent (72-74, 91) and with evidence indicating
 846 a marked increase in South Atlantic Anticyclone intensity (Main Text Figure 3; as calculated
 847 by (92) using the data of (73, 75, 76, 93), which would have limited the
 848 incursion/development of summer rainfall systems in the region.

849

850 As mentioned, the percentage of Restionaceae and woody phytoliths has - contrasted with
 851 grass phytoliths - been used as an indicator of fynbos vegetation (64, 65), which is
 852 characteristic of the Fynbos Biome that is today primarily restricted to regions south of
 853 VR003 (Main Text Figure 1; (94)). In contrast, phytoliths from the vegetation of the Succulent
 854 Karoo Biome (currently encompassing the VR003 site) are uncommon and/or largely non-
 855 diagnostic, but do contain relatively higher levels of Chloridoideae (C₄) phytoliths compared
 856 with fynbos (69, 95). At VR003, percentages of the Restionaceae and woody phytolith group
 857 more than double across the MIS 5/4 transition (from 6.8% to 16.5%). Considering the
 858 anthropogenic nature of archaeological sediments, and the noted use of Restionaceae for
 859 bedding (96), human agency cannot be discounted as the driver behind this change, but as

860 it coincides with shift towards more C₃ grass presence we consider it more parsimonious
861 that the increase in Restionaceae and woody phytoliths reflects environmental change and a
862 northward expansion of fynbos vegetation.

863

864 In summary, we conclude that variability in the VR003 phytolith record is consistent with data
865 from independent regional records that indicate significant changes to regional climate
866 systems across the MIS 5/4 boundary. Cooler global temperatures, expanded Antarctic sea-
867 ice extent and steeper intrahemispheric temperature gradients would have combined to drive
868 an increase in winter rain at VR003 while concurrently limiting the influence of summer rain
869 systems. The result would have been greater affinities with the Fynbos Biome, and weaker
870 environmental boundaries between VR003 and contemporaneous archaeological sites to the
871 south.

872

873

874 **Fauna**

875 **Vertebrates.** Early explorer records can be an important source for reconstructing historic
876 faunal communities, and Skead has provided the most comprehensive reviews of accounts
877 for south-western Africa (97, 98). However, information specific to the Knersvlakte is rare,
878 and we must look towards descriptions of Namaqualand more generally. This may be
879 suitable, because Namaqualand belongs to the Succulent-Karoo Biome and as such it
880 appears that historically at least the Olifants River created an ecological boundary between
881 this semi-desert of the north and the grassy, Fynbos Biome to the south (97), and VR003 is
882 to the north. Following (97), (99), and (100) in Namaqualand's recent past red hartebeest
883 (*Alcelaphus buselaphus*), gemsbok (*Oryx gazella*), and springbok (*Antidorcas marsupialis*)
884 grazed the coastal plains, while black rhinoceros (*Diceros bicornis*) likely browsed in the
885 scrubrier areas with surface water. Klipspringer (*Oreotragus oreotragus*), grey rhebok
886 (*Pelea capreolus*), and mountain zebra (*Equus zebra*) were found in rockier up-lands,
887 probably alongside hyrax (*Procavia capensis*), which are present on VR003's farm today.
888 Eland (*Taurotragus oryx*) and quagga (which is often considered a sub-species of Plains
889 zebra, *Equus quagga*) were also seen in the region historically, but like many of the other
890 large bodied taxa, eland have been extirpated from the region while quagga are extinct.
891 Steenbok (*Raphicerus campestris*), common duiker (*Sylvicapra grimmia*), Cape porcupines
892 (*Hystrix africaeaustralis*), and ostrich (*Struthio camelus*) continue to be seen throughout the
893 region, as well as small animals such as hare (*Lepus* sp.) and a variety of tortoises: mostly
894 commonly the angulate or South African bowsprit tortoise (*Chersina angulate*), but also
895 speckled padloper (*Homopus signatus*) and tent tortoise (*Psammobates tentorius*). A variety
896 of large carnivores exploited the region, including hyenas (brown [*Hyaena brunnea*] and
897 spotted [*Crocuta crocuta*]), jackals (*Canis mesomelas*), caracals (*Caracal caracal*), leopards
898 (*Panthera pardus*), and even lions (*Panthera leo*), alongside many smaller carnivores. Cape
899 fur seal (*Arctocephalus pusillus*), penguin (*Spheniscus demersus*), and other shore birds
900 would have been found along the coast.

901

902 However, Late Pleistocene faunal communities are often distinct from the historic ones. For
903 example, further south in the Fynbos Biome the elevated abundance of grazers indicates
904 that more grasses must have been present in the Late Pleistocene (101). Locally however,
905 until our project on the Varsche Rivier Farm, no archaeological samples were known, either
906 MSA or LSA, from the Knersvlakte, so no local Late Pleistocene comparisons are possible
907 (102). Late Pleistocene faunal samples have been described from northern Namaqualand,
908 including the MSA deposits from Spitzkloof Rockshelter (103) and the hyena den sample
909 from Boegoeberg 1 (104).

910

911 The Lower Deposit faunal assemblage (Table S11) has a substantial proportion of tortoise
912 remains (n= 352, 67% of total NISP) and counts of distal humeri indicate at least 21
913 individuals present; when carapace and plastron pieces are identifiable to species they are
914 predominately from angulate tortoises; one humerus was not an angulate but the alternative
915 species could not be confidently assigned. Mammals comprise the other major component of
916 the assemblage, primarily bovids of all size classes as well as zebras. Based on
917 identifications of dental remains, among the small bovids, grysbok/steenbok were confirmed,
918 and among the large bovids, eland were identified. While no identifiable dental remains of
919 small-medium and medium-large bovids were preserved in the Lower Deposits, in other Late
920 Pleistocene contexts at VR003, small-medium bovids are represented by springbok
921 (*Antidorcas marsupialis*) and large-medium bovids are represented by alcelaphines
922 (wildebeest and hartebeest; *Alcelaphus* and *Connochaetes*) and the now extinct blue
923 antelope (*Hippotragus leucopheus*). When comparing to the historic data, many of the taxa
924 identified in the Lower Deposits of VR003 were seen in Namaqualand historically. This
925 includes hyraxes, porcupines, honey badgers and the abundant tortoises. A few taxa require
926 further discussion (again, following (97, 99)). Overall, terrestrial species representation
927 suggests a relatively open, arid to semi-arid environment, with both graze and browse
928 available in diverse habitats. More grass would have been available than was present in the
929 region during the late Holocene, including historically. While the phytolith data show variation
930 through the sequence, a comparable signal of change through time is harder to identify in
931 the faunal record; small sample sizes limit detailed comparisons.

932

933 VR003 is close to the boundary where Cape dune mole-rats exist to the south and Namaqua
934 dune mole-rats (*Bathyergus janetta*) exist to the north. Our identification is based on our
935 specimen's larger size, because the Cape species is larger than the Namaqua one;
936 however, Cape dune mole-rat body size varies with precipitation (105), and it may be
937 possible that Namaqua dune mole-rats did, too. In either case, mole-rats indicate flat sandy
938 substrates, which necessary for their burrowing, and they can survive independent of water,
939 obtaining sufficient moisture from the plants that they eat.

940

941 Skead (97) highlights the challenges of trying to determine which small cats were referenced
942 in the historic accounts, and although references specific to wild cats are not known for
943 Namaqualand, they were presumed to be present because of their recent wide geographic
944 range; furthermore, the black-footed cat (*Felis nigripes*) might be possible. We identified the
945 VR003 specimens as wild cat based on their size, because black-footed cats are
946 significantly smaller.

947

948 The Cape zebra was a horse-sized zebra that grazed a broad range of southern eastern and
949 north-eastern Africa during the Pleistocene (106). The Cape zebra disappeared from
950 southern Africa by 12,000 to 9,500 years ago, apparently because grazing opportunities
951 declined with the onset of the Holocene, further indicated by the increase in smaller
952 browsing taxa in Holocene and historic faunas (107-109). In this assemblage, we identified
953 our specimen as Cape zebra instead of quagga based on its large size.

954

955 Eland were present but apparently sparse in Namaqualand historically. They have a wide
956 geographic distribution, because they are mixed-feeders taking advantage of grazing and
957 browsing based on local availability. Importantly, they are not tied to surface water and
958 therefore can take advantage of a wider variety of habitats. Therefore, their presence in the
959 Lower Deposits of VR003 are not surprising, and other sites show that MSA people
960 frequently hunted them (110, 111).

961

962 Finally, based on the specimens preserved, we were unable to distinguish steenbok from
963 grysbok (both small bovids of the genera *Raphicerus*). Steenbok are common in
964 Namaqualand today; they are browsers who prefer open areas with some tall grasses or
965 shrubs for protection. Grysbok were probably also in the area, at least in the southern part
966 adjacent to the mountainous fynbos. They are also a browser, but they prefer denser cover
967 than steenbok. During the Late Pleistocene grysbok appear to have been much more
968 widespread, and therefore we cannot confidently argue that our specimens are more likely to
969 be one species over the other (112). However, in the Richtersveld of northern Namaqualand,
970 steenbok but not grysbok have been identified in the Late Pleistocene deposits of Spitzkloof
971 (103) and Boegoeberg 1 (104), indicating open environments.

972

973 Analysis of bone modifications was limited due to high fragmentation and poor preservation
974 of the assemblage, and signs of hominin butchery and carcass processing may be obscured
975 by some root etching, minor weathering damage, and the more common presence of
976 concretions on many of the specimens. No cutmarks or percussion marks were observed but
977 evidence of green breakage on a small portion (n=7) of bovid long bones could indicate
978 cracking of fresh bone to access marrow. All major taxonomic categories (tortoises, bovids,
979 small mammals/carnivores, birds) show some evidence of burning. No chew-marks, gastric
980 etching, or other evidence of carnivore consumption were observed.

981

982

983 **Table S11.** The faunal remains from the Lower Deposits, I-08 and I-09. The Number of Identified
 984 Specimens (NISP) are presented, along with the Minimum Number of Individuals (MNI). The bovid
 985 species counts are based on dental remains, and those counts are not included in the body-size
 986 categories. When possible to identify more specifically, the Testudinidae are *Chersina angulate*, with
 987 the exception of one humerus which was not. The birds and snakes were not identified to more
 988 specific taxa. Mammalian nomenclature based on (99).

Scientific name	Common name	NISP	MNI
<i>Procavia capensis</i>	rock hyrax (dassie)	1	1
<i>Bathyergus suillus</i>	Cape dune mole-rat	1	1
<i>Hystrix africaeaustralis</i>	Cape porcupine	1	1
<i>Felis silvestris libyca</i>	African wild cat	8	1
<i>Mellivora capensis</i>	honey badger (ratel)	1	1
<i>Equus capensis</i>	Cape zebra	1	1
<i>Taurotragus oryx</i>	eland	5	2
<i>Raphicerus</i> sp(p.)	grysbok/steenbok	4	1
	small bovid(s)	63	1
	small-medium bovid(s)	34	1
	large-medium bovid(s)	32	1
	large bovid(s)	15	1
Aves	birds	3	1
Testudinidae	tortoises	352	21
Serpentes	snakes	3	1
	Total	524	

989

990 **Molluscs.** The West Coast of South Africa is well-known for its important fisheries. The
 991 coast supports a high biomass of animals and plants, due to the near-shore upwellings that
 992 bring cold, nutrient-rich waters to the surface (113). Humans have taken advantage of this
 993 productive coastal ecosystem from today into the deeper past. Along the West Coast, LSA
 994 shell middens are abundant and well-documented from the coastal fynbos region south of
 995 our study area: particularly from Lambert's, Elands, and Saldanha Bays and the Vredenburg
 996 Peninsula (114, 115). In northern Namaqualand, numerous LSA shell middens are
 997 documented along the coastal regions of the Buffels, Swartlinjies, and Spoeg Rivers (116-
 998 119). MSA shell middens are rarer, but a few are documented: Boegoeberg 2 in the far north
 999 and Ysterfontein 1, Hoedjiespunt 1 and 3, and Sea Harvest to the south (114). Sites are
 1000 known from along the coast west of VR003, but few have been well-investigated (120).
 1001 Nearest to VR003 are samples from Brandsebaai, where five LSA and one MSA shell
 1002 middens have been analyzed in detail (121), highlighting that shellfish should have been
 1003 available along the more local coast while VR003 was occupied.

1004

1005 The LSA and MSA shell middens document that coastal occupants consistently exploited
 1006 limpets and mussels from the rocky shoreline. Three limpet species are most common in
 1007 archaeological samples from the West Coast: granite (*Cymbula granatina*), granular
 1008 (*Scutellastra granularis*), and Argenville's (*Scutellastra argenvillei*). Granite limpets live and
 1009 graze on rocks in the upper part of the inter-tidal zone (the Upper Balanoid), often in high
 1010 densities in Namaqualand, making them readily accessible to foragers during low-tide;

1011 granular limpets also live in this zone, often even higher in the inter-tidal than granite limpets
1012 (113, 122). Despite their increased accessibility, granular limpets are often passed over at
1013 first as foragers focus their harvesting on larger granite limpets (121, 123). Argenville's
1014 limpets can also occur at high densities and are the largest of the three, but they occur
1015 lowest in the inter-tidal (122); they are most accessible during spring low tides, which may
1016 have restricted their exploitation in the past despite their large size. Black mussels
1017 (*Choromytilus meridionalis*) are commonly found alongside these three limpets in
1018 archaeological assemblages, although their relative proportions can vary considerably. This
1019 variation may reflect local rocky shore morphology, because limpets prefer sheltered areas
1020 as heavy waves may dislodge them, while mussels, as filter feeders, prefer surfaces
1021 exposed to wave action. Black mussels primarily live in the lower inter-tidal, but will extend
1022 up to the more accessible reaches; storms may dislodge and wash up rafts or mats of
1023 mussels, which humans can be readily harvest, if found fresh. The mollusc sample from the
1024 Lower Deposits of VR003 is consistent with the other archaeological samples noted above
1025 and contains mostly granite limpets (NISP=13), but Argenville's limpet (NISP=3) and
1026 unidentifiable limpet (NISP=4) fragments are also present, along with fragments of black
1027 mussels (NISP=2) (Table S12). The shells are fragmented, but no ochre residues nor
1028 anthropogenic modifications were observed on them.

1029

1030 What is surprising about the VR003 Lower Deposits mollusc sample is that they were
1031 transported at least 44 km from the coast to the site. Ethnographic work with modern
1032 shellfish foragers shows that they rarely transported shellfish meant for consumption more
1033 than 10 km (2 hours walk) from the coast, and usually they stay much closer; the locations of
1034 recent shell middens (when sea levels would have been near what they are today) supports
1035 this (124-127). From the MSA, two exceptions are known: Diepkloof Rock Shelter and
1036 Sibudu Cave. Diepkloof is 14 km from the modern coast. The MSA assemblages span from
1037 the pre-Still Bay through the post-Howiesons Poort, although the molluscs are concentrated
1038 in the upper deposits; granite limpets (1,565.1 g) and black mussels (809.0 g) are most
1039 common, consistent with other shell middens from the West Coast (128). Sibudu also span
1040 from the pre-Still Bay through the post-Howiesons Poort and preserves mostly brown
1041 mussels (*Perna perna*; NISP=296), but also some other molluscs and a few fish remains;
1042 Sibudu is ~15 km from the modern coast of KwaZulu-Natal (129). These two examples may
1043 represent the extreme end of the distribution of variation in transport distances for edible
1044 shellfish or they may represent transportation for other purposes. At least in the younger
1045 MSA deposits, Diepkloof's sample is large enough that it suggests consistent consumption
1046 of shellfish, and therefore may reflect the ease of transportation along the flat landscape of
1047 the Verlorenvlei (128).

1048

1049 More extreme is the evidence for long-distance transportation during the MSA of small
1050 samples of marine shellfish noted from Apollo 11 and Pockenbank Rock Shelter, which are
1051 ~140 km and ~120 km from the modern coast respectively. Apollo 11 preserves two granite
1052 limpet fragments and Pockenbank has provided granite limpet and black mussel fragments
1053 [T. Steele, personal observation] (130, 131). Transportation beyond 10-15 km is more typical
1054 of the LSA, including small samples of shells that were found in the LSA deposits of VR003
1055 and three LSA sites on the same farm (1, 132-134). The reason for the transportation of the
1056 VR003 Lower Deposits marine shells is unclear, and further investigations are needed to
1057 help determine if they may have been transported for use as containers, tools, or other
1058 purposes; however, we have identified no residues or anthropogenic modifications on them.
1059 In the pre-Still Bay deposits of Blombos Cave, a large abalone (*Haliotis midae*) shell was
1060 found that had been used as a container for processing ochre (135). As far as we are aware,
1061 marine shells tools have not yet been documented in the MSA, although they are known
1062 from the Middle Paleolithic (such as in Grotta dei Moscerini, Italy) and from more recent
1063 periods (136). Finally, at the Pinnacle Point 13B and the Contrebandiers Cave (Morocco),
1064 MSA people transported larger shells (helmet or lipped cask shell, *Phalium labiatum*, and
1065 predatory sea snails *Charonia lampas*, respectively) into these coastal sites for unknown
1066 reasons; the taphonomy of the shells indicates that they were collected after the gastropod
1067 inside had died, so they were not first used as a food resource (137). The MSA African
1068 record does show that smaller shells that were often used as ornaments were regularly
1069 transported for 40-50 km (from the modern shore), with one example of 200 km (138),
1070 although the largest assemblages come from near-shore contexts.

1071

1072 **Table S12.** The marine shell remains from I-08 and I-09. The Number of Identified Specimens (NISP)
1073 are presented, along with the Minimum Number of Individuals (MNI); weight in grams and number of
1074 burnt specimens are also included. When MNI counts exceed one, they are based on the apices of
1075 the limpets.

Scientific name	Common name	NISP	MNI	Weight (g)	# Burnt
<i>Choromytilus meridionalis</i>	black mussel	2	1	0.3	1
<i>Cymbula granatina</i>	granite limpet	13	2	45.2	0
<i>Scutellastra argenvillei</i>	Argenville's limpet	3	1	12.7	2
	limpet	4	1	1.5	4
	mollusc	4	1	1.2	1
Total		26			

1076

1077 **Ostrich eggshell (OES).** Fragments of OES recovered from the screens during excavation
1078 were sorted into categories based on colour, representing the temperature of heat exposure
1079 consistent with that described by (139) (Table S13). Counts and weights were recorded, and
1080 all fragments were examined for evidence of anthropomorphic alteration, including beads in
1081 various stages of manufacture, intentional engraving, and any indication of deliberate or

1082 repeated percussive modification (i.e., flaking) (Table S14). Occasionally worked pieces
 1083 were identified during excavation (n=5 as in Table S14). These were individually plotted, and
 1084 then quantified in terms of count, colour, and weight; they are included in Table S13.

1085

1086 OES identified as possibly flaked were examined using a Nikon SMZ 1000 stereomicroscope
 1087 with a magnification range of 8x to 80x. A Nikon D7100 was attached for microphotos that
 1088 captured images at a magnification range of 16x to 160x. Flaking initiations can be seen, for
 1089 example, on fragments VR003-6147, VR003-7833, and VR003-7114, indicating repeated
 1090 application of downward percussive force in a series of precisely-aimed blows (Main Text
 1091 Figure 4). A few samples preserved only simple notches from single blows (e.g., VR003-
 1092 9220, VR003-7693) that could be carnivore perforations (140); in other cases such notches
 1093 appear to reflect either errant blows or early stages of flaking (e.g., VR003-7974, VR003-
 1094 9300, VR003-7340) prior to refinement of the flaking arc. Perforation notches may potentially
 1095 reflect initial stages of flask opening.

1096

1097 **Table S13.** OES divided into categories of heat exposure, including number of fragments
 1098 and total weight in grams (g).

I-08 & I-09	OES < 200°C		OES 200°C - 350°C		OES > 350°C		Total OES	
	n=	Wt (g)	n=	Wt (g)	n=	Wt (g)	n=	Wt (g)
Aggregate samples	2719 17%	1605.4 21%	3479 22%	2692.1 36%	9511 61%	3262.4 43%	15709	7559.9

1099

1100
1101
1102
1103

Table S14. Details of flaked OES fragments recovered from I-08 and I-09. Concave refers to concavities formed by repeated flaking in an arc; notched refers to a concavity formed by a single flaking initiation. Arc radius and circle diameter estimated for concave flaked margins only.

Sample ID	Recovery	Max. dimension (mm)	N initiation	N margins flaked	Initiation from exterior?	Initiation from interior?	Concave (C) and/or notched	C Width (CW)	C Depth (CD)	CD / CW	N width	N depth	Est. radius	Est. diam.
5698	screen	41.3	>3	1	1	0	C	9.3	0.6	15.50			18.32	36.64
6147	plot	24.6	>3	1	1	0	C	14.8	1.8	8.22			16.11	32.22
7833	plot	30	>3	1	1	0	C	18.8	3.1	6.06			15.80	31.60
7114	screen	18.8	>3	1	1	0	C	11.3	1.1	10.27			15.06	30.12
7693	screen	17.6	>3	1	1	0	C	10.6	1	10.60			14.55	29.09
5910	screen	23.7	>3	1	1	0	C	12.6	1.7	7.41			12.52	25.05
8415	plot	30.5	>3	1	1	0	C	13.4	2.1	6.38			11.74	23.48
6307	plot	38.4	>3	1	1	0	C	13.3	2.1	6.33			11.58	23.16
9300	screen	17.9	3	1	1	0	C,N	11.8	1.7	6.94	5.8	1.2	11.09	22.18
7974	screen	29.7	>3	1	1	0	C,N	14.1	2.6	5.42	6.3	2	10.86	21.72
8417	screen	13.1	>3	1	1	0	C	6.4	0.5	12.80			10.49	20.98
8348	plot	27.6	>3	1	1	1	C	11.3	1.8	6.28			9.77	19.53
8100	screen	23	>3	1	1	0	C	8.9	1.1	8.09			9.55	19.10
6060	screen	22	>3	1	1	0	C	8.5	1.1	7.73			8.76	17.52
6199	screen	28.2	>3	1	1	0	C	8.8	1.2	7.33			8.67	17.33
6612	screen	17.7	>3	1	1	0	C	6.7	0.7	9.57			8.37	16.73
9340	screen	17.9	2	1	1	0	C,N	8.4	1.3	6.46	4.5	1.2	7.43	14.87
8344	screen	32.7	1	1	0	0								
5169	screen	22.3	2	2	1	0								
9220	screen	19.2	1	1	1	0	N				5.1	2.9		
7693	screen	18.9	1	1	1	0	N				4.9	1.6		

1104
1105

1106 **Pigments**

1107 Data recorded on all pigments >5 mm from the Lower Deposits include nodule morphology,
1108 weathering, friability, hardness, magnetism, texture, luster, and type of inclusions. It was
1109 noted whether or not each pigment nodule was washed before analysis in case of
1110 ambiguous traces. Macroscopic observations were made using a Nikon SMZ 1000
1111 stereomicroscope with a magnification range of 8x to 80x. A Nikon D7100 was attached for
1112 microphotos, capturing images at magnifications from 16x to 160x. For pigment nodules that
1113 were anthropogenically modified, modification form, proportion, number of facets, and profile
1114 type were recorded. Pigment nodules were tested for streakability on a ceramic plate. If
1115 nodules did not streak or exhibited poor staining power, they were excluded from the final
1116 count. Pigment streak colour was assessed using a Munsell CAPTURE Color Matching Tool,
1117 directly applied to the ceramic plates following device protocols. Munsell colour values were
1118 captured multiple times to ensure accuracy. If multiple values were obtained, the value that
1119 was captured more often was used. Munsell colour values were then converted to the RGB
1120 colour model using the xyY-to-sRGB formula at <https://pteromys.melonisland.net/munsell/>.

1121

1122 The Lower Deposit pigment assemblage comprises 78 pieces (Table S15) featuring
1123 considerable variation in morphology and mineralogy (including pieces rich in hematite,
1124 limonite, and manganese). Nodules masses range from 0.05g to 12.01g with the vast
1125 majority <1g. Pigment nodules have varying morphologies that include irregular chunks
1126 (n=48), rounded lumps (n=16), flakes (n=6), chips (n=6), a tabular piece, and a prismatic
1127 (crayon-like) one (Table S15). Nodules described as chunks exhibit an irregular thick
1128 morphology with sharp edges (Figure S21), while chips and flakes are thin portions derived
1129 from larger nodules. Chips are rounded in outline, while flakes are angular. Nodules exhibit
1130 some weathering with almost all having some amount of sediment adhering to them (n=75)
1131 and many with indications of rounding (n=38). A small number of pigments nodules were
1132 either burned (n=2; Figure S21) or have ash adhering to the surface (n=1). Nodules are
1133 generally well or moderately cemented, though three nodules are friable to the touch. Many
1134 nodule colors are represented in this assemblage including pink, red, purple, black, grey,
1135 greenish brown, yellow, and orange; nodules streak in a wide variety of colors and hues from
1136 dark reds and reddish browns to light reds and pale browns with reddish yellows, strong
1137 browns, and medium reds in between (Figure S21). Three of the specimens appear to be
1138 massive hematite nodules, which generally are substantial, smooth, dark, and glossy in
1139 appearance. While many similar objects such as these did not produce a color when
1140 streaked on a ceramic tile, the three included in this dataset exhibited relatively good
1141 staining power in colors such as very pale brown and yellowish red. The majority of the

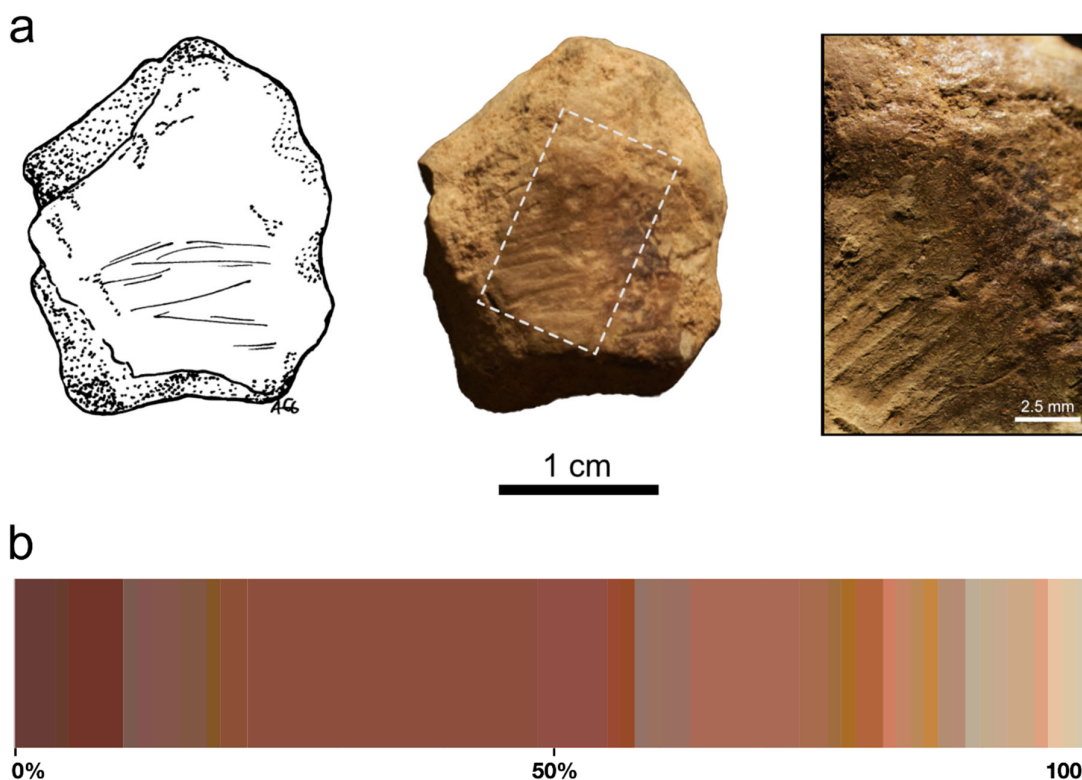
1142 pigment nodules are unmodified, but eight are ground, scraped, and/or polished (Figure S21;
 1143 Table S15). Two of the modified nodules have multiple wear facets including the prismatic
 1144 piece which has nine separate facets. The modified nodules streak a variety of colors
 1145 including pink, red, yellowish red, greyish red, and very pale brown when tested on a
 1146 ceramic tile (Figure S21).

1147
 1148

Table S15. Number of pigment modified and unmodified nodules by morphology, I-08 & I-09.

Pigment nodule morphologies	Number of pigment nodules	Number of modified nodules
Chunk	23	4
Flake	6	0
Lump	4	0
Prismatic	1	1
Tabular	1	1
Small chip	6	0
Small chunk	25	2
Small lump	12	0
TOTAL	78	8

1149
 1150



1151
 1152
 1153
 1154
 1155
 1156

Figure S21. (A) Pigment nodule VR003-8511 (I-08) with anthropogenic modifications including polish and grinding with minor burning on the surface. This nodule is characterized as a chunk, weighs 4.18g, measures 24.74 x 19.9 x 9.97mm, and streaks a very pale brown color (Munsell color system: 10YR 7/3). (B) Proportion of pigment colors from Lower Deposits when streak on a ceramic tile.

1157 **Lithics**

1158 We begin this section by providing a detailed description of the Lower Deposits lithic
 1159 assemblage before providing an overview of potentially comparable MSA assemblages from
 1160 across southern Africa. We conclude by evaluating whether the characteristic technologies
 1161 of the Lower Deposits are similar to any other published datasets.

1162

1163 **Lower Deposits lithic data.** The analysed assemblage from the Lower Deposits comprises
 1164 3062 flaked artefacts >15 mm; artefacts below this cut-off were not analysed individually.
 1165 The breakdown of primary classes by raw material is given in Table S16. Silcrete is the
 1166 single most common rock type in the sample (41.6%), followed by quartz (29.8%) and
 1167 quartzite (20.9%); between them these three lithologies account for more than 90% of the
 1168 artefacts. The fine-grained rocks hornfels and chert account for a further 6.2% of artefacts,
 1169 followed by the ‘other’ category which includes sandstone, shale, ironstone, limestone and
 1170 unidentified igneous lithologies. The raw material composition of the Lower Deposits is
 1171 interesting relative to previously published strata from the site: in all other units which we
 1172 have analysed, quartz was the dominant rock (>50% of total) and silcrete never exceeded
 1173 17% (1).

1174

1175 **Table S16.** Breakdown of flaked lithic assemblage from I-08 and I-09 by raw material and artefact
 1176 class.

	silcrete	quartz	quartzite	hornfels	chert	other	total	%
flakes	813	712	554	76	66	26	2247	73.4
retouched flakes	29	44	18	10	4	1	106	3.5
cores	72	25	13	3	4	0	117	3.8
flaked pieces	67	119	26	4	7	8	231	7.5
heat shatter	313	9	20	8	5	6	361	11.8
total	1294	909	631	101	86	41	3062	
%	41.6	29.8	20.9	3.3	2.9	1.4		100.0

1177

1178 Flakes are the most common of the primary artefact classes (73.4%), with cores (3.8%) and
 1179 retouched flakes (3.4%) having similarly low frequencies. Heat shattered pieces – pieces
 1180 formed by heat-induced fracture – account for 11.8% of the total. This abundance is driven
 1181 principally by silcrete among which it accounts for nearly a quarter (24.2%) of all artefacts,
 1182 including many large pieces (Figure S22). Among all other raw materials combined heat
 1183 shatter accounts for 3.0% of artefacts, with hornfels (8.8%) having the highest value after
 1184 silcrete. This pattern might partly be explained by the relative identifiability of heat effects on
 1185 different lithologies. The characteristics of heat shatter are generally visually-obvious on fine-
 1186 gained sedimentary/metamorphic rocks such as silcrete, chert and hornfels, and to an extent

1187 on the coarse-grained rocks such as quartzite, but can be hard to identify on crystalline
 1188 rocks like quartz which often exhibit non-conchoidal fracture. This does not, however,
 1189 explain the differences observed here for heat shatter frequencies between silcrete, chert
 1190 and hornfels. Chert should be more sensitive to shatter than silcrete (141).

1191

1192 Notable variation is also observed in the prevalence of other primary artefact classes by raw
 1193 material. Silcrete, for example, contributes the majority of the cores (61.4%) but only 27.4%
 1194 of the retouch flakes. Indeed, silcrete is only the lithology in which cores exceed retouched
 1195 flakes. Among other rock types the retouched flake to core ratio varies from 1 (chert / other)
 1196 to 3.3 (hornfels); for silcrete the value is 0.4. These base data suggest differences in the
 1197 delivery and treatment of silcrete vs non-silcrete artefacts in the Lower Deposit assemblage.
 1198 Complete flakes were classified into three shape types: flakes, blades and points (Figure
 1199 S23). We define blades here as any flake with elongation (percussion length / maximum
 1200 percussion width) of 2 or greater. We do not distinguish blades and bladelets, and given our
 1201 cut-off of 15 mm many of the latter would have been missed during analysis. 'Points' we
 1202 define as flakes with a consistent taper through at least their distal two-thirds. The type
 1203 'flakes' refers to any shape that does not conform to these other types. Where points are
 1204 elongate the type 'point' was selected over the type 'blade'.

1205

1206 **Table S17.** Numbers of different flake types in the Lower Deposits divided by raw material, complete
 1207 flakes only.

	silcrete	quartz	quartzite	hornfels	chert	other	total	%
flakes	434	323	269	37	35	14	1111	88.7
blades	36	14	20	10	3	0	83	6.6
points	24	8	20	3	4	0	59	4.7
total	494	345	309	50	42	14	1253	

1208

1209 Flakes dominate the sample (88.7%) with both blades and points relatively uncommon (6.6%
 1210 and 4.7% respectively) (Table S16). Values for both are consistent across raw material
 1211 classes with the exception of hornfels, where blades comprise an anomalous 20%,
 1212 potentially implying different reduction patterns for that rock type. Only 18 (21.7%) of the
 1213 blades related to laminar (unidirectional or bidirectional opposed) reduction systems,
 1214 suggesting that the presence of the blades in the assemblage was largely incidental.
 1215 Consistent with this, evidence for formal establishment and/or maintenance of blade
 1216 removals is minimal; following Soriano, Villa and Wadley (142) most of the blades fail to
 1217 conform to standard types (Table S18). The single class 'C' (maintenance) crested blade we
 1218 identified is only partially crested, with the crest in lateral position. This artefact is made from
 1219 silcrete and the proximal area of the left lateral reflects an episode of thermal fracture that
 1220 occurred before the flake was struck (Figure S23 e). The scars that comprise the crest are

1221 smooth and lustrous, and consistent with working after heat treatment. Thus, the flake was
 1222 struck from a core that had been heated to the point of fracture.

1223

1224 **Table S18.** Blade types from I-08 and I-09 following (142). Empty columns (i.e., those with null
 1225 values: classes B3, B5, B11, B13, B14, D1) are excluded. Class A blades reference initial phases of
 1226 production (cortical blades); class B blades derive from the optimal phase; class C blades are those
 1227 used for maintenance of core morphology; class D blades are those that do not conform with any of
 1228 the standard definitions.

	A1	A2	A3	B1	B2	B4	B6	B7	B8	B9	B10	B12	C2	D2
silcrete	1	2	2	5				2	1	1			1	20
quartz				2	2	1	1		1	1				6
quartzite	2			2			1		1	1		1		11
hornfels				1	1	2	1		1		1			3
chert	1									1				1
total	4	2	2	10	3	3	3	2	4	4	1	1	1	41

1229

1230 Like blades, point production in our assemblage mostly seems opportunistic or incidental
 1231 (Table S18). Only seven of 59 (11.8%) exhibit platform and dorsal scar configurations
 1232 suggestive of Levallois reduction; across the entire sample this amounts to 0.6% of complete
 1233 flakes. A further ten points (16.9%) appear to relate to discoidal flaking patterns. One of
 1234 these was made from chert and refits to an earlier flake (Figure S7), suggesting that at least
 1235 some of these points were made on site. As we note, though, there is nothing in the flake
 1236 component to suggest that manufacture of points was an objective of reduction at the site.

1237

1238 Almost half of all flakes (46.5%) – including flakes, blades and points – have cortex (Table
 1239 S19). Presence and prevalence of cortex between raw materials is quite consistent, varying
 1240 from 41.2% (chert) to 56.8% (hornfels). Notably less well-represented lithologies present the
 1241 outlying values, possibly reflecting sample-size effects. Within the main raw materials,
 1242 variance is from 42.8% (silcrete) to 51.4% (quartzite). Similarly, proportions of flakes with
 1243 cortical coverage across more than half of the dorsal and platform surfaces do not vary
 1244 greatly between raw materials (7.5% (silcrete) to 10.3% (chert)). The main point of contrast
 1245 in cortex between raw materials is in its form (Table S20). Quartzite and hornfels, which are
 1246 both available in ancient cobble beds in the area, generally have fluvial cortex as their most
 1247 common type (62.4% and 40.0% respectively); silcrete and quartz, the two flakable rocks
 1248 that occur commonly as primary sources in the area, have very high proportions of outcrop
 1249 cortex (83.8% and 74.1% respectively).

1250

1251 **Table S19.** Cortex classes for all complete flakes in I-08 and I-09.

	silcrete	quartz	quartzite	hornfels	chert	total	%
51-100	35	29	25	4	4	97	8.6

26-50	33	21	33	6	0	93	8.0
1-25	127	112	74	15	12	340	29.9
0	299	183	177	25	26	710	53.5
total	494	345	309	50	42	1240	

1252

1253

Table S20. Cortex types for all complete flakes in I-08 and I-09.

	silcrete	quartz	quartzite	hornfels	chert	total
outcrop	160	120	6	4	5	295
fluvial	9	11	82	10	2	114
crystal	0	5	0	0	0	5
unsure	26	28	44	11	9	118
total	195	164	133	25	16	533

1254

1255

The 103 retouched flakes in the Lower Deposits include 63 complete pieces that we discuss briefly here. Notched pieces – comprising simple notches formed by a single blow and complex notches formed by multiple removals from the same concavity – are the most common retouched artefact type. These are followed by denticulates, defined as artefacts with three or more adjacent notches along a single margin. A very high proportion (41.9%) of retouched pieces could not be assigned to any type. Among the major lithologies, these ‘informal’ retouched pieces are most common on silcrete artefacts (60%); quartz has the next highest proportion at 41.7%. The retouched silcrete artefacts include one denticulate made on a piece of heat shatter. This is one of only three examples of retouch on heat shattered fragments (see Table S23 below) (e.g., Figure S23 m).

1265

1266

Table S21. Retouch flake types in I-08 and I-09 by raw material.

	silcrete	quartz	quartzite	hornfels	chert	Other	total
Denticulate	2	5	2	0	0	0	9
Notch, simple	3	4	6	2	0	0	15
Notch, complex	2	1	0	1	0	0	4
Scaled piece	0	1	1	2	0	0	4
Scraper	1	3	0	0	0	0	4
Other	12	10	2	0	2	1	27
total	20	24	11	5	2	1	63

1267

1268

Silcrete cores have been discussed in some detail in the main text; here we discuss the core assemblage as a whole (n=91, Table S22). As noted in the main text, the types of cores found in the Lower Deposits is quite diverse. ‘Other prepared’ pieces – comprising those with preparation of the striking platform but no clear organisation of the removal surface – are numerically most common, along with cores that conformed to no type. Most of these latter pieces were opportunistic, 23 of 24 (95.8%) having three or fewer removals >20% of the core maximum dimension. The ‘platform’ groups includes cores that are not technically single platform – they may have one or two blows from from a second surface – but which

1269

1270

1271

1272

1273

1274

1275

1276 have a series of removals along a single dominant, and invariably linear platform. Bipolar
 1277 working is extremely rare across all materials (n=1).
 1278
 1279 Generally speaking the non-silcrete cores are similar many respects to the silcrete cores.
 1280 Those made from quartz (n=20), chert (n=3), and hornfels (n=2) have similar maximum
 1281 dimensions (mean=34.2, ± 11.0 mm), numbers of removals (3.3), flake scar lengths (17.1
 1282 ± 7.3 mm) and types as the silcrete cores. Quartzite cores (n=12) are appreciably larger than
 1283 those on other lithologies (61.7 ± 26.2 mm), with larger scars (26.9 ± 9.4 mm), and more
 1284 scars per core (4.4). Generally speaking, however, cores from all materials in I-08 and I-09
 1285 were dedicated to the expedient production of small flakes and blades.
 1286
 1287 Consistent with earlier observations on the flake component, evidence for blade production
 1288 is rare: only 7 of the 91 (7.7%) complete cores retained one or more blade removal. Point
 1289 removals were even less common (n=4, 4.4%). Of the blade removals recorded, most were
 1290 extremely small, with a mean of 16.3 mm (± 6.2).

1291
 1292

Table S22. Core types by raw material, I-08 and I-09.

	silcrete	quartz	quartzite	hornfels	chert	Other	total
Bipolar	0	1	0	0	0	1	2
Discoidal	3	1	1	0	0	0	5
Levallois, preferential	3	1	2	0	0	0	6
Levallois, recurrent	5	0	1	1	1	0	8
Other prepared	15	5	3	1	0	0	24
Platform	10	3	1	0	1	0	16
Rotated	4	1	1	0	0	0	6
No type	13	8	3	0	1	0	24
total	53	20	12	2	3	1	91

1293
 1294
 1295
 1296
 1297
 1298
 1299
 1300
 1301
 1302
 1303
 1304

Heat effects are prevalent in the Lower Deposits, but as noted in the main text, most commonly on silcrete. To that end, we restrict discussion of heat effects here to that raw material. Like prior sections of this SI, we exclude incomplete pieces to avoid duplicate counts of what may have been individual artefacts. Heat effects are classified following (143, 144). Without a detailed reference collection the identification of post-heat removals is subjective, relying on the evaluation that flake scars are smoother and more lustrous than might be expected for unheated silcrete. The classification 'unsure' was thus used quite frequently during analysis, and the firm identification of heat treatment largely restricted to those pieces with clear texture contrast between adjacent and/or sequential removal events, including double patina and surfaces with heat-induced non-conchoidal (HINC) fracture (Table S23).

1305

1306 Overall, 39.4% of silcrete artefacts appear likely to have been heated and 35.8% might
1307 confidently be classified as ‘heat treated’ in the sense that they were thermally altered before
1308 being worked (ie., all heated excluding ‘HINC – Flaked before’ and ‘HINC – Unsure’). Of
1309 those with clear signs of heat shatter (HINC fractures) at some point before or after discard,
1310 a very high proportion (79.8%) were flaked after shatter. Excluding those for which the
1311 sequence of shatter and flaking cannot be identified (HINC – Unsure) this value rises to
1312 96.3%.

1313

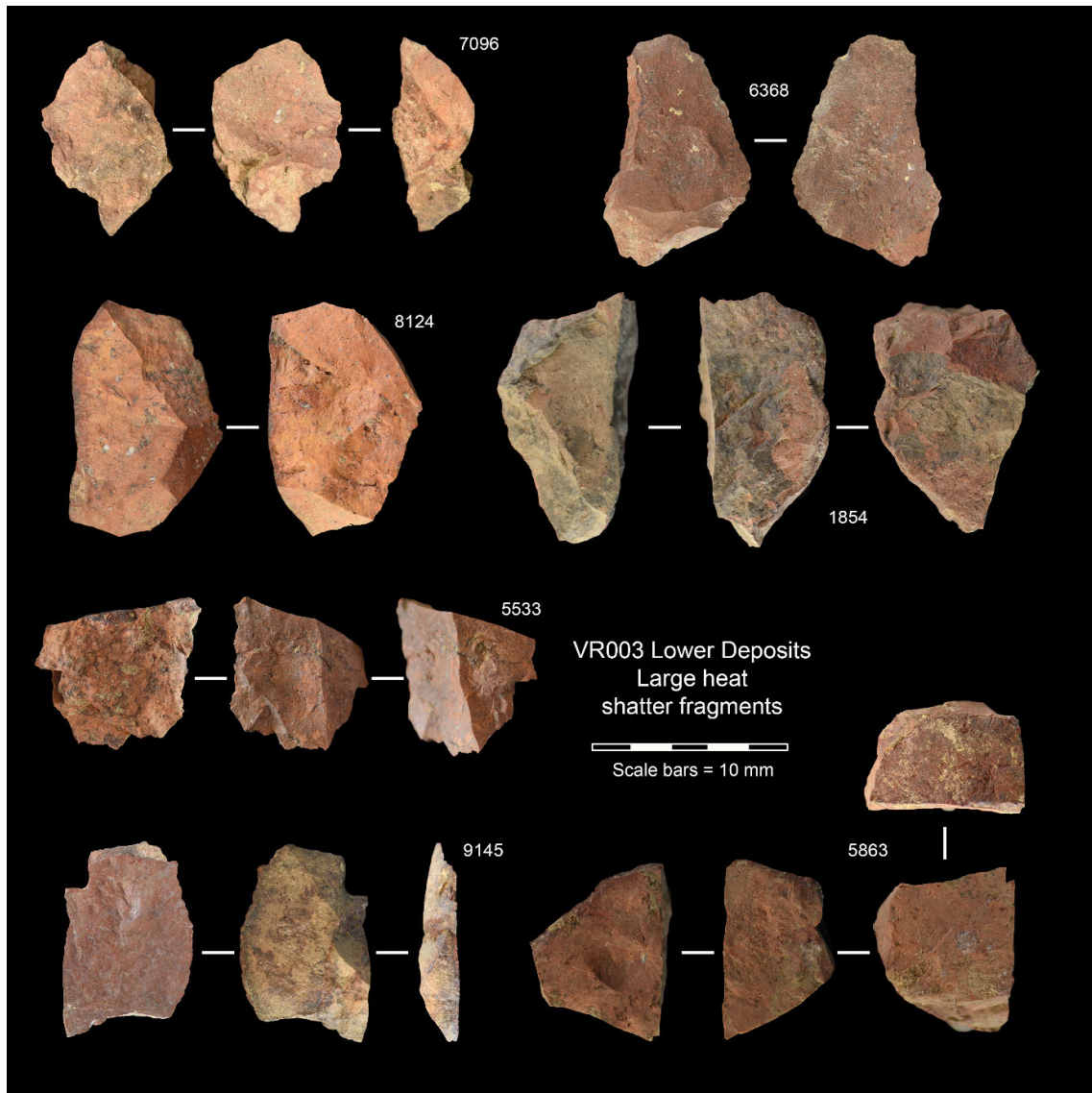
1314 Evidence for heat effects occurs unevenly between different artefact classes. Approximately
1315 two thirds of all unretouched flakes (65.4%) and half of all retouched flakes (48.4%) show no
1316 clear signs of heat effect. This is true of only 5.6% of cores. Types of heat effects differ just
1317 as starkly. Heat treated pieces with no evidence of HINC are twice as common as pieces
1318 flaked after shatter among complete flakes and complete retouched flakes; among cores
1319 pieces flaked after shatter are twice as common as those with no evidence of HINC. Most
1320 simply, this difference may reflect flakes removed from areas of a heated core from which
1321 HINC fractures were absent. It is also possible that these flaking products derive from a heat
1322 treatment system in which heat-induced fracture was less prevalent. Based on the evidence
1323 from the silcrete cores in the Lower Deposits, however, such activities may have taken place
1324 off site.

1325

1326 **Table S23.** Classification of heat effects on silcrete artefacts of different classes, I-08 and I-09.
1327 Double patina excludes pieces with HINC features. Flaked before, Flaked after, Both, and Unsure
1328 refers to the sequential relationship between the shatter event creating the HINC fracture and any
1329 flaking events evident on the piece.

Artefact class	No heat	Unsure	Heated						Total
			Post-heat removals	Double patina	HINC				
					Flaked before	Flaked after	Both	Unsure	
flakes	66	257	48	47	3	55	2	16	494
retouched flakes	1	8	1	5	0	3	0	1	19
cores	1	2	3	14	0	32	0	1	53
Total	68	267	52	66	3	77	2	17	553

1330



1331

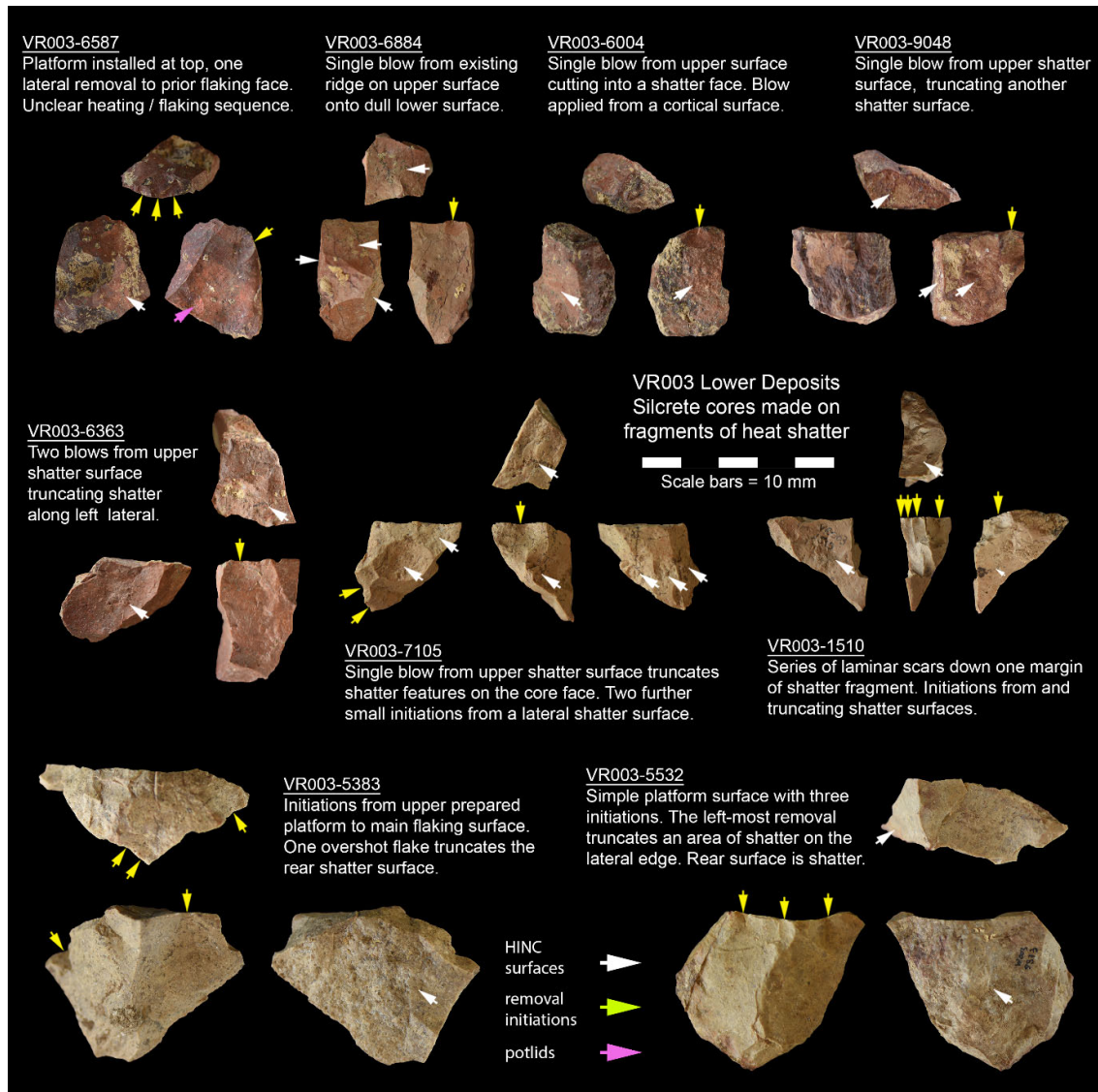
1332 **Figure S22.** Large, blocky, unworked silcrete heat shatter fragments from the Lower Deposits.

1333



1334

1335 **Figure S23.** Flakes and unretouched flakes from the Lower Deposits. White arrows are used to
 1336 indicate locations of HINC fractures that have been truncated by subsequent removals. (a-c) silcrete
 1337 blades; (a) was heat shattered after manufacture, as indicated by HINC (potlids) on the ventral
 1338 surface. (d) silcrete point with double patina on the left side (dorsal view) – note the texture contrast
 1339 between the proximal (later) and distal (earlier) scars. (e-f) silcrete blades, including (e) partially
 1340 crested blade; (f) was struck from a ridge formed by heat shatter. (h) hornfels blade with percussion-
 1341 shattered bulb. (i) silcrete flake with HINC on distal right lateral, truncated by the ventral. (j-k)
 1342 denticulate and notched (respectively) quartz flakes. (j) hornfels scaled piece. (m) silcrete notched
 1343 piece with HINC fracture truncated by both the ventral and one retouch scar. (n) silcrete complex
 1344 notch. (o) silcrete scraper, retouch has removed the platform.



1345

1346 **Figure S24.** Annotated figure showing silcrete cores made on fragments of heat shatter.

1347

1348 **The Lower Deposits lithic technology in context.** A wide variety of industry/technocomplex
 1349 terms combined with a small number of consistently dated assemblages complicates
 1350 reviews of the pre-Still Bay lithic technology of southern Africa. The term 'pre-Still Bay' itself
 1351 presumes the existence of the Still Bay as a regional horizon marker, though it probably
 1352 cannot function that way given: [1] Still Bay assemblages are quite rare (145), [2] there does
 1353 not appear to be a Still Bay in some regions (146), [3] the bifacial points used to define
 1354 discrete Still Bay horizons in the west and south-west of South Africa (147, 148) are a
 1355 recurrent feature of assemblages in the east and north-east (149, 150), and [4] regional
 1356 differences in bifacial point morphology (151, 152), coupled with chronometric
 1357 inconsistencies (e.g., 12, 153, 154), precludes the assumption that all such bifacial point

1358 assemblages are related (155). The broader term 'Early MSA' is not obviously more useful.
1359 Some apply this to any assemblage inferred to be of MIS 5 age or greater (156); others
1360 restrict it to assemblages inferred to ante-date the MIS 5e highstand (157-160). In either
1361 case the Early MSA, like the pre-Still Bay, lacks unifying technological characteristics and
1362 doesn't provide an obvious mechanism for dealing with undated assemblages.

1363

1364 Given that our interests here are quite narrow, we approach this review through the lens of a
1365 specific question: what other MSA assemblages resemble those from the Lower Deposits at
1366 VR003? We define the technological characteristics of the Lower Deposit lithic assemblages
1367 as follows: [1] focussed procurement of silcrete, [2] use of heat fracture to create core
1368 blanks, [3] dedicated production of small flakes and blades across most raw materials, [4]
1369 short reduction chains in the dominant core component, [5] elevated rates of heat shatter, [6]
1370 rare and opportunistic production of blades and points, [7] relatively few retouched artefacts,
1371 [8] notches and denticulates as the most common implement forms, and [9] near-absence of
1372 bipolar reduction. Not all of these characteristics are reported on in published analyses of
1373 other sites, but enough information is available in most cases to make a reasonable
1374 assessment. Characteristic [1] is only applicable to silcrete-bearing regions around the
1375 southern and western coastal margins of South Africa (161); in other areas an equivalent
1376 characteristic could be redefined as 'predominance of a raw material that is otherwise rare in
1377 the sequence'. Further note that, so far, heat treatment in the MSA has only been
1378 demonstrated to have been applied to silcrete (162-165). Consequently characteristics [2]
1379 and [5] are also likely to be geographically constrained.

1380

1381 We take a two part approach to this review. We start by using the defining characteristics of
1382 the prevailing MIS 5 culture-historic taxonomies (ie., 'technocomplexes') in the region,
1383 including Klasies River / Mossel Bay / pre-Still Bay (158, 159, 166), and the recently re-
1384 emerging Pietersburg (167-169). Following (170) we appreciate that these culture-historic
1385 taxa are normative and typically act to suppress inter- and intra-assemblage variation,
1386 creating the appearance of coherence where it may not exist (156). We thus document site-
1387 specific variance within these taxa where possible. Subsequently, we provide detailed data
1388 on assemblages likely to ante-date the Still Bay from the six MSA sites within 100 km of
1389 VR003 both from published sources and from our own analyses.

1390

1391 *Major technocomplex comparisons.* The foundational MSA culture-historic taxonomy
1392 proposed by Volman (171) remains influential but has recently been updated by Lombard
1393 and colleagues (159), and Wurz (158), with important further supplementary information in
1394 (172). We follow their naming conventions here. It is worth recalling, though, that Volman's

1395 original focus was on the southern Cape region that today largely falls within the Fynbos
1396 Biome. Regions to the north and east—those receiving predominantly summer rain and
1397 including the Grassland and Savanna Biomes—were not always well served by that system.
1398 With a recent resurgence of interest in the MSA of this area (167-169, 173, 174), the
1399 historical Pietersburg Industry has been somewhat revitalised as a regional MSA
1400 technocomplex tentatively assigned to MIS 5 (167, 168).

1401

1402 Klasies River. The Klasies River unit is assigned a putative age of 130-105 ka, and has been
1403 identified at sites including Klasies River and Pinnacle Point 13b (159) (Figure S25). Defining
1404 characteristics are “a recurrent blade reduction strategy”, elongate flaking products with
1405 diffuse bulbs, low frequencies of retouch, and denticulated pieces. Further sites with
1406 assemblages in the age range of this taxon are Florisbad, Hoedjiespunt and Ysterfontein
1407 (59, 175, 176), though they appear to have different technological characteristics (158).

1408

1409 The relevant LBS member at Klasies River Main site has large cores dedicated to blade
1410 production, with almost all artefacts made from quartzite, and negligible silcrete ('non-local',
1411 a term used for rocks that include silcrete, totals 0.2-0.4% in these assemblages). Quartzite
1412 also dominates the LC-MSA 5e and East 5d assemblages from Pinnacle Point 13b, though
1413 silcrete accounts for a reasonably elevated 12.6% of artefacts. There are very few cores in
1414 these deposits (177), and neither the presence nor prevalence of heat treatment in the
1415 assemblages at either site has been documented.

1416

1417 Heat treatment does occur at Hoedjiespunt (163), where quartz is the main raw material,
1418 bipolar cores the dominant type, and silcrete cores absent (176). On the other hand, silcrete
1419 is common at Ysterfontein 1 both overall (51.3%) and among cores specifically (47.1%)
1420 (178), though heat treatment has not been studied. The assemblage is characterised by the
1421 production of small flakes and blades (179), with cores described as 'platform' and 'two
1422 volume' (179), the latter corresponding to discoidal and/or Levallois reduction.

1423

1424 Florisbad is the only site in this grouping to lie outside the modern Fynbos Biome. Unit F has
1425 an age of 121 ±6 ka and an assemblage of ~1669 artefacts, almost all made from dolerite
1426 (175). Pointed flakes are relatively common, though it is not clear if blades per se are
1427 present, and if so in what quantity. The most common implements are described as 'cutting
1428 tools' – flakes showing either minor retouch or use damage. The only other types present
1429 are burins and sidescrapers.

1430

1431 Mossel Bay. Lombard et al (159) assign the Mossel Bay taxon an age range of 105-77 ka,
1432 and identify it at Klasies River, Pinnacle Point, and potentially Melikane, with undated
1433 examples at Cape St Blaize and Nelson Bay. With the exception of Melikane, all of these
1434 sites are located within the modern Fynbos Biome. Wurz also assigns unspecified layers at
1435 Diepkloof to the Mossel Bay (probably MSA-Mike and earlier—see discussion below under
1436 *Individual site comparisons*), as well as Cave of Hearths, though we include the latter here
1437 under the Pietersburg. The Mossel Bay is defined by the production of points and blades by
1438 unipolar recurrent Levallois reduction, with low rates of retouch and few defined implement
1439 types (158, 159). Douze et al (172) extend this comparison to include the M3 unit at
1440 Blombos dating 98-82 ka (180), and provide seven characteristics that link all assemblages:
1441 “1) the dominant use of local raw material, 2) dominant parallel (Levallois-like) core reduction
1442 methods, 3) a combination of different core reduction methods for the production of blanks,
1443 4) a production of predetermined blanks, 5) a low percentage of retouched tools, 6) usually a
1444 dominance of notched or/and denticulated tools, and 7) the production of points” (p25). They
1445 consider the technocomplex to be a single coherent unit comparable to the Still Bay and
1446 Howiesons Poort.

1447

1448 In the Mossel Bay-assigned SAS Member at Klasies River, quartzite accounts for the
1449 majority of artefacts, and silcrete is again scarce ('non-local' ranges from 0.5% to 2.1%).
1450 Wurz (166: p1008) states that “The core reduction scheme in this sub-stage is clear, as
1451 almost all the cores and end products are uniformly patterned. Nearly all of the preparation
1452 of the core was directed at the production of Levallois-like points”. Cores in this unit are
1453 made either on large primary flakes or cobbles, and while retouch was typically rare,
1454 notching and denticulation were the most common forms. A minor departure from this
1455 pattern is found in the Witness Baulk sample reported by (181) dating ~110-93 ka where,
1456 though quartzite accounts for 90% of artefacts, there is some dedicated production of small
1457 blades. In the M3 at Blombos silcrete is the most common raw material, but the
1458 technological elements are strongly similar to the typical Mossel Bay elements at Klasies
1459 River (172). Again, there has been no discussion of the role of heat treatment in these
1460 assemblages or their technological organisation.

1461

1462 At Pinnacle Point 5-6 quartzite is the major raw material in the stratigraphic aggregates YBS
1463 (96 ± 6 ka), YBSR (89 ± 5 ka) and LBSR (91 ± 4 ka), though silcrete accounts for 25.7% of all
1464 artefacts and 45.7% of cores (182). Almost half of the silcrete cores produced blades or
1465 bladelets. Cores on heat shatter are not included in the extensive dataset provided by
1466 Wilkins and colleagues (182), though heat treatment was likely applied to silcretes in the

1467 LBSR unit at least (183). Bipolar cores are notably rare in these assemblages, despite a
1468 diverse core corpus geared towards the production of a range of blades, points, and flakes.
1469
1470 Inclusion in this technocomplex of Melikane, located in the modern Grassland Biome in
1471 Lesotho, seems questionable. The Phase IV assemblage there has ages of 83.2 ± 6.2 ka and
1472 79.5 ± 3.1 ka, but its technological characteristics feature the production of small blades from
1473 multi-directional cores made on locally-available chert pebbles, and their subsequent
1474 reduced by bipolar techniques (184). There is no evidence of heat treatment, though this site
1475 falls outside the 'silcrete belt' and as noted earlier, heat treatment has not yet been
1476 documented on lithologies other than silcrete in the region. The distinct nature of the
1477 technological systems at Melikane suggest regional diversity of technological responses in
1478 the interval covered by the Mossel Bay taxon.
1479
1480 pre-Still Bay. The 'pre-Still Bay' is not a coherent taxon, and is used in Lombard et al (159) to
1481 denote undescribed or anomalous assemblages either underlying or immediately antedating
1482 the Still Bay. With Blombos M3 reassigned to Mossel Bay, the two remaining sites in this
1483 grouping are Rose Cottage Cave and Sibudu, both located outside the Fynbos Biome, in the
1484 Grassland and Savanna Biomes respectively. Both have ages that would otherwise place
1485 them in the Mossel Bay, perhaps further emphasising that MIS 5 technological diversity
1486 increases when sites outside the Fynbos Biome are considered.
1487
1488 Description of the pre-Still Bay (more accurately 'pre-Howiesons Poort' (185, 186))
1489 technology at Rose Cottage Cave remains limited, though a summary of ages from layers
1490 KUA through LEN range from $\sim 96-71$ ka (187). Chert is the most common rock, as at
1491 Melikane, though "sandstone and tuffaceous rocks" are more common in the pre-Still Bay
1492 than elsewhere in the sequence (186). Neither pointed flakes nor blades appear to be
1493 particularly common, and unifacial points are the most common implement type, followed by
1494 'knives'.
1495
1496 At Sibudu the pre-Still Bay layers are denoted D-A, and are older than 77.2 ± 2.1 ka with as
1497 yet no lower bounding age (174). Dolerite is the main raw material, comprising 83.9% of the
1498 published artefact sample. Fine-grained rocks hornfels and chert are rare (1.7% and 0.3%
1499 respectively), as is quartz (2.1%). Cores are also very uncommon (0.7%) though retouch
1500 (8.2%) is more frequent than at most MIS 5 assemblages. Reduction processes are geared
1501 towards the production of blades, and the main core type is given as 'platform', indicating
1502 typically unidirectional removals. Bipolar reduction is also common, however. As at Rose
1503 Cottage Cave, unifacial points are the most common implement type. This stands in contrast

1504 to all MIS 5 assemblages from the Fynbos Biome, with the exception of MSA-Lynn at
1505 Diepkloof (see below). Bifacial tools are the second most common implement type at
1506 Sibudu, followed by scrapers. Denticulates are present though infrequent.

1507

1508 Pietersburg. As with the 'pre-Still Bay', though it is long-established (188-190), whether the
1509 Pietersburg can be considered a coherent taxon is still unclear (168). Sites with published
1510 ages are few but include 227-77 ka at Border Cave (173), 150 ±14 ka at Olieboomspoor
1511 (169), 97 ±10 ka to 73 ±6 ka at Bushman Rock Shelter (167), and potentially 90 ka at
1512 Mwulu's Cave (191). Other sites that have been assigned to this grouping are Cave of
1513 Hearths and Lincoln Cave (172). All are located within the modern Grassland and Savanna
1514 Biomes.

1515

1516 de la Peña and colleagues (168) describe the Pietersburg as a technological succession,
1517 rather than an entity, from "triangular blanks/Levallois-like industries to bifacial/unifacial
1518 pieces/Levallois-like industries" (p25). Scrapers are also common in some sequence
1519 components (167), and denticulates in others (168). Almost all Pietersburg assemblages do
1520 appear to produce some bifacial points, however. Like other MIS 5 groupings, raw material
1521 selection appears to be highly localised, with quartzite the dominant rock at Mwulu's Cave
1522 and Olieboomspoor (168, 169), hornfels and quartz at Bushman Rock Shelter (167), and
1523 rhyolite, hornfels and basalt at Border Cave (173). There is no discussion of heat treatment
1524 in any Pietersburg sites, but it seems unlikely that any of the main raw materials would be
1525 suitable.

1526

1527 The assemblages underlying the Still Bay at Apollo 11 (192) are an uneasy fit with the
1528 Pietersburg, but have not been assigned to other technocomplexes. Volman (171)
1529 considered these assemblages most similar to those from Cave of Hearths. The artefacts
1530 include numerous large flakes and blades, but the retouched component is mainly
1531 denticulate with single unifacial point reported in (192). Consistent with the other sites
1532 considered in this review, raw material selection is localised, comprising quartzite and
1533 calcareous mudstone (combined >90%).

1534

1535 *Individual site comparisons.* We now review data from MSA sites located near to VR003,
1536 targeting the data most relevant to the identifying characteristics of the Lower Deposit
1537 assemblages. The sites relevant to this comparison are Putslaagte 8 (69.3 km) (193), Hollow
1538 Rock Shelter (76.3 km) (194, 195), Klipfonteinrand 1 (78.3 km) (171), Mertenhof (88.9 km)
1539 (196), Elands Bay Cave (91.3 km) (160, 171, 197), and Diepkloof (96.2 km) (147). All are
1540 located to the south of VR003 in what is today part of the Fynbos Biome, though Putslaagte

1541 8, Klipfonteinrand 1, Hollow Rock Shelter and Mertenhof all lie east of the Cederberg
1542 mountains close to the current boundary with the Succulent Karoo Biome (Figure 1). Elands
1543 Bay Cave and Diepkloof lie west of the mountains near the modern coastline. The data
1544 presented below are summarised in Table S24.

1545

1546 Putslaagte 8 has minor Howiesons Poort and Still Bay components, and the undated
1547 underlying MSA assemblage from layers FOBSS spits 6-14 is small. FOBSS6-8 and
1548 FOBSS9-14 had minor technological differences and are reported separately here. The
1549 prevailing raw materials across both units are hornfels and quartzite, which are locally
1550 abundant. Silcrete accounts for 1.4% of artefacts in FOBSS6-8 and 1.2% in FOBSS9-14
1551 later peaking at 21.9% during the LSA Robberg (CGBSS13-16). None of the 30 cores in
1552 FOBSS6-14 were made from silcrete. No observations were made on heat treatment,
1553 though heat shatter comprises 3.6% of artefacts in Mackay's dataset for FOBSS6-8 and
1554 1.4% for FOBSS9-14; only one of those pieces is silcrete. The FOBSS 6-14 assemblage –
1555 immediately underlying the putative Still Bay – contains some blades, but cores dedicated to
1556 blade or point production were not reported. In FOBSS 6-8 bipolar cores were reasonably
1557 common (n=4, 16.7%), as was retouch (4.8%) with scaled pieces (n=7) and denticulates
1558 (n=6) the most frequent types. In the underlying FOBSS 9-14 a few notches (n=2) and
1559 denticulates (n=1), along with one bipolar core (16.7%).

1560

1561 The shallow deposit at Hollow Rock Shelter has been excavated twice but the MSA
1562 component underlying the Still Bay has not been described in detail. In fact, it is unclear
1563 whether or not there is a pre-Still Bay component to the site, though an OSL age of 87 ± 6
1564 was obtained from a sample 200 mm below surface. Consequently the site is not included in
1565 the summary Table S24, but some observations are made here. Bifacial points are rare in
1566 the two deepest layers—IIIA and IIIB—reported by (198), as is silcrete (194, 199). Silcrete
1567 samples from the potential pre-Still Bay layers were too small for meaningful analysis by
1568 (199), though 45% of silcrete cores in the Still Bay were made on heat fractured blanks,
1569 intimating persistence/recurrence of that technological behaviour in MIS 4.

1570

1571 Klipfonteinrand was excavated by Parkington in 1969 and Mackay between 2011-2012. The
1572 MSA component of the site has Howiesons Poort and underlying MSA. Volman (171)
1573 analysed Parkington's MSA sample, though found that excavation had cross-cut depositional
1574 layers, resulting in a mixed assemblage of which Volman made a relatively cursory
1575 assessment. Nevertheless, he assigned the pre-Howiesons Poort MSA to MSA 2b in his
1576 scheme, equivalent to Mossel Bay above, with high proportions of quartzite, high rates of
1577 retouch, and few denticulates.

1578
1579 Mackay's (unpublished, manuscript in preparation) re-excavation differentiated four MSA
1580 strata—LGSS, BS, GGLBS & PBSS—the upper two of which were Howiesons Poort and the
1581 lower two unassigned to any technocomplex. Silcrete peaks at 23% in the Howiesons Poort,
1582 a value comparable to peak values at Putslaagte 8 (21.5%), which is only 15 km north, and
1583 the Still Bay at Hollow Rock Shelter (18.8) 5 km to the west. The earlier, pre-Howiesons
1584 Poort MSA layers include 5422 analysed artefacts. Silcrete varies between 7.0% (GGLBS)
1585 and 1.2% (PBSS), though it accounts for only 1.4% of artefacts overall, and only 1 of 98
1586 cores. Quartzite and sandstone are the main raw materials, comprising 77.8% of all artefacts
1587 in GGLBS and 94.2% in PBSS. These raw materials also account for 84.6% (GGLBS) and
1588 91.8% (PBSS) of cores in those two layers. Only 0.6% of artefacts were classified as heat
1589 shatter – no other analysis of heat treatment has been completed. Blades and convergent
1590 flakes respectively comprise 4.7% and 8.4% of artefacts in GGLBS, and 3.5% and 8.1% of
1591 complete flakes in PBSS. Several of the blades in PBSS are notably large, ranging from 80-
1592 120 mm. Retouched pieces comprise 6.0% of all artefacts across both units, with
1593 denticulates (n=74) and notched flakes (n=31) as the most common implements, though as
1594 noted in (200) it is not clear that these two types are meaningfully different.

1595
1596 Mertenhof is located a further 10.7 km south of Klipfonteinrand, and was excavated by
1597 Mackay between 2013-2015. Few results have yet been published so far, and the site
1598 remains undated, though the sequence contains Late MSA, post-Howiesons Poort,
1599 Howiesons Poort, Still Bay, and pre-Still Bay units (201, 202). Published data are so far
1600 limited, and thus we provide summary results from O'Driscoll's ongoing PhD analysis of
1601 1401 pre-Still Bay artefacts. The pre-Still Bay component of the sequence (originally DBS) is
1602 subdivided into four units, from youngest to oldest: SL, LAS, GLB, and LMS. Silcrete peaks
1603 at 32.2% of artefacts in the Howiesons Poort (202); among the pre-Still Bay units the highest
1604 value is 4.7% in SL, and the overall proportion is 1.1%. The major raw materials are
1605 quartzite (65.4%), hornfels (16.3%), and sandstone (10.1%). There are only 29 cores in the
1606 assemblage, most of which are quartzite (51.7%) and none of which are silcrete. Though
1607 rare overall (5.8%), quartz accounts for 24.6% of cores; bipolar working (24.1%) is
1608 correspondingly common. Heat shatter comprises 1.2% of the analysed assemblage overall,
1609 though no heat shattered pieces of silcrete were recorded. Convergent (point-like) flakes are
1610 common, as are blades, the latter including pieces comparably large to those at
1611 Klipfonteinrand. Both blades and convergent flakes are most common in unit LAS. Retouch
1612 is common ranging from 7.3% to 14.0%, with notches and denticulates the most frequent
1613 types.

1614

1615 Elands Bay Cave was initially excavated by Parkington in 1970 (203), and again by Porraz in
1616 2011 (197). The sequence is dominated by Later Stone Age occupation, though there are
1617 Late MSA and 'Early MSA' components. The Late MSA has ages of 35 ± 3 ka and 38 ± 3 ka,
1618 and the Early MSA has ages of 83 ± 14 ka and 236 ± 26 ka (204). Porraz and colleagues
1619 conclude that the Early MSA assemblage formed in MIS 6 (197). The published Early MSA
1620 sample comprises 1518 artefacts, dominated by quartzite (98.7%) (160). Silcrete contributes
1621 only 3 pieces (0.2%) to the Early MSA total, but in subsequent phases of the LSA rises to
1622 almost 50% (197). No markers of heat treatment were identified in the Early MSA sample.
1623 Core reduction is organised around the morphology of locally available quartzite blocks, and
1624 directed primarily towards the production of flakes. Core blanks comprise slabs (67.2%),
1625 flakes (13.8%), and indeterminate forms (19.0%). The most common reduction systems are
1626 described as planar—where removals are directed across the broad face of the core—and
1627 orthogonal—where removals are directed down the shortest face of the core. Bipolar
1628 working is a common component of the orthogonal reduction system though no specific data
1629 are available. Pseudo-Levallois points (8.2%) are modestly common and blades (2.3%) are
1630 rare, though 5.2% of cores were organised around blade production. Retouched pieces
1631 comprise 7.3% of the assemblage, with notches and denticulates the most common
1632 implement types.

1633

1634 Diepkloof contains a long MSA sequence, including post-Howiesons Poort, Howiesons
1635 Poort, Still Bay, and two 'pre-Still Bay' units denoted MSA-Lynn and MSA-Mike (147, 205).
1636 MSA-Lynn has ages of 100 ± 10 ka from Tribolo and colleagues (12), and bracketing ages of
1637 76.5 ± 3.3 ka and 88.4 ± 4.0 ka from Jacobs and Roberts (57). MSA-Mike has ages of 118-90
1638 ka (12), and 88.2 ± 4.4 ka to 93.3 ± 4.4 ka (154) from the same research groups.

1639

1640 The lithic assemblages from MSA-Lynn comprises 922 pieces >20 mm and has been
1641 extensively described by Porraz and colleagues (205). Quartzite (60.1%) and quartz (12.8%)
1642 are the dominant raw materials, though silcrete comprises a further 24.7%. This is elevated
1643 relative to other pre-Still Bay assemblages in the region, though lower than the peak value of
1644 65-66% during the Howiesons Poort at the site (147). Silcrete is over-represented in cores,
1645 accounting for 47.6% of the total (10 of 21). Heat treatment of silcrete is common (73-91%),
1646 though only 7.4% of pieces show HINC fractures. No specific data on proportions of heat
1647 shatter are presented, though Porraz et al ((205): p13) note "A few thermal fragments were
1648 recorded in the assemblage but whether heat shattering occurred as an accident during heat
1649 treatment or through post-depositional processes remains unclear in these cases". Mackay
1650 (206) analysed a column sequence from Diepkloof for his PhD, which included a small

1651 sample of layer Lynn (n=132) with silcrete proportions (28.0%) similar to those reported by
1652 Porraz (205). This sample included no heat shattered pieces.

1653

1654 Porraz et al (205) describe seven different lithic reduction sequences for MSA-Lynn. The first
1655 four relate to the production of flakes of different morphologies, though not all are
1656 represented by cores found at the site. The fifth sequence is directed towards the production
1657 of bladelets from silcrete cores, the bladelets having a mean bladelet length of 24.7 ± 7 mm.
1658 Bladelet production involves preparation through overhang removal and production of
1659 crested blades, with 40% of silcrete cores dedicated to bladelet production. Despite
1660 extensive analysis of heat treatment markers, there is no discussion of the use of heat
1661 shatter in this or any other reduction sequence in MSA-Lynn. The final two reduction
1662 sequences correspond to bipolar working, which account for 52.4% of cores, and the
1663 production of bifacial pieces (5.6% of assemblage total, including 13 bifacial pieces and 39
1664 shaping flakes). Porraz and colleagues discount the possibility that these artefacts are
1665 intrusive from the overlying Still Bay, but rather consider them a precursor to the
1666 technological systems that follow. In contrast to other nearby pre-Still Bay assemblages,
1667 unifacial points (n=19) and bifacial points (n=13) are the most common implement types in
1668 the assemblage; denticulates (n=6) and notches (n=2) are relatively rare. Retouch accounts
1669 for 7.8% of artefacts in MSA-Lynn overall.

1670

1671 MSA-Mike has much higher proportions of quartzite (86.3%) and correspondingly lower
1672 proportions of silcrete (3.9%) than MSA-Lynn. The role of heat in this assemblage has not
1673 been described, and no data are available on the proportion of heat shatter in (147, 205).
1674 Mackay's PhD sample from layer Mike is small (n=46) but includes no heat shattered pieces.
1675 Including all layers from MSA-Lynn to the base of the Diepkloof sequence Mackay recorded
1676 only 6 heat shattered pieces, comprising 0.4% of all analysed artefacts with a range from 0%
1677 to 0.6% (n=2321).

1678

1679 In the larger dataset used by Porraz et al (205), points constitute ~17% of all flakes, with
1680 production via two different system. One system complies with the definition of Levallois
1681 reduction, while the other involved exploiting angular core edges to produce elongate points
1682 with a triangular cross-section. Blades comprise ~13% of the flake total, and were largely
1683 produced via a unidirectional production system. Retouch rates in MSA-Mike are relatively
1684 low (2.9%), with denticulates and notches combined accounting for 32% of retouched
1685 pieces.

1686

1687 *Summary.* Information about lithic assemblages is presented inconsistently between MSA
1688 sites, making any broad review difficult. In this case we attempted to use a combination of
1689 specific and general data to assess which other MSA assemblages most resemble those
1690 from the Lower Deposits at VR003. It seems reasonably clear that there is no ready fit with
1691 any of southern Africa's major technocomplexes as currently defined. Silcrete is common at
1692 some sites during MIS 5—most notably along the southern Cape coast—but we could not
1693 find evidence for the systematic use of heat treatment to create core blanks among those
1694 sites. A focus on small flake and blade production was rare, with the exceptions of
1695 Ysterfontein and the MSA-Lynn at Diepkloof, both of which also had high proportions of
1696 silcrete within the assemblage generally and within cores specifically. Ysterfontein has been
1697 consistently dated to ~120 ka, however, making it around 30 000 years older than the Lower
1698 Deposits at VR003. There is also no published evidence for heat treatment at that site. We
1699 return to the case of MSA-Lynn momentarily.

1700

1701 Perhaps the major pattern to emerge from our review of the technocomplexes is that MIS 5
1702 was technologically diverse both within regions, but perhaps more appreciably between
1703 regions (156). Local raw material procurement is a consistent characteristic across all sites
1704 in all technocomplexes, but implement types in the Fynbos Biome sites are different to those
1705 in the modern Savanna and Grassland Biomes, and flaking systems are highly variable both
1706 within and between regions. To the extent that taxa like Klasies River or Mossel Bay are as
1707 coherent as they have been argued to be, it is doubtful that they can be applied beyond the
1708 Fynbos Biome sites for which they were originally defined. And that may be the primary
1709 conclusion to reach from this section of our review: lithic assemblages may be different in
1710 different regions, so given we know essentially nothing about the MSA of what is today
1711 Succulent Karoo, is it any surprise that the assemblages there are different again?

1712

1713 The closest analogue to the Lower Deposit assemblage was found in the MSA-Lynn at
1714 Diepkloof. None of the other sites within 100 km of VR003 resembled these assemblages,
1715 despite much of the data being collected by the same analysts using the same or similar
1716 protocols. The MSA-Lynn has high proportions of silcrete both generally and among cores
1717 specifically, high rates of heat treatment, and the dedicated production of small blades from
1718 silcrete cores. In the Jacobs and Roberts chronology, the age interval for MSA-Lynn also
1719 overlaps that for the Lower Deposits. There are important differences between these
1720 assemblages, however. Primarily, despite detailed data being available, there is no evidence
1721 that heat shatter was abundant or habitually used to create core blanks in this part of the
1722 Diepkloof sequence. Given the analysis conducted by P. Schmidt (205), and the
1723 supplementary data available from (206), it seem likely that this absence of evidence is

1724 evidence of absence. A second difference concerns the nature of these sequences
1725 themselves. At VR003, silcrete peaks in the Lower Deposits before falling away again
1726 through I-07 to I-05, increasing subsequently in the Still Bay and Howiesons Poort (I-04). At
1727 Diepkloof, the increase in silcrete in MSA-Lynn is sustained thereafter through to the post-
1728 Howiesons Poort (147). Supporting this, the unifacial and bifacial pieces that appear in MSA-
1729 Lynn also persist into subsequent layers. It is for these reasons that Porraz and colleagues
1730 (205) view MSA-Lynn as an immediate precursor to the Still Bay. That cannot be the case at
1731 VR003 Lower Deposits, which lacks unifacial and bifacial points, and sits at least half a
1732 meter below the Still Bay. Thus, even one set of ages allow for overlap between the Lower
1733 Deposits and MSA-Lynn, they are technologically and sequentially distinct.

1734 **Table S24.** Comparison of technological characteristics of MSA assemblages preceding the Howiesons Poort and/or Still Bay within 100 km of VR003. Data
 1735 sources are provided in the text. VR003=Varsche Rivier 003; PL8=Putslaagte 8; KFR=Klipfonteinrand; MRS=Mertenhof; EBC=Elands Bay Cave;
 1736 DRS=Diepkloof Rock Shelter. Hollow Rock Shelter was excluded due to lack of relevant data. Sites are organised by increasing distance from VR003.

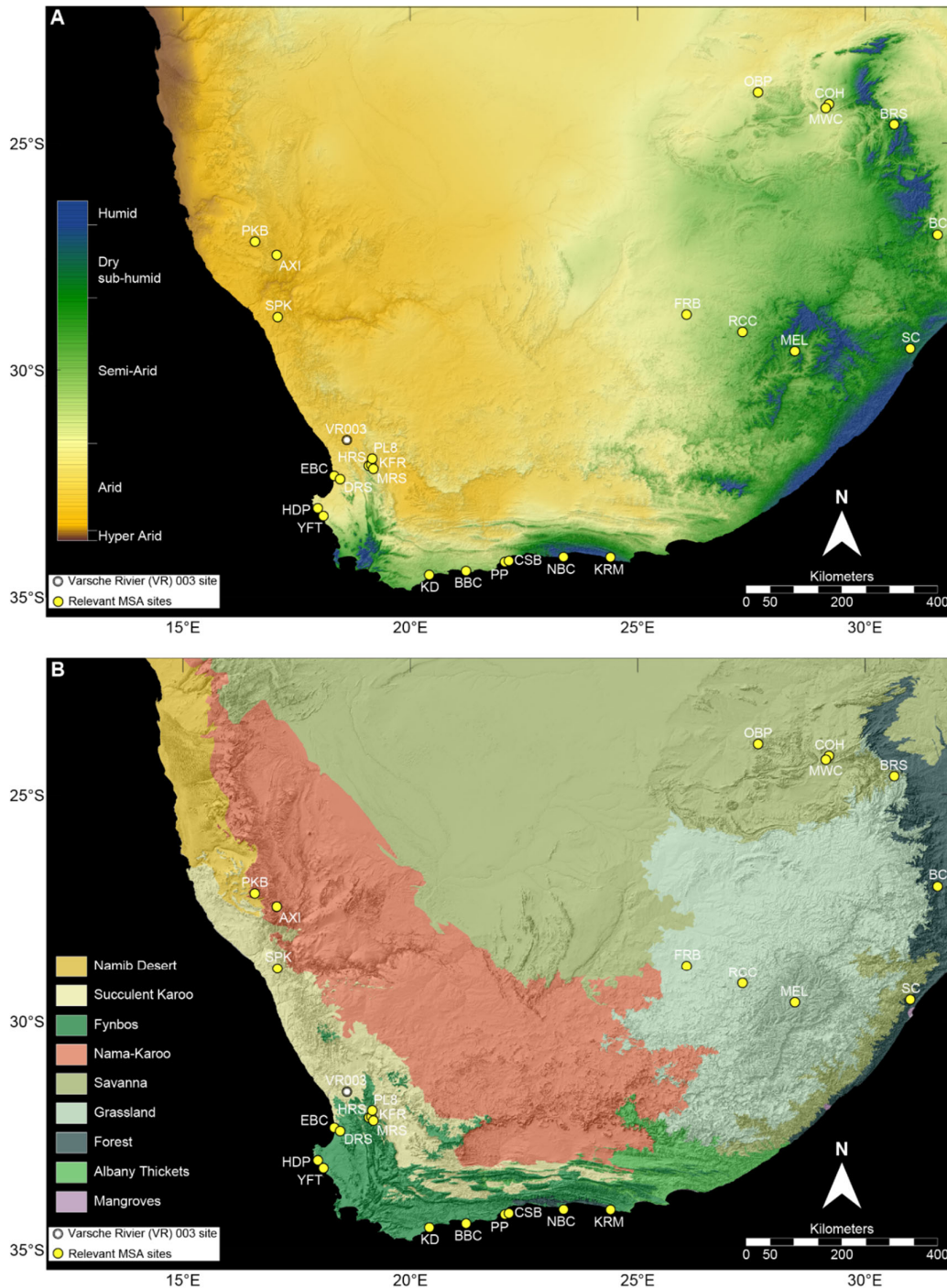
Site	VR003	PL8		KFR		MRS				EBC ^a	DRS ^b	
Layer	Lower Deposits	FOBSS 6-8	FOBSS 9-14	GGLBS	PBSS	SL	LAS	GLB	LMS	Early MSA	Lynn	Mike
Date	92-79 ka	-	-	-	-	-	-	-	-	83-236 ka	~100 ka or ~88-77 ka	118-90 ka or ~93-88 ka
% silcrete	41.6	1.4	1.2	7.0	1.2	4.7	0.6	0.6	2.7	0.2	24.7	3.9
% silcrete as ratio to site max. ^c	1.0	0.06	0.05	0.30	0.05	0.15	0.02	0.02	0.08	0.004	0.37	0.06
% silcrete heated	39-76	-	-	-	-	-	-	-	-	0	73-91	-
% heat shatter ^d	11.8	3.6	1.4	1.4	0.4	2.3	0.6	1.8	3.4	0	0-0.6	
% points	4.7	-	-	8.4	8.1	4.7	7.2	1.2	3.7	8.2	5.2	17.2
% blades	6.6	-	-	4.7	3.5	2.3	5.3	2.9	2.0	2.3	14.6	14.1
% retouch	3.5	4.8	1.4	7.1	5.8	14.0	7.3	12.4	8.8	7.3	7.8	2.9
Most common implements	notched, dentic.	scaled piece, dentic.	notched, dentic.	dentic., notched	dentic., notched	dentic.	notched, dentic.	dentic., notched	dentic., notched	notched, dentic.	Unifacial points, bifacial points	dentic., notched
% silcrete cores	61.5	0	0	0	1.2	0	0	0	0	0	47.6	0
% bipolar cores	2.2	16.7	16.7	0	1.1	0	27.3	33	21.4	-	52.4	-

1737 ^a As noted in the text, no published data are available for the proportion of heat shattered silcrete at DRS, and our (206) sample of these layers is quite small.
 1738 We thus provide an aggregate value for all 'pre-Still Bay' layers at the site, but note, as per the text, that (205) describe the number of pieces in MSA-Lynn as
 1739 'a few'.

1740 ^b We use the estimate in (197) for peak silcrete values at EBC, given no specific data are available.

1741 ^c We include the variable "% silcrete as ratio to site max." to control for the effect that variation the availability of silcrete may have on % silcrete values. In
 1742 areas such as the Olifants River valley, where high quality silcrete is abundant, values can reach >90% in the MSA (207). Both Diepkloof and Elands Bay
 1743 Cave have access to silcrete sources within 20 km, and their peak silcrete values are 50-66%. In the eastern Cederberg sites (PL8, KFR, MRS), the closest
 1744 known silcrete sources are no closer than 24 km (208), and peak silcrete values are typically 25-30%.

1745 ^d This variable includes all raw materials, not only silcrete, due to the way most available data are aggregated.



1746

1747 **Figure S25. (A)** Aridity map of southern Africa, with the Varsche Rivier 003 (VR003; white dot) and
 1748 relevant MSA sites referred to in the preceding review (yellow dots) indicated as follows:
 1749 AXI=Apollo11, BBC=Blombos Cave, BC=Border Cave, BRS=Bushman Rock Shelter, CSB=Cape St.
 1750 Blaize, COH=Cave of Hearths, DRS=Diepkloof, EBC=Elands Bay Cave, FRB=Florisbad,
 1751 HDP=Hoedjiespunt, HRS=Hollow Rock Shelter, KD=Klipdrift, KFR=Klipfonteinrand 1, KRM=Klasies
 1752 River Main site, MEL=Melikane, MRS=Mertenhof, MWC=Mwulu's Cave, NBC=Nelson Bay Cave,
 1753 OBP=Olieboompoort, PP=Pinnacle Point site complex, PL8=Putslaagte 8, RCC=Rose Cottage Cave,
 1754 SC=Sibuu Cave, VR003=Varsche Rivier 003, YFT=Ysterfontein. Aridity index data from (209) with
 1755 definitions according to (210). **(B)** Modern biome-bioregion map of southern Africa with VR003 and
 1756 other sites shown as in Pane (A). Biome-bioregion boundaries defined following (211, 212).

1757

1758 **References**

- 1759 1. Steele TE, *et al.* (2016) Varsche Rivier 003: A Middle and Later Stone Age site with Still Bay
 1760 and Howiesons Poort assemblages in southern Namaqualand, South Africa.
 1761 *PaleoAnthropology* 2016:100-163.
- 1762 2. Bertran P & Texier J-P (1999) Facies and microfacies of slope deposits. *Catena* 35:99-121.
- 1763 3. Villagran X, Strauss A, Alves M, & Oliveira RE (2019) Virtual micromorphology: The
 1764 application of micro-CT scanning for the identification of termite mounds in archaeological
 1765 sediments. *Journal of Archaeological Science: Reports* 24:785–795.
- 1766 4. Cosarinsky MI (2011) The nest growth of the neotropical mound-building termite,
 1767 *Cornitermes cumulans*: a micromorphological analysis. *Journal of Insect Science* 11:1-14.
- 1768 5. Jungerius PD, van der Acker JAM, & Múcher HJ (1999) The contribution of termites to the
 1769 microgranular structure of soils on the Uasin Gishu Plateau, Kenya. *Catena* 34:349-363.
- 1770 6. Francis ML, Ellis F, Lambrechts JJN, & Poch RM (2012) A micromorphological view through a
 1771 Namaqualand termitaria (Heuweltjie, a Mima-like mound). *Catena* 100:57-73.
- 1772 7. Genise JF & Poire DG (2000) Fluidization in insect constructions in soils. *Ichnos* 7:127-134.
- 1773 8. Lenoble A & Bertran P (2004) Fabric of Palaeolithic levels: methods and implications for site
 1774 formation processes. *Journal of Archaeological Science* 31(4):457-469.
- 1775 9. McPherron SP (2018) Additional statistical and graphical methods for analyzing site
 1776 formation processes using artifact orientations. *PLoS One* 13(1):e0190195.
- 1777 10. Steele TE, *et al.* (2016) Varsche Rivier 003: A Middle and Later Stone Age site with Still Bay
 1778 and Howiesons Poort assemblages in Southern Namaqualand, South Africa.
 1779 *PalaeoAnthropology*:100-163.
- 1780 11. Jacobs Z, *et al.* (2008) Ages for the Middle Stone Age of southern Africa: implications for
 1781 human behavior and dispersal. *Science* 322(5902):733-735.
- 1782 12. Tribolo C, *et al.* (2013) OSL and TL dating of the Middle Stone Age sequence at Diepkloof
 1783 Rock Shelter (South Africa): a clarification. *Journal of Archaeological Science* 40(9):3401-
 1784 3411.
- 1785 13. Mejdahl V (1985) Thermoluminescence dating based on feldspars. *Nuclear Tracks and
 1786 Radiation Measurements (1982)* 10(1-2):133-136.
- 1787 14. Guérin G, Mercier N, & Adamiec G (2011) Dose-rate conversion factors: Update. *Ancient TL*
 1788 29(1):5-8.
- 1789 15. Bøtter-Jensen L & Mejdahl V (1988) Assessment of beta dose-rate using a GM multicounter
 1790 system. *International Journal of Radiation Applications and Instrumentation. Part 14(1-
 1791 2)*:187-191.
- 1792 16. De Corte F, *et al.* (2007) Preparation and characterization of loess sediment for use as a
 1793 reference material in the annual radiation dose determination for luminescence dating.
 1794 *Journal of Radioanalytical and Nuclear Chemistry* 272(2):311-319.
- 1795 17. Brennan BJ, Lyons RG, & Phillips SW (1991) Attenuation of alpha particle track dose for
 1796 spherical grains. *International Journal of Radiation Applications and Instrumentation. Part*
 1797 *18(1-2)*:249-253.
- 1798 18. Guérin G, Mercier N, Nathan R, Adamiec G, & Lefrais Y (2012) On the use of the infinite
 1799 matrix assumption and associated concepts: A critical review. *Radiation Measurements*
 1800 47(9):778-785.
- 1801 19. Balescu S & Lamothe M (1993) Thermoluminescence dating of the holsteinian marine
 1802 formation of Herzelee, northern France. *Journal of Quaternary Science* 8(2):117-124.
- 1803 20. Mejdahl V (1987) Internal radioactivity in quartz and feldspar grains. *Ancient TL* 5:10-17.
- 1804 21. Neudorf CM, Roberts RG, & Jacobs Z (2012) Sources of overdispersion in a K-rich feldspar
 1805 sample from north-central India: Insights from D_e, K content and IRSL age distributions for
 1806 individual grains. *Radiation Measurements* 47(9):696-702.

- 1807 22. Gaar D, Lowick SE, & Preusser F (2014) Performance of different luminescence approaches
1808 for the dating of known-age glaciofluvial deposits from Northern Switzerland.
1809 *Geochronometria* 41(1):65-80.
- 1810 23. Lamothe M, Balescu S, & Auclair M (1994) Natural IRSL intensities and apparent
1811 luminescence ages of single feldspar grains extracted from partially bleached sediments.
1812 *Radiation Measurements* 23(2-3):555-561.
- 1813 24. Jacobs Z, *et al.* (2019) Timing of archaic hominin occupation of Denisova Cave in southern
1814 Siberia. *Nature* 565(7741):594-599.
- 1815 25. O'Gorman K, Brink F, Tanner D, Li B, & Jacobs Z (2021) Calibration of a QEM-EDS system for
1816 rapid determination of potassium concentrations of feldspar grains used in optical dating.
1817 *Quaternary Geochronology* 61.
- 1818 26. Huntley DJ & Baril MR (1997) The K content of K-feldspars being measured in optical dating
1819 or in thermoluminescence dating. *Ancient TL* 15(11-13).
- 1820 27. Smith MA, Prescott JR, & Head MJ (1997) Comparison of ¹⁴C and luminescence chronologies
1821 at Puritjarra rock shelter, central Australia. *Quaternary Science Reviews* 16(3-5):299-320.
- 1822 28. Durcan JA, King GE, & Duller GAT (2015) DRAC: Dose Rate and Age Calculator for trapped
1823 charge dating. *Quaternary Geochronology* 28:54-61.
- 1824 29. Bøtter-Jensen L, Andersen CE, Duller GAT, & Murray AS (2003) Developments in radiation,
1825 stimulation and observation facilities in luminescence measurements. *Radiation*
1826 *Measurements* 37(4-5):535-541.
- 1827 30. Duller GAT, Bøtter-Jensen L, Murray AS, & Truscott AJ (1999) Single grain laser luminescence
1828 (SGLL) measurements using a novel automated reader. *Nuclear Instruments and Methods in*
1829 *Physics Research, Section B: Beam Interactions with Materials and Atoms* 155(4):506-514.
- 1830 31. Duller GAT, Bøtter-Jensen L, & Murray AS (2003) Combining infrared- and green-laser
1831 stimulation sources in single-grain luminescence measurements of feldspar and quartz.
1832 *Radiation Measurements* 37(4-5):543-550.
- 1833 32. Armitage SJ & Bailey RM (2005) The measured dependence of laboratory beta dose rates on
1834 sample grain size. *Radiation Measurements* 39(2):123-127.
- 1835 33. Ballarini M, Wintle AG, & Wallinga J (2006) Spatial variation of dose rate from beta sources
1836 as measured using single grains. *Ancient TL* 24(1):1-7.
- 1837 34. Murray AS & Wintle AG (2000) Luminescence dating of quartz using an improved single-
1838 aliquot regenerative-dose protocol. *Radiation Measurements* 32(1):57-73.
- 1839 35. Roberts RG, Galbraith RF, Yoshida H, Laslett GM, & Olley JM (2000) Distinguishing dose
1840 populations in sediment mixtures: A test of single-grain optical dating procedures using
1841 mixtures of laboratory-dosed quartz. *Radiation Measurements* 32(5):459-465.
- 1842 36. Colarossi D, Duller GAT, & Roberts HM (2018) Exploring the behaviour of luminescence
1843 signals from feldspars: Implications for the single aliquot regenerative dose protocol.
1844 *Radiation Measurements* 109:35-44.
- 1845 37. Thomsen KJ, Murray AS, Jain M, & Bøtter-Jensen L (2008) Laboratory fading rates of various
1846 luminescence signals from feldspar-rich sediment extracts. *Radiation Measurements* 43(9-
1847 10):1474-1486.
- 1848 38. Li B, Jacobs Z, Roberts RG, & Li SH (2014) Review and assessment of the potential of post-ir
1849 irsl dating methods to circumvent the problem of anomalous fading in feldspar
1850 luminescence. *Geochronometria* 41(3):178-201.
- 1851 39. Roberts RG, Galbraith RF, Yoshida H, Laslett GM, & Olley JM (2000) Distinguishing dose
1852 populations in sediment mixtures: a test of single-grain optical dating procedures using
1853 mixtures of laboratory-dosed quartz. *Radiation Measurements* 32:459-465.
- 1854 40. Duller GAT (2003) Distinguishing quartz and feldspar in single grain luminescence
1855 measurements. *Radiation Measurements* 37(2):161-165.

- 1856 41. Balian HG & Eddy NW (1977) Figure-of-merit (FOM), an improved criterion over the
1857 normalized Chi-squared test for assessing goodness-of-fit of gamma-ray spectral peaks.
1858 *Nuclear Instruments and Methods* 145:389-395.
- 1859 42. Peng J, Pagonis V, & Li B (2016) On the intrinsic accuracy and precision of the standardised
1860 growth curve (SGC) and global-SGC (gSGC) methods for equivalent dose determination: A
1861 simulation study. *Radiation Measurements* 94:53-64.
- 1862 43. Peng J & Li B (2017) Single-aliquot regenerative-dose (SAR) and standardised growth curve
1863 (SGC) equivalent dose determination in a batch model using the R package 'numOSL'.
1864 *Ancient TL* 35:32-53.
- 1865 44. Peng J, Dong Z, Han F-Q, Long H, & Liu X-J (2013) R package numOSL: numeric routines for
1866 optically stimulated luminescence dating. *Ancient TL* 31:41-48.
- 1867 45. Guralnik B, *et al.* (2015) Radiation-induced growth and isothermal decay of infrared-
1868 stimulated luminescence from feldspar. *Radiation Measurements* 81:224-231.
- 1869 46. Galbraith RF, Roberts RG, Laslett GM, Yoshida H, & Olley JM (1999) Optical dating of single
1870 and multiple grains of quartz from Jinmium rock shelter, northern Australia: Part I,
1871 experimental design and statistical models. *Archaeometry* 41(2):339-364.
- 1872 47. Kreutzer S, Schmidt C, Fuchs MC, Dietze M, & Fuchs M (2012) Introducing an R package for
1873 luminescence dating analysis. *Ancient TL* 30:1-8.
- 1874 48. Armitage SJ, Krishna A, Parker LE, & King GE (2019) Optically stimulated luminescence dating
1875 of heat retainer hearths from the Sahara: Insights into signal accumulation and
1876 measurement. *Quaternary Geochronology* 49:249-253.
- 1877 49. Galbraith RF & Green PF (1990) Estimating the component ages in a finite mixture. *Nuclear*
1878 *Tracks and Radiation Measurements* 17(3):197-206.
- 1879 50. Guérin G, Jain M, Thomsen KJ, Murray AS, & Mercier N (2015) Modelling dose rate to single
1880 grains of quartz in well-sorted sand samples: The dispersion arising from the presence of
1881 potassium feldspars and implications for single grain OSL dating. *Quaternary Geochronology*
1882 27:52-65.
- 1883 51. Thomsen KJ, *et al.* (2016) Testing single-grain quartz OSL methods using sediment samples
1884 with independent age control from the Bordes-Fitte rockshelter (Roches d'Abilly site, Central
1885 France). *Quaternary Geochronology* 31:77-96.
- 1886 52. Feathers JK (2017) A response to some unwarranted criticism of single-grain dating:
1887 Comments on Thomsen *et al.*, *Quaternary Geochronology* 31 (2016), 77–96. *Quaternary*
1888 *Geochronology* 37:108-115.
- 1889 53. Guo Y-J, *et al.* (2017) New ages for the Upper Palaeolithic site of Xibaimaying in the Nihewan
1890 Basin, northern China: implications for small-tool and microblade industries in north-east
1891 Asia during Marine Isotope Stages 2 and 3. *Journal of Quaternary Science* 32(4):540-552.
- 1892 54. Duller G (2007) Assessing the error on equivalent dose estimates derived from single aliquot
1893 regenerative dose measurements. *Ancient TL* 25:15-24.
- 1894 55. Huntley DJ & Lamothe M (2001) Ubiquity of anomalous fading in K-feldspars and the
1895 measurement and correction for it in optical dating. *Canadian Journal of Earth Sciences*
1896 38(7):1093-1106.
- 1897 56. Mayya YS, Mortheikai P, Murari MK, & Singhvi AK (2006) Towards quantifying beta
1898 microdosimetric effects in single-grain quartz dose distribution. *Radiation Measurements*
1899 41(7-8):1032-1039.
- 1900 57. Jacobs Z & Roberts RG (2017) Single-grain OSL chronologies for the Still Bay and Howieson's
1901 Poort industries and the transition between them: Further analyses and statistical modelling.
1902 *Journal of Human Evolution* 107:1-13.
- 1903 58. Sharp WD, *et al.* (2019) ²³⁰Th/U burial dating of ostrich eggshell. *Quaternary Science*
1904 *Reviews* 219:263-276.

- 1905 59. Niespolo EM, Sharp WD, Avery G, & Dawson TE (2021) Early, intensive marine resource
 1906 exploitation by Middle Stone Age humans at Ysterfontein 1 rockshelter, South Africa. *Proc*
 1907 *Natl Acad Sci U S A* 118(16).
- 1908 60. Jaffey AH, Flynn KF, Glendenin LE, & Essling AM (1971) Precision measurement of half-lives
 1909 and specific activities of ^{235}U and ^{238}U . *Physical Review C* 4:1889-1906.
- 1910 61. Cheng H, *et al.* (2013) Improvements in ^{230}Th dating, ^{230}Th and ^{234}U half-life values, and U–Th
 1911 isotopic measurements by multi-collector inductively coupled plasma mass spectrometry.
 1912 *Earth and Planetary Science Letters* 371-372:82-91.
- 1913 62. Kohn MJ (2008) Models of diffusion-limited uptake of trace elements in fossils and rates of
 1914 fossilization. *Geochimica et Cosmochimica Acta* 72:3758-2770.
- 1915 63. Neumann K, *et al.* (2019) International code for phytolith nomenclature (ICPN) 2.0. *Annals of*
 1916 *Botany* 124:189-199.
- 1917 64. Cordova CE (2013) C3 Poaceae and Restionaceae phytoliths as potential proxies for
 1918 reconstructing winter rainfall in South Africa. *Quaternary International* 287:121-140.
- 1919 65. Esteban I, *et al.* (2017) Modern soil phytolith assemblages used as proxies for paleoscape
 1920 reconstruction on the south coast of South Africa. *Quaternary International* 434:160-179.
- 1921 66. Linder HP, Eldenas P, & Briggs BG (2003) Contrasting patterns of radiation in African and
 1922 Australian Restionaceae. *Evolution* 57:2688-2702.
- 1923 67. Bergh NG, Verboom GA, Rouget M, & Cowling RM (2014) Vegetation types of the Greater
 1924 Cape Floristic Region. *Fynbos: Ecology, Evolution, and Conservation of a Megadiverse Region*,
 1925 eds Allsopp N, Colville JF, & Verboom GA (Oxford University Press, Oxford).
- 1926 68. Novello A, Bamford MK, van Wijk Y, & Wurz S (2018) Phytoliths in modern plants and soils
 1927 from Klasies River, Cape Region (South Africa). *Quaternary International* 464:440-459.
- 1928 69. Scott L, *et al.* (2021) A 14000 year multi-proxy alluvial record of ecotone changes in a
 1929 Fynbos-Succulent Karoo transition in South Africa. *Palaeogeography, Palaeoclimatology,*
 1930 *Palaeoecology* 569.
- 1931 70. Cordova C & Scott L (2010) The potential of Poaceae, Cyperaceae, and Restionaceae
 1932 phytoliths to reflect past environmental conditions in South Africa. *Palaeoecology of Africa*
 1933 30 107-133.
- 1934 71. Piperno DR (2006) *Phytoliths: A Comprehensive Guide for Archaeologists and Paleoecologists*
 1935 (AltaMira Press, Oxford).
- 1936 72. Chase BM & Meadows ME (2007) Late Quaternary dynamics of southern Africa's winter
 1937 rainfall zone. *Earth-Science Reviews* 84(3-4):103-138.
- 1938 73. Stuut J-B, *et al.* (2002) A 300-kyr record of aridity and wind strength in southwestern Africa:
 1939 inferences from grain-size distributions of sediments on Walvis Ridge, SE Atlantic. *Marine*
 1940 *Geology* 180:221-233.
- 1941 74. van Zinderen Bakker EM (1976) The evolution of late Quaternary paleoclimates of Southern
 1942 Africa. *Palaeoecology of Africa* 9:160-202.
- 1943 75. Little MG, *et al.* (1997) Trade wind forcing of upwelling, seasonality, and Heinrich events as a
 1944 response to sub-Milankovitch climate variability. *Paleoceanography* 12:568-576.
- 1945 76. Pichevin L, Cremer M, Giraudeau J, & Bertrand P (2005) A 190 kyr record of lithogenic grain-
 1946 size on the Namibian slope: forging a tight link between past wind-strength and coastal
 1947 upwelling dynamics. *Marine Geology* 218:81-96.
- 1948 77. Chase BM, *et al.* (2015) Influence of tropical easterlies in southern Africa's winter rainfall
 1949 zone during the Holocene. *Quaternary Science Reviews* 107:138-148.
- 1950 78. Chase BM & Thomas DSG (2007) Multiphase late Quaternary aeolian sediment accumulation
 1951 in western South Africa: Timing and relationship to palaeoclimatic changes inferred from the
 1952 marine record. *Quaternary International* 166(1):29-41.
- 1953 79. Stokes S, Thomas DSG, & Washington R (1997) Multiple episodes of aridity in southern Africa
 1954 since the last interglacial period. *Nature* 388:154-158.

- 1955 80. Still CJ, Berry JA, Collatz GJ, & DeFries RS (2003) Global distribution of C3 and C4 vegetation:
1956 carbon cycle implications. *Global Biogeochemical Cycles* 17:6-1-6-14.
- 1957 81. Collatz GJ, Berry JA, & Clark JS (1998) Effects of climate and atmospheric CO₂ partial
1958 pressure on the global distribution of C4 grasses: present, past, and future. *Oecologia*
1959 114:441-454.
- 1960 82. Ehleringer JR, Cerling TE, & Helliker BR (1997) C4 photosynthesis, atmospheric CO₂, and
1961 climate. *Oecologia* 112:285-299.
- 1962 83. Teeri JA & Stowe LG (1976) Climatic patterns and the distribution of C4 grasses in North
1963 America. *Oecologia* 23:1-12.
- 1964 84. Keeling RF & Keeling CD (2017) Atmospheric Monthly In Situ CO₂ Data - Mauna Loa
1965 Observatory, Hawaii. ed Data SCP (UC San Diego Library Digital Collections).
- 1966 85. Fick SE & Hijmans RJ (2017) WorldClim 2: new 1-km spatial resolution climate surfaces for
1967 global land areas. *International Journal of Climatology* 37(12):4302-4315.
- 1968 86. Mucina L, *et al.* (2006) Succulent Karoo Biome. *The vegetation of South Africa, Lesotho and*
1969 *Swaziland*, Strelizia, eds Mucina L & Rutherford MC (SANBI, Pretoria), Vol 19.
- 1970 87. Petit JR, Raynaud, D., *et al.* (1999) Climate and atmospheric history of the past 420,000 years
1971 from the Vostok ice core, Antarctica. *Nature* 399:429-436.
- 1972 88. Siegenthaler U, *et al.* (2005) Stable carbon cycle-climate relationship during the Late
1973 Pleistocene. *Science* 310(5752):1313-1317.
- 1974 89. Chevalier M, Chase BM, Quick LJ, Dupont LM, & Johnson TC (2020) Temperature change in
1975 subtropical southeastern Africa during the past 790,000 yr. *Geology* 49(1):71-75.
- 1976 90. Stute M & Talma AS (1998) Glacial temperatures and moisture transport regimes
1977 reconstructed from noble gas and d18O, Stampriet aquifer, Namibia. *Isotope Techniques in*
1978 *the Study of Past and Current Environmental Changes in the Hydrosphere and the*
1979 *Atmosphere*, (IAEA Vienna Symposium 1997, Vienna, Austria), pp 307-318.
- 1980 91. Chase BM, Chevalier M, Boom A, & Carr AS (2017) The dynamic relationship between
1981 temperate and tropical circulation systems across South Africa since the last glacial
1982 maximum. *Quaternary Science Reviews* 174:54-62.
- 1983 92. Chase BM, *et al.* (2019) Orbital controls on Namib Desert hydroclimate over the past 50,000
1984 years. *Geology* 47(9):867-871.
- 1985 93. Farmer EC, deMenocal PB, & Marchitto TM (2005) Holocene and deglacial ocean
1986 temperature variability in the Benguela upwelling region: implications for low-latitude
1987 atmospheric circulation. *Paleoceanography* 20:PA2018.
- 1988 94. Rebelo AG, Boucher C, Helme N, Mucina L, & Rutherford MC (2006) Fynbos Biome. *The*
1989 *Vegetation of South Africa, Lesotho and Swaziland*, Strelizia, eds Mucina L & Rutherford MC
1990 (SANBI, Pretoria), Vol 19.
- 1991 95. Cordova C & Avery G (2017) African savanna elephants and their vegetation associations in
1992 the Cape Region, South Africa: Opal phytoliths from dental calculus on prehistoric, historic
1993 and reserve elephants. *Quaternary International* 443:189-211.
- 1994 96. Wadley L, *et al.* (2011) Middle Stone Age bedding construction and settlement patterns at
1995 Sibudu, South Africa. *Science* 334(6061):1388-1391.
- 1996 97. Skead C (2011) *Historical Incidence of the Larger Land Mammals in the Broader Northern and*
1997 *Western Cape* (Centre for African Conservation Ecology, Nelson Mandela Metropolitan
1998 University, Port Elizabeth, South Africa) 2nd edition Ed.
- 1999 98. Skead CJ (1980) *Historical Mammal Incidence in the Cape Province. Volume 1: The Western*
2000 *and Northern Cape* (Department of Nature and Environmental Conservation, Cape Town).
- 2001 99. Skinner JD & Chimimba CT (2005) *The Mammals of the Southern African Subregion*
2002 (Cambridge University Press, Cambridge) 3rd edition Ed.
- 2003 100. Cowling RM & Pierce S (1999) *Namaqualand: A Succulent Desert* (Fernwood Press, Vlaeberg,
2004 South Africa).

- 2005 101. Klein RG (1983) Palaeoenvironmental implications of Quaternary large mammals in the
2006 Fynbos Biome. *Fynbos palaeoecology: a preliminary synthesis.* , eds Deacon HJ, Hendey QB,
2007 & Lambrechts JJN (South African National Scientific Programmes Reports., Pretoria), Vol 75,
2008 pp 116-138.
- 2009 102. Orton JD (2012) Late Holocene archaeology in Namaqualand, South Africa: hunter-gatherers
2010 and herders in a semi-arid environment. (University of Oxford).
- 2011 103. Dewar G & Stewart BA (2012) Preliminary results of excavations at Spitzkloof Rockshelter,
2012 Richtersveld, South Africa. *Quaternary International* 270:30-39.
- 2013 104. Klein RG, Cruz-Uribe K, Halkett D, Hart T, & Parkington JE (1999) Paleoenvironmental and
2014 human behavioral implications of the Boegoeberg 1 Late Pleistocene hyena den, Northern
2015 Cape Province, South Africa. *Quaternary Research* 52(393-403).
- 2016 105. Klein RG (1991) Size variations in the Cape dune mole rat (*Bathyergus suillus*) and late
2017 Quaternary climatic change in the south-western Cape Province, South Africa. *Quaternary
2018 Research* 36:243-256.
- 2019 106. Churcher CS (1986) The extinct Cape zebra. *Sagittarius* 1:4-5.
- 2020 107. Klein RG (1980) Environmental and ecological implications of large mammals from Upper
2021 Pleistocene and Holocene sites in southern Africa. *Annals of the South African Museum*
2022 81:223-283.
- 2023 108. Klein RG (2000) Human evolution and large mammal extinctions. *Antelopes, Deer, and
2024 Relatives, Present and Future: Fossil Record, Behavioral Ecology, Systematics, and
2025 Conservation*, eds Vrba E & Schaller GS (Yale University Press, New Haven), pp 128-139.
- 2026 109. Faith JT (2014) Late Pleistocene and Holocene mammal extinctions on continental Africa.
2027 *Earth-Science Reviews* 128:105-121.
- 2028 110. Klein RG & Cruz-Uribe K (1996) Exploitation of large bovids and seals at Middle and Later
2029 Stone Age sites in South Africa. *Journal of Human Evolution* 31:315-334.
- 2030 111. Weaver TD, Steele TE, & Klein RG (2011) The abundance of eland, buffalo, and wild pigs in
2031 Middle and Later Stone Age sites. *Journal of Human Evolution* 60:309-314.
- 2032 112. Klein RG (1976) The fossil history of *Raphicerus* H. Smith, 1827 (Bovidae, Mammalia) in the
2033 Cape Biotic Zone. *Annals of the South African Museum* 71:169-191.
- 2034 113. Branch GM, Branch ML, & Bannister A (1981) *The Living Shores of Southern Africa* (C. Struik
2035 Publishers, Cape Town).
- 2036 114. Avery GD, Halkett D, Orton J, Steele TE, & Klein RG (2008) The Ysterfontein 1 Middle Stone
2037 Age Rockshelter and the evolution of coastal foraging. *South African Archaeological Society
2038 Goodwin Series* 10:66-89.
- 2039 115. Parkington JE (2006) *Shorelines, Strandlopers and Shell Middens* (Creda Communications,
2040 Cape Town).
- 2041 116. Dewar G (2008) *The archaeology of the coastal desert of Namaqualand, South Africa: a
2042 regional synthesis* (British Archaeological Reports International Series, Oxford).
- 2043 117. Webley L (1992) The history and ethnoarchaeology of pastoralist and hunter-gatherer
2044 settlement in the north-western Cape, South Africa. PhD (University of Cape Town, Cape
2045 Town).
- 2046 118. Orton JD (2014) The late pre-colonial site of Komkans 2 (KK002) and an evaluation of the
2047 evidence for indigenous copper smelting in Namaqualand, southern Africa. *Azania:
2048 Archaeological Research in Africa* 49:386-410.
- 2049 119. Orton JD (2007) The sampling of ephemeral shell scatters in Namaqualand, South Africa.
2050 *South African Archaeological Bulletin* 62:74-78.
- 2051 120. Parkington JE (1976) Coastal settlement between the mouths of the Berg and Oliphants
2052 Rivers, Cape Province. *South African Archaeological Bulletin* 31(127-140).
- 2053 121. Kyriacou K & Parkington JE (2015) Prehistoric shellfish exploitation along the Northern Cape
2054 coast: the Middle and Later Stone age shellfish assemblages from Brandsebaai,
2055 Namaqualand. *South African Archaeological Bulletin* 70:28-35.

- 2056 122. Branch GM, Griffiths C, Branch M, & Beckley L (1994) *Two Oceans: A guide to the marine life*
2057 *of southern Africa* (David Philip, Cape Town).
- 2058 123. Buchanan WF, Parkington JE, Robey TS, & Vogel JC (1984) Shellfish, subsistence and
2059 settlement: some western Cape Holocene observations. *Frontiers: Southern African*
2060 *Archaeology Today*, BAR International Series, eds Hall M, Avery G, Avery DM, Wilson ML, &
2061 Humphreys AJB (British Archaeological Reports, Oxford), Vol 207, pp 121-130.
- 2062 124. Lasiak T (1992) Contemporary shellfish-gathering practices of indigenous coastal people in
2063 Transkei: some implications for interpretation of the archaeological record. *South African*
2064 *Journal of Science* 88:19-28.
- 2065 125. Bigalke EH (1973) The exploitation of shellfish by coastal tribesmen of the Transkei. *Annals*
2066 *of the Cape Province Museum (Natural History)* 9:159-175.
- 2067 126. Erlandson JM (2001) The archaeology of aquatic adaptations: paradigms for a new
2068 millennium. *Journal of Archaeological Research* 9:287-350.
- 2069 127. Buchanan WF (1988) *Shellfish in Prehistoric Diet: Elands Bay, S. W. Cape Coast, South Africa*
2070 (British Archaeological Reports International Series, Oxford).
- 2071 128. Steele TE & Klein RG (2013) The Middle and Later Stone Age faunal remains from Diepkloof
2072 Rock Shelter, Western Cape, South Africa. *Journal of Archaeological Science* 40(9):3453-
2073 3462.
- 2074 129. Plug I (2006) Aquatic animals and their associates from the Middle Stone Age levels at
2075 Sibudu. *Southern African Humanities* 18:289-299.
- 2076 130. Vogelsang R (1998) *Middle Stone Age Fundstellen in Südwest-Namibia. Africa* (Heinrich-
2077 Barth-Institut, Köln).
- 2078 131. Schmidt I, *et al.* (2016) New investigations at the Middle Stone Age site of Pockenbank
2079 Rockshelter, Namibia. *Antiquity* 90:e2.
- 2080 132. Mitchell PJ (1996) Prehistoric exchange and interaction in southeastern Southern Africa:
2081 Marine shells and ostrich eggshell. *African Archaeological Review* 13:35-76.
- 2082 133. Orton JD (2018) VR048: An open-air Later Stone Age site on the Knersvlakte of southern
2083 Namaqualand. *South African Archaeological Bulletin* 73:126-137.
- 2084 134. Orton JD, Klein RG, Mackay A, Schwartz S, & Steele TE (2011) Two Holocene rock shelter
2085 deposits from the Knersvlakte, southern Namaqualand, South Africa. *Southern African*
2086 *Humanities* 23:109-150.
- 2087 135. Henshilwood CS, *et al.* (2011) A 100,000-year-old ochre-processing workshop at Blombos
2088 Cave, South Africa. *Science* 334(6053):219-222.
- 2089 136. Anonymous (!!! INVALID CITATION !!! (111, 132, 133)).
- 2090 137. Anonymous (!!! INVALID CITATION !!! (134, 135)).
- 2091 138. Steele TE, Álvarez-Fernández E, & Hallett-Desguez E (2019) A review of shells as personal
2092 ornamentation during the African Middle Stone Age. *PaleoAnthropology* 2019:24-51.
- 2093 139. Collins B & Steele TE (2017) An often overlooked resource: Ostrich (*Struthio* spp.) eggshell in
2094 the archaeological record. *Journal of Archaeological Science: Reports* 13:121-131.
- 2095 140. Kandel AW (2004) Modification of ostrich eggs by carnivores and its bearing on the
2096 interpretation of archaeological and paleontological find. *Journal of Archaeological Science*
2097 31:377-391.
- 2098 141. Schmidt P, Buck G, Berthold C, Lauer C, & Nickel KG (2018) The mechanical properties of
2099 heat-treated rocks: a comparison between chert and silcrete. *Archaeological and*
2100 *Anthropological Sciences*.
- 2101 142. Soriano S, Villa P, & Wadley L (2007) Blade technology and tool forms in the Middle Stone
2102 Age of South Africa: the Howiesons Poort and post-Howiesons Poort at Rose Cottage Cave.
2103 *Journal of Archaeological Science* 34(5):681-703.
- 2104 143. Schmidt P, *et al.* (2013) Heat treatment in the South African Middle Stone Age: temperature
2105 induced transformations of silcrete and their technological implications. *Journal of*
2106 *Archaeological Science* 40(9):3519-3531.

- 2107 144. Schmidt P, *et al.* (2015) A previously undescribed organic residue sheds light on heat
2108 treatment in the Middle Stone Age. *J Hum Evol.*
- 2109 145. Kandel AW, *et al.* (2015) Increasing Behavioral Flexibility? An Integrative Macro-Scale
2110 Approach to Understanding the Middle Stone Age of Southern Africa. *Journal of*
2111 *Archaeological Method and Theory.*
- 2112 146. Stewart BA, *et al.* (2012) Afromontane foragers of the Late Pleistocene: Site formation,
2113 chronology and occupational pulsing at Melikane Rockshelter, Lesotho. *Quaternary*
2114 *International* 270:40-60.
- 2115 147. Porraz G, *et al.* (2013) Technological successions in the Middle Stone Age sequence of
2116 Diepkloof Rock Shelter, Western Cape, South Africa. *Journal of Archaeological Science*
2117 40(9):3376-3400.
- 2118 148. Villa P, Soressi M, Henshilwood CS, & Mourre V (2009) The Still Bay points of Blombos Cave
2119 (South Africa). *Journal of Archaeological Science* 36(2):441-460.
- 2120 149. de la Peña P, Wadley L, & Lombard M (2013) Quartz bifacial points in the Howiesons Poort of
2121 Sibudu. *South African Archaeological Bulletin* 69(198):119-136.
- 2122 150. Beaumont PB (1978) Border Cave. MA (University of Cape Town).
- 2123 151. Rots V, Lentfer C, Schmid VC, Porraz G, & Conard NJ (2017) Pressure flaking to serrate
2124 bifacial points for the hunt during the MIS5 at Sibudu Cave (South Africa). *PLoS One*
2125 12(4):e0175151.
- 2126 152. Lombard M, Wadley L, Jacobs Z, Mohapi M, & Roberts RG (2010) Still Bay and serrated
2127 points from Umhlatuzana Rock Shelter, Kwazulu-Natal, South Africa. *Journal of*
2128 *Archaeological Science* 37(7):1773-1784.
- 2129 153. Feathers J (2015) Luminescence dating at Diepkloof Rock Shelter – new dates from single-
2130 grain quartz. *Journal of Archaeological Science* 63:164-174.
- 2131 154. Jacobs Z & Roberts RG (2015) An improved single grain OSL chronology for the sedimentary
2132 deposits from Diepkloof Rockshelter, Western Cape, South Africa. *Journal of Archaeological*
2133 *Science* 63:175-192.
- 2134 155. Archer W, Pop CM, Gunz P, & McPherron SP (2016) What is Still Bay? Human biogeography
2135 and bifacial point variability. *Journal of Human Evolution* 97:58-72.
- 2136 156. Mackay A, Stewart BA, & Chase BM (2014) Coalescence and fragmentation in the late
2137 Pleistocene archaeology of southernmost Africa. *Journal of Human Evolution* 72:26-51.
- 2138 157. Chazan M, *et al.* (2020) Archeology, Environment, and Chronology of the Early Middle Stone
2139 Age Component of Wonderwerk Cave. *Journal of Paleolithic Archaeology* 3(3):302-335.
- 2140 158. Wurz S (2013) Technological Trends in the Middle Stone Age of South Africa between MIS 7
2141 and MIS 3. *Current Anthropology* 54(S8):S305-S319.
- 2142 159. Lombard M, *et al.* (2012) South African and Lesotho Stone Age sequence updated. *South*
2143 *African Archaeological Bulletin* 67(195):120-144.
- 2144 160. Schmid V, Conard NJ, Parkington J, Texier PJ, & Porraz G (2016) The ‘MSA 1’ of Elands Bay
2145 Cave (South Africa) in the context of the southern African Early MSA technologies. *Southern*
2146 *African Humanities* 29:153-201.
- 2147 161. Will M & Mackay A (2016) What factors govern the procurement and use of silcrete during
2148 the Stone Age of South Africa? *Journal of Archaeological Science: Reports.*
- 2149 162. Wadley L, de la Peña P, & Prinsloo LC (2017) Responses of South African Agate and
2150 Chalcedony When Heated Experimentally, and the Broader Implications for Heated
2151 Archaeological Minerals. *Journal of Field Archaeology*:1-14.
- 2152 163. Schmidt P, Stynder D, Conard NJ, & Parkington JE (2020) When was silcrete heat treatment
2153 invented in South Africa? *Palgrave Communications* 6(1):73.
- 2154 164. Schmidt P (2017) How reliable is the visual identification of heat treatment on silcrete? A
2155 quantitative verification with a new method. *Archaeological and Anthropological Sciences* 11
2156 713-726.

- 2157 165. Schmidt P, Nash DJ, Coulson S, Goden MB, & Awcock GJ (2017) Heat treatment as a universal
2158 technical solution for silcrete use? A comparison between silcrete from the Western Cape
2159 (South Africa) and the Kalahari (Botswana). *PLoS One* 12(7):e0181586.
- 2160 166. Wurz S (2002) Variability in the Middle Stone Age Lithic Sequence, 115,000–60,000 Years
2161 Ago at Klasies River, South Africa. *Journal of Archaeological Science* 29(9):1001-1015.
- 2162 167. Porraz G, *et al.* (2018) The MIS5 Pietersburg at '28' Bushman Rock Shelter, Limpopo
2163 Province, South Africa. *PLoS One* 13(10):e0202853.
- 2164 168. de la Peña P, *et al.* (2018) Revisiting Mwulu's Cave: new insights into the Middle Stone Age in
2165 the southern African savanna biome. *Archaeological and Anthropological Sciences* 11.
- 2166 169. Val A, *et al.* (2021) The place beyond the trees: renewed excavations of the Middle Stone
2167 Age deposits at Olieboomspoor in the Waterberg Mountains of the South African Savanna
2168 Biome. *Archaeological and Anthropological Sciences* 13(7).
- 2169 170. Wilkins J (2020) Is it Time to Retire NASTIES in Southern Africa? Moving Beyond the Culture-
2170 Historical Framework for Middle Stone Age Lithic Assemblage Variability. *Lithic Technology*
2171 45(4):295-307.
- 2172 171. Volman TP (1981) The Middle Stone Age in the Southern Cape. PhD (University of Chicago).
- 2173 172. Douze K, Wurz S, & Henshilwood CS (2015) Techno-Cultural Characterization of the MIS 5 (c.
2174 105 - 90 Ka) Lithic Industries at Blombos Cave, Southern Cape, South Africa. *PLoS One*
2175 10(11):e0142151.
- 2176 173. Backwell LR, *et al.* (2018) New Excavations at Border Cave, KwaZulu-Natal, South Africa.
2177 *Journal of Field Archaeology*:1-20.
- 2178 174. Schmid VC, Porraz G, Zeidi M, & Conard NJ (2019) Blade Technology Characterizing the MIS 5
2179 D-A Layers of Sibudu Cave, South Africa. *Lithic Technology*:1-38.
- 2180 175. Kuman K, Inbar M, & Clarke RJ (1999) Palaeoenvironments and cultural sequence of the
2181 Florisbad Middle Stone Age Hominid Site, South Africa. *Journal of Archaeological Science*
2182 26:1409-1425.
- 2183 176. Will M, Parkington JE, Kandel AW, & Conard NJ (2013) Coastal adaptations and the Middle
2184 Stone Age lithic assemblages from Hoedjiespunt 1 in the Western Cape, South Africa. *J Hum*
2185 *Evol* 64(6):518-537.
- 2186 177. Thompson E, Williams HM, & Minichillo T (2010) Middle and late Pleistocene Middle Stone
2187 Age lithic technology from Pinnacle Point 13B (Mossel Bay, Western Cape Province, South
2188 Africa). *J Hum Evol* 59(3-4):358-377.
- 2189 178. Halkett D, *et al.* (2003) First excavation of intact Middle Stone Age layers at Ysterfontein,
2190 Western Cape Province, South Africa: implications for Middle Stone Age ecology. *Journal of*
2191 *Archaeological Science* 30(8):955-971.
- 2192 179. Wurz S (2012) The significance of MIS 5 shell middens on the Cape coast: A lithic perspective
2193 from Klasies River and Ysterfontein 1. *Quaternary International* 270:61-69.
- 2194 180. Jacobs Z, Jones BG, Cawthra HC, Henshilwood CS, & Roberts RG (2020) The chronological,
2195 sedimentary and environmental context for the archaeological deposits at Blombos Cave,
2196 South Africa. *Quaternary Science Reviews* 235.
- 2197 181. Brenner MJ, Ryano KP, & Wurz S (2020) Coastal adaptation at Klasies River main site during
2198 MIS 5c-d (93,000–110,000 years ago) from a southern Cape perspective. *The Journal of*
2199 *Island and Coastal Archaeology*:1-28.
- 2200 182. Wilkins J, *et al.* (2017) Lithic technological responses to Late Pleistocene glacial cycling at
2201 Pinnacle Point Site 5-6, South Africa. *PLoS One* 12(3):e0174051.
- 2202 183. Brown KS, *et al.* (2009) Fire as an engineering tool of early modern humans. *Science*
2203 325(5942):859-862.
- 2204 184. Pazan KR, Dewar G, & Stewart BA (2020) The MIS 5a (~80 ka) Middle Stone Age lithic
2205 assemblages from Melikane Rockshelter, Lesotho: Highland adaptation and social
2206 fragmentation. *Quaternary International*.

- 2207 185. Hodgskiss T & Wadley L (2017) How people used ochre at Rose Cottage Cave, South Africa: Sixty thousand years of evidence from the Middle Stone Age. *PLoS One* 12(4):e0176317.
- 2208
- 2209 186. Harper PTN (1997) The Middle Stone Age sequences at Rose Cottage Cave: a search for continuity and discontinuity. *South African Journal of Science* 93:470-475.
- 2210
- 2211 187. Pienaar M, Woodborne S, & Wadley L (2008) Optically stimulated luminescence dating at Rose Cottage Cave. *South African Journal of Science* 104:65-70.
- 2212
- 2213 188. Goodwin AJH & van Riet Lowe C (1929) *The Stone Age Cultures of South Africa* (Neill and Co, Edinburgh).
- 2214
- 2215 189. Sampson CG (1974) *The Stone Age archaeology of southern Africa* (Academic Press, New York).
- 2216
- 2217 190. Mason RJ & Brain CK (1988) *Cave of Hearths, Makapansgat, Transvaal* (Archaeological Resaerc Unit, University of the Witswatersrand).
- 2218
- 2219 191. Feathers JK, Evans M, Stratford DJ, & de la Peña P (2020) Exploring complexity in luminescence dating of quartz and feldspars at the Middle Stone Age site of Mwulu's cave (Limpopo, South Africa). *Quaternary Geochronology* 59.
- 2220
- 2221
- 2222 192. Vogelsang R, *et al.* (2010) New Excavations of Middle Stone Age Deposits at Apollo 11 Rockshelter, Namibia: Stratigraphy, Archaeology, Chronology and Past Environments. *Journal of African Archaeology* 8(2):185-218.
- 2223
- 2224
- 2225 193. Mackay A, Jacobs Z, & Steele TE (2015) Pleistocene archaeology and chronology of Putslaagte 8 (PL8) rockshelter, Western Cape, South Africa. *Journal of African Archaeology* 13(1):71-98.
- 2226
- 2227
- 2228 194. Evans U (1994) Hollow Rock Shelter, a Middle Stone Age site in the Cederberg. *Southern African Field Archaeology* 3:63-73.
- 2229
- 2230 195. Högberg A (2016) A Lithic Attribute Analysis on Blades from the Middle Stone Age Site, Hollow Rock Shelter, Western Cape Province, South Africa. *Lithic Technology* 41(2):93-113.
- 2231
- 2232 196. Will M, Mackay A, & Phillips N (2015) Implications of Nubian-like core reduction systems in southern Africa for the identification of early modern human dispersals. *PLoS One*.
- 2233
- 2234 197. Porraz G, *et al.* (2016) Update on the 2011 excavation at Elands Bay Cave (South Africa) and the Verlorenvlei Stone Age. *Southern African Humanities* 29:33-68.
- 2235
- 2236 198. Högberg A (2014) Chronology, stratigraphy and spatial distribution of artefacts at Hollow Rock Shelter, Cape Province, South Africa. *South African Archaeological Bulletin* 69:142-151.
- 2237
- 2238 199. Schmidt P & Högberg A (2018) Heat treatment in the Still Bay - A case study on Hollow Rock Shelter, South Africa. *Journal of Archaeological Science: Reports* 21:712-720.
- 2239
- 2240 200. O'Driscoll CA & Mackay A (2020) On the Operation of Retouch in Southern Africa's Early Middle Stone Age. *Journal of Paleolithic Archaeology* 3(4):1149-1179.
- 2241
- 2242 201. Schmidt P & Mackay A (2016) Why Was Silcrete Heat-Treated in the Middle Stone Age? An Early Transformative Technology in the Context of Raw Material Use at Mertenhof Rock Shelter, South Africa. *Plos One* 11(2):e0149243.
- 2243
- 2244
- 2245 202. Will M, Mackay A, & Phillips N (2015) Implications of Nubian-Like Core Reduction Systems in Southern Africa for the Identification of Early Modern Human Dispersals. *PLoS One* 10(6):e0131824.
- 2246
- 2247
- 2248 203. Parkington JE (1980) The Elands Bay cave sequence: cultural stratigraphy and subsistence strategies. *Proceedings of the Eighth Pan-African Congress of Prehistory and Quaternary Studies*, ed Leakey RAaO, B. A. (Tillmiap, Nairobi), pp 315-320.
- 2249
- 2250
- 2251 204. Tribolo C, *et al.* (2016) Chronology of the Pleistocene deposits at Elands Bay Cave (South Africa) based on charcoals, burnt lithics, and sedimentary quartz and feldspar grains. *Southern African Humanities* 29:129-152.
- 2252
- 2253
- 2254 205. Porraz G, *et al.* (2020) Experimentation as a driving force for innovation in the Pre-Still Bay from Southern Africa. *EcoEvoRxiv*, ch53r, ver. 3, peer-reviewed and recommended by PCI Archaeology.
- 2255
- 2256

- 2257 206. Mackay A (2009) History and Selection in the Late Pleistocene Archaeology of the Western
2258 Cape, South Africa. PhD (Australian National University).
2259 207. Mackay A (2010) The Late Pleistocene archaeology of Klein Kliphuis rockshelter, Western
2260 Cape, South Africa: 2006 excavations. *South African Archaeological Bulletin* 65(192):132-147.
2261 208. Watson S, *et al.* (2020) Robberg material procurement and transport in the Doring River
2262 catchment: Evidence from the open-air locality of Uitspankraal 9, Western Cape, South
2263 Africa. *Journal of African Archaeology* 18:209-228.
2264 209. Trabucco A & Zomer R (2019) Global Aridity Index and Potential Evapotranspiration (ET0)
2265 Climate Database v2.
2266 210. UNEP (1997) *World atlas of desertification* (United Nations Environment Programme,
2267 London) 2nd ed Ed.
2268 211. Dinerstein E, *et al.* (2017) An Ecoregion-Based Approach to Protecting Half the Terrestrial
2269 Realm. *Bioscience* 67(6):534-545.
2270 212. Mucina L & Rutherford MC (2006) *The vegetation of South Africa, Lesotho and Swaziland*
2271 (South African National Biodiversity Institute, Pretoria).
2272